National Technical University of Greece

Interdisciplinary Program of Postgraduate Studies “ENVIRONMENT & DEVELOPMENT”

Academic year 2013 – 15

A study on the distribution of forest tree species and forest biodiversity using hyperspectral and multispectral imagery in the University Research Forest Taxiarchis in Chalkidiki

Postgraduate thesis by:

Maria Kampouri

University Research Forest Taxiarchis (Source: ΑΠΘ, **2014)**

Supervisors:

Prof. Demetre Argialas

Assoc. Prof. Vassilia Karathanassi

Dr. Pol Kolokoussis

Contents

List of Figures

Abstract

The aim of the study is to show how satellite or aerial imagery can be used to estimate patches of high biodiversity for conservation and management purposes in a Mediterranean forest ecosystem. The present thesis investigates the effectiveness of identifying forest tree species through high spatial resolution multispectral satellite imaging, as well as hyperspectral satellite and aerial imagery. We used Landsat and GeoEye multispectral images, as well as CASI and Hyperion hyperspectral images over Taxiarchis University Forest in Chalkidiki, North Greece. The images were subject to pre-processing for the purpose of reducing noise and the number of spectral bands used, along with file size and processing time, without compromising accuracy. The transforms used for band extraction included the Principal Component Analysis (PCA), the Minimum Noise Fraction (MNF) and for band selection, band selection based on the correlation between the spectral signatures of the trees of interest. Masks were created from field sampling was used for defining tree species' spectral signatures, as well as consequent accuracy estimation. Classification was object based and aimed mainly on the identification of tree patches, but also tree species in the case of the CASI imagery with resolution up to 2 m. After the best image in terms of classification accuracy and stability, processing time and suitability in incorporating a fuzzy analysis based on physiographic characteristics of tree distribution, was selected, a biodiversity index (Simpson's Biodiversity Index) was estimated.

Keywords: multispectral, hyperspectral, OBIA, biodiversity, Simpson's Biodiversity Index, Taxiarchis University Forest, PCA, MNF, tree spectral signatures.

Περίληψη

Ο στόχος της παρούσας μελέτης είναι η διερεύνηση μεθόδων ανάλυσης δεδομένων ψηφιακής τηλεπισκόπησης για τον προσδιορισμό περιοχών με υψηλή βιοποικιλότητα για την προστασία και τη σωστή διαχείρισή τους σε ένα Μεσσογειακό δασικό οικοσύστημα. Μετά την ανάλυση μίας ποικιλίας δορυφορικών εικόνων και αεροφωτογραφιών, από το Πανεπιστημιακό Δάσος Ταξιάρχη, με τη μέθοδο της αντικειμενοστραφούς ταξινόμησης (OBIA) και με βάση διανυσματικά δεδομένα, που αποκτήθηκαν μετά από δειγματοληψία πεδίου, ήταν δυνατό να επιλεγούν εικόνες που παρείχαν την πιο ακριβή ταξινόμηση δασικών ειδών δένδρου για περαιτέρω ανάλυση. Οι εικόνες που χρησιμοποιήθηκαν περιλαμβαναν δορυφορικές πολυφασματικές, όπως οι Landsat (υψηλή χωρική ανάλυση) και GeoEye (πολύ υψηλή χωρική ανάλυση), καθώς και υπερφασματικές εικόνες όπως η δορυφορική Hyperion (υψηλή χωρική ανάλυση), και οι υπερφασματικές εικόνες του δέκτη CASI (πολύ υψηλή χωρική ανάλυση). Στις υπερφασματικές εικόνες εφαρμόστηκαν τρεις μέθοδοι μετασχηματισμού με σκοπό τη μείωση των καναλιών, του μεγέθους του αρχείου και του χρονου επεξεργασίας. Αυτές είναι: Ανάλυση Κυρίων Συνιστωσών (PCA), Μετασχηματισμός Ελαχιστοποίησης Θορύβου (MNF) και η επιλογή καναλιων βάσει της συσχέτισης των φασματικών υπογραφών των ειδών δέντρου.

Οι εικόνες που παρείχαν τα καλύτερα αποτελέσματα ακρίβειας ταξινόμησης, οι οποίες επιλέχθηκαν για περαιτέρω επεξεργασία, ήταν η μετασχηματισμένη με τον Μετασχηματισμό Ελαχιστοποίησης Θορύβου (MNF) CASI με 2m χωρική ανάλυση, η εικόνα Landsat, καθώς και η μετασχηματισμένη με MNF Hyperion εικόνα, η οποία αν και δεν παρουσίασε ιδιαίτερα υψηλή ακρίβεια, ήταν χρήσιμη στη σύγκριση και αξιολόγηση των αποτελεσμάτων. Ανάλυση με χρήση ασαφούς λογικής, βάσει της ταξινόμησης δασικών ειδών κατά υψομετρική διαβάθμιση (λαμβάνοντας υπόψη υψόμετρο, κλίση και προσανατολισμό), χρησιμοποιώντας το ψηφιακό μοντέλο εδάφους Aster GDEM, βοήθησαν στη μείωση των συγκρούσεων ταξινόμησης μεταξύ των κατηγοριών, αλλά όχι στη βελτίωση της συνολικής ακρίβειας. Η διαδικασία της ταξινόμησης με τη βοήθεια ασαφούς λογικής για την κατανομή κάθε κατηγορίας από άποψη υψομέτρου και κλίσης (ο προσανατολισμός αποδείχτηκε αναξιόπιστος) ήταν μια χρονοβόρα διαδικασία που απαίτησε προσεκτική παρατήρηση, αλλά οδήγησε σε βελτιώσεις σε ότι αφορά την ακρίβεια ταξινόμησης ορισμένων κατηγοριών κατά την ταξινόμηση.

Ο μετασχηματισμός MNF αποδείχτηκε ένα εξαιρετικά χρήσιμο εργαλείο για τη μείωση των δεδομένων που υποβάλλονται σε επεξεργασία και, κατά συνέπεια, τον χρόνο επεξεργασίας. Επίσης, αποδείχθηκε ότι είναι μια μέθοδος εξαγωγής

χρακτηριστικών, η οποία μπορεί να μειώσει με επιτυχία τον θόρυβο, χωρίς απώλεια χρήσιμων πληροφοριών για την ταξινόμηση των δασικών ειδών, χρησιμοποιώντας αντικειμενοστραφή ταξινόμηση (OBIA). Ειδικά στην περίπτωση της εικόνας CASI, μιας εικόνας με 72 κανάλια, ο MNF μετασχηματισμός αύξησε δραματικά την ταχύτητα του χρόνου επεξεργασίας της, δίνοντας ικανοποιητικά αποτελέσματα ακρίβειας ταξινόμησης. Με μια χωρική ανάλυση 2m, η μετασχηματισμένη με MNF εικόνα CASI αποδείχθηκε η πιο αξιόπιστη για την παροχή μίας σταθερής ταξινόμησης των ειδών δέντρων, ενώ η Landsat και η Hyperion έδωσαν υψηλή ακρίβεια, αλλά χαμηλή σταθερότητα και εμπιστοσύνη στα αποτελέσματα μετά την εισαγωγή περιορισμών ασαφούς λογικής. Μπορούμε λοιπόν να συμπεράνουμε ότι η χωρική ανάλυση πρέπει να είναι τουλάχιστον 2 μέτρα για την αποτελεσματική ταυτοποίηση των ειδών δέντρου όταν εφαρμόζεται αντικειμενοστραφής ταξινόμηση.

Σε μια μελλοντική μελέτη, μπορεί να είναι χρήσιμο για τα δεδομένα του εδάφους να συλλέγονται βάσει αμιγών κατηγοριών και όχι μεικτών, όταν η μελέτη χρησιμοποιείται για τους σκοπούς της ψηφιακής τηλεπισκόπησης, με σκοπό τον προσδιορισμό συγκεκριμένων φασματικών υπογραφών ανά είδος. Μια άλλη προοπτική για τη βελτίωση των αποτελεσμάτων της παρούσας μελέτης, είναι η αξιοποίηση των φασματικών υπογραφών ανά είδος δέντρου, το οποίο θα μπορούσε στη συνέχεια να χρησιμοποιηθεί για την ανάλυση των τηλεπισκοπικών δεδομένων.

Ο Δείκτης Βιοποικιλότητας Simpson υπολογίστηκε και παρουσιάστηκε με τη μορφή ενός χάρτη, που δείχνει περιοχές εντός του δάσους του Ταξιάρχη με υψηλή βιοποικιλότητα. Δασικά δένδρα μπορεί να αποτελούν οικότοπους για μια ποικιλία ζωντανών οργανισμών. Λαμβάνοντας υπόψη τη σημασία που αποδίδεται στη βιοποικιλότητα, από άποψη πολιτικής και νομοθεσίας της ΕΕ, ως κριτήριο για τη προστασία του οικοσυστήματος, η χρήση τηλεπισκόπησης για τον εντοπισμό περιοχών με υψηλή βιοποικιλότητα είναι σημαντική, διότι αυτό θα μπορούσε να αφορά εξαιρετικά μεγάλες δασικές περιοχές ή ακόμα και άλλους τύπους οικοσυστημάτων. Σε περιοχές όπου παρατηρείται μεγάλη βιοποικιλότητα, θα μπορούσαν να ενταθούν οι προσπάθειες περιβαλλοντικής προστασίας παρέχοντας προστασία για ένα ολόκληρο οικοσύστημα. Επιπλέον, ζώνες προστασίας θα μπορούσαν να σχεδιαστούν γύρω από περιοχές που θεωρούνται οικολογικά πολύτιμες δεδομένης της υψηλής βιοποικιλότητας, κάνοντας χρήση εργαλείων ψηφιακής τηλεπισκόπησης.

Introduction

Since Darwin and Wallace, biologists concerned with ecology and evolution have been trying to interpret the distribution of species and discover why certain areas are especially species-rich (Turner *et al.*, 2003). Biologists appreciate today that biodiversity is based on different levels of organisation. The management approach of protecting biodiversity offers a possibility for integrated environmental protection, as opposed to a species-centered approach.

Biodiversity does not only represent a collection of genes, species, ecosystems or any other grouping for a particular area. The fact that an area might contain 500 species while another contains 50 does not offer sufficient information to evaluate their relative importance when aiming for environmental protection. Biodiversity usually takes into consideration the rate of occurrence or the abundance of a species or of another ecological entity, along with the multitude of species within the sample. Biodiversity indices, such as the Shannon & Weaver and the Simpson Index combine species richness with a measure of the degree of heterogeneity in their distribution.

When a natural landscape is fragmented, for example, the total biodiversity of a community may remain on the same levels or may increase, even though the integrity of the community may have been compromised due to the intrusion of alien-species, dislocating for example species which previously existed there. As an area gradually loses its character, global biodiversity is reduced (Noss, 1990).

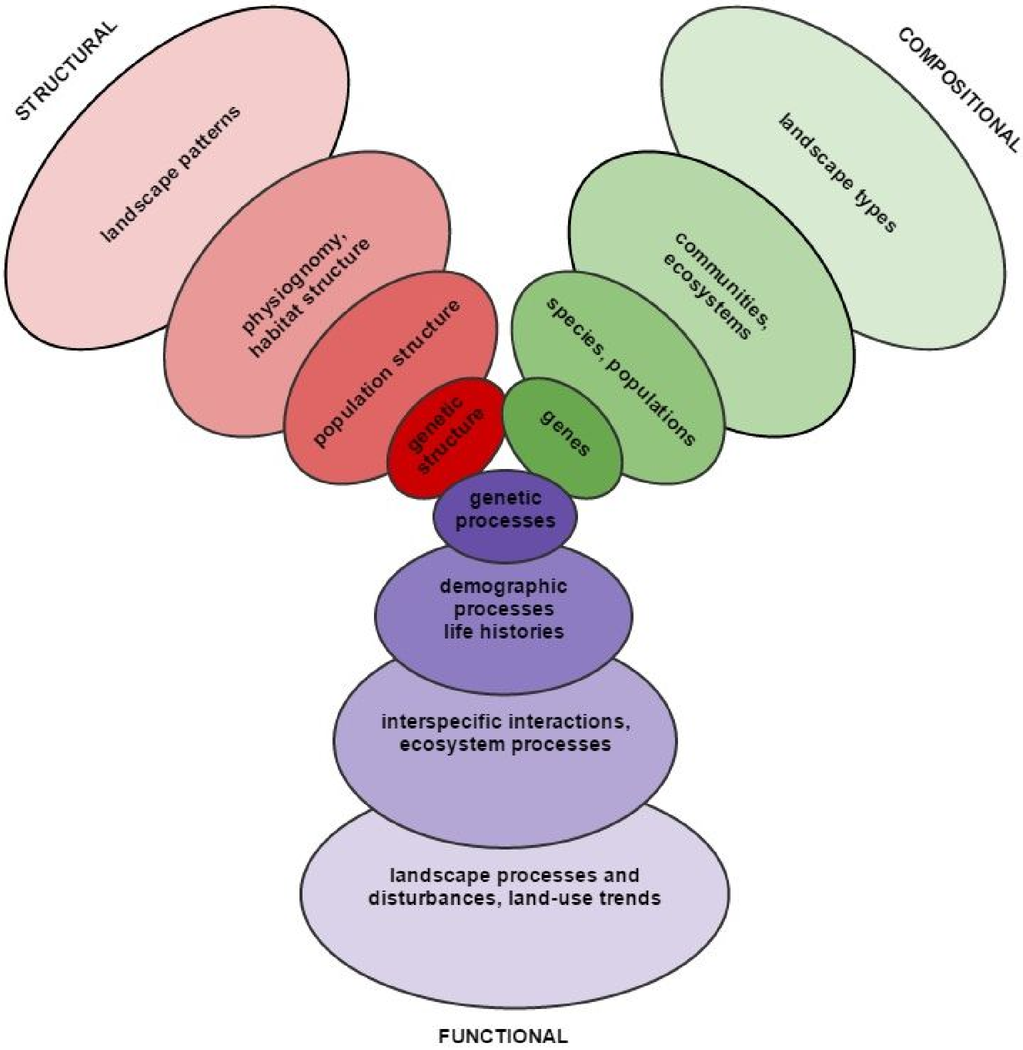

Figure 1: Compositional, structural and functional biodiversity, as interconnected spheres, with each one including multiple levels of organisation. This ideological framework can facilitate the selection of indices, which represent the multiple dimensions of biodiversity, ensuring the adoption of the most suitable approach in environmental monitoring and evaluation programs (Source: Noss, 1990).

The hierarchical theory proposes that higher levels of organization include and restrict the behaviour of lower levels. Based on this theory, global environmental problems, such as the greenhouse effect and the reduction of ozone in the stratosphere constitute substantial obstacles for the protection of natural ecosystems or endangered species. The requirement for the acquisition of consistent temporal and spatial data regarding natural ecosystems on a global scale and especially within the EU is a commitment, which creates the requirement for the development of suitable tools for monitoring. Specifically, the Framework Directive of the United Nations for Climate Change, during which the Kyoto Protocol was agreed on, invites participant countries to provide information concerning carbon sinks (such as forests and oceans), as well as their evolution in time (De Fries *et al.*, 2000).

This theoretical background of hierarchical structure of different levels of ecosystem organisation (see figure 1) allows for the selection of indicators, which represent the multiple sides of biodiversity and create a practical background for the development of monitoring and protection programs. On higher levels of organisation, a valuable monitoring tool is remote sensing. While research on lower levels focuses on the mechanistic basis of the interactions between species, which constitutes the basis for the motives, arrangements and reiterations constitute higher levels of organisation. The structure, biodiversity and productivity of a landscape can be recorded through aerial and satellite photography to provide a time-series record (Noss, 1990; Turner *et al.*, 2003).

Digital sensors offer systematic and synoptic visualisation of ground cover and land uses at regular time intervals (Nagendra, 2001). For example, Landsat 8 (see appendix I) with a pixel resolution of 30 m (15 m for panchromatic data), offers data for the entire surface of the Earth on 16-day intervals, which are distributed for free (USGS, 2014). Remote sensing is an important tool for the study of biodiversity on a large and medium scale, while on smaller scales, remote sensing data can be used for the evaluation of structural changes in a forest ecosystem, as well as motives that emerge over time (Townshend et al., 1991).

According to Jones & Riddle (1996), the evaluation of biodiversity can be studied on different scales depending on the objective and aim of the study. On a global scale, it is possible to use satellite images for the study of the factors affecting the distribution of species-rich areas. On a landscape scale, remote sensing can be a tool for identifying current trends for biodiversity and biotopes.

Remote sensing can provide answers in the form of maps and inventories, while allowing for the quantification of environmental characteristics, as well as the evaluation of the fundamental conditions of biodiversity. When combined with additional data from field studies, remote sensing can significantly contribute to the illustration of biodiversity through digitally processed images, ultimately assisting in management, conservation and decision-making (Innes & Koch, 1998). Whilst the rate of biotope loss remains high, the need for the protection of biodiversity becomes increasingly urgent. For the purpose of planning strategies for conservation, remote sensing provides a systematic tool in gathering information concerning the distribution and dynamics of species constituting an ecosystem, as well as their course in time (Nagendra, 2001).

The majority of studies on biodiversity focus on canopy tree species of a forested area (even though in recent years with the use of radar sensors, such as Lidar, penetration on lower vegetative levels is feasible), as these are usually static and bulky organisms. However, various studies conclude that the distinction between tree species is particularly difficult and requires both good resolution of imaging and a suitable selection of a spectral signature area (or a combination), which depends on the biochemical composition of an organism. In most cases, the accuracy of classification, which is achieved for the identification of tree species using remote sensing data, varies between 50% and 90%. In case the aim of a study is the identification of a homogenous assimilation of tree species classification accuracy is improved. Reliability of results can be substantially improved incorporating data from a digital elevation model (DEM) (Nagendra, 2001; Franklin *et al.*, 1994).

The present thesis investigates the effectiveness of identifying forest tree species through high spatial resolution multispectral satellite imaging, as well as hyperspectral satellite and aerial imagery. An outline of the proposed methodology is depicted in figure 2. We used Landsat and GeoEye multispectral images, as well as CASI and Hyperion hyperspectral images over Taxiarchis University Forest in Chalkidiki, North Greece. The images were subject to pre-processing for the purpose of reducing noise and the number of spectral bands used, along with file size and processing time, without compromising accuracy, with the exception of the Landsat image, which was ready for processing. The transforms used for band extraction included the Principal Component Analysis (PCA), the Minimum Noise Fraction (MNF) and for band selection, band selection based on the correlation between the spectral signatures of the trees of interest (see figure 2). After the best image in terms of classification accuracy and stability, processing time and suitability in incorporating a fuzzy analysis based on physiographic characteristics of tree distribution, was selected, a biodiversity index (Simpson's Biodiversity Index) was estimated.

The aim of the study is to show how satellite or aerial imagery can be used to estimate patches of high biodiversity for conservation and management purposes. The implication concerns the entire ecosystem, as forest constitutes the habitat of numerous species of animal and plant life, as well as microorganisms.

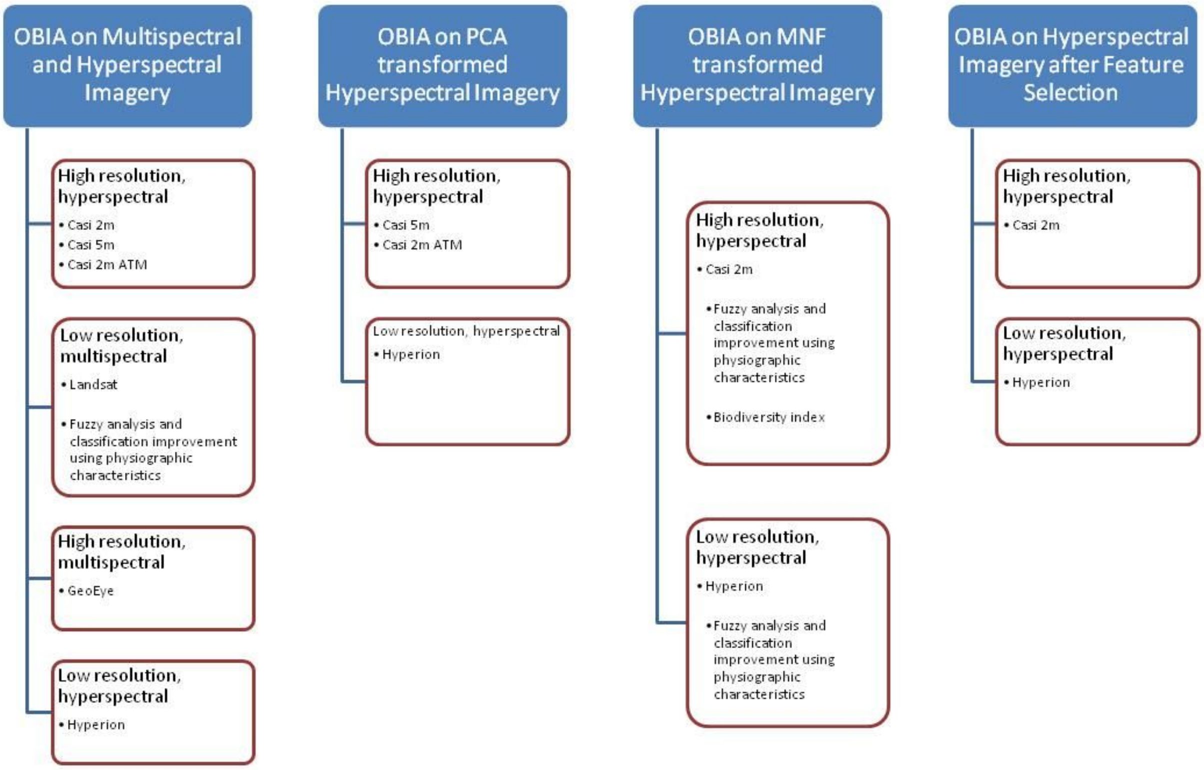

Figure 2: Methodology outline and flowchart.

1. Literature Review

1.1 Biodiversity and Ecosystem Monitoring

The concept of biodiversity, which includes variation at the level of genes, species and ecosystems, has been evolving over the past 25 years after being proposed by E.O. Wilson (1988). In his 1985 paper, "The crisis of biological diversity" Wilson wrote:

> *The worst thing that can happen during the 1980s is not energy depletion, economic collapse, limited nuclear war, or conquest by a totalitarian government. As terrible as these catastrophes would be for us, they can be repaired within a few generations. The one process ongoing in the 1980s that will take millions of years to correct is the loss of genetic and species diversity by the destruction of natural habitats. This is the folly that our descendents are least likely to forgive us.*

Wilson also pointed out the importance of mapping biodiversity in order to plan its conservation and practical use. He has also stressed the importance of identifying patterns in endemism and biodiversity hotspots, ultimately addressing land use and conservation issues (Raven & Wilson, 1992). His vision of mapping global diversity, a task that should be assigned to multidisciplinary research teams on a national level and addressing conservation and land use constitutes today an important EU goal.

Initially, most protected areas were set aside because of their spectacular natural beauty, the occurrence of populations of rare or endangered species, or their value in harboring species of recreational interest. More recently, the identification and prioritisation of places meriting protection has become more systematic and scientific. Several organizations (e.g., Conservation International, the World Wildlife Fund) have targeted places for global protection based upon the biodiversity they contain—so-called "hotspots" of species richness (Myers *et al.*, 2000). Others, such as The Nature Conservancy (TNC), have used inventories of species and communities and assessments of major threats such as development or habitat fragmentation to target areas for protection within broadly defined eco-regions (Groves & The Nature Conservancy, 2003). Systematic conservation planning has become a major focus of conservation and management (Wiens *et al*., 2009).

1.2 Habitats

The term habitat has often been defined as the spatial extent of a resource for a particular species. Habitat in this sense is explicitly linked to a species, or species group sharing the same ecological requirements. Dictionary definitions are also not specific and usually refer generally to communities. The terms 'habitat patch', 'micro-habitats' and 'temporary habitat', are also often used in this respect. Other terms such as biotope and ecosystem are also used in similar contexts in the literature but are rarely defined. In recent years the latter term has been increasingly used in the concept of ecosystem services but as described by Fisher *et al.* (2009) it is usually applied at a range of different scales from the specific e.g. a crop field to the general such as a riparian zone. Ecosystem services have to be considered as a policy parameter additional to traditional nature conservation (Haslett *et al.*, 2010).

The scientific use of the term habitat shows an evolution in meaning from the vague and broad to the narrow and precise, as shown following examples of definitions:

- "*Place, living space, where an organism lives*" (Odum, 1963).

- "*Place where a species normally lives, often described in terms of physical factors such as topography and soil moisture and by associated dominant forms (e.g. intertidal rock pools or mesquite woodland)*" (Calow, 1999).

- "*Habitat is a zone (area) comprising a set of resources, consumables and utilities, for the maintenance of an organism. The resources occur in union and/or intersect and may also be equivalent; links between resource outlets are established by individual searching movements of the organism*" (Dennis & Shreeve, 1996).

The above definitions are primarily theoretical and are not designed for field mapping with the objective to determine the extent of habitats and their spatial distribution. However, Bunce *et al.* (2008) have adapted the principles originally developed in the Great Britain Countryside Survey for mapping European habitats and rules are provided for assignment of a given patch to a habitat class at a defined scale. Bunce *et al.* (2008) define habitat as "*an element of the land surface that can be consistently defined spatially in the field in order to define the principal environments in which organisms live*".

In addition to their recognition in their own right habitats also have the following practical advantages:

1. Aerial photographs, especially infra-red, can be used to estimate habitat extent and its change over time e.g. Ståhl *et al.* (2011)

2. Remote sensing data from satellites can be linked to in situ maps of habitats to larger units (Mücher *et al.*, 2009).

3. Relationships between habitats and species assemblage composition or particular taxa important to biodiversity can be used to link habitat records to other biodiversity indicators, such as species e.g. Petit and Usher (1998)

4. Habitat records can be linked to changes over time at the landscape level and to vegetation assemblages. Protocols are now available and can be used to link extant habitat data across Europe for five national major monitoring programs and could also be developed for other surveys (Bunce *et al*., 2013).

Habitats are important as indicators of biodiversity in their own right but they are also linked to species and assemblages both of plants and other taxa in a variety of ways. This is axiomatic for plant species, as habitats are often defined by phytosociological syntaxa which are determined by vegetation composition. Plant species, can also be used as indicators for a habitat as described in the Interpretation Manual for Annex I habitats (European Commission, 2007). These species can then be used in conjunction with ancillary data, such as soils, to predict the distribution of the habitats themselves across Europe as shown by Mücher *et al.* (2009).

The landscape ecological literature also provides many studies where habitats have been used as a framework for examining the behaviour of species. Thus Harvey *et al.* (2006) related tree cover to birds, butterflies and dung beetles while Dover *et al.* (2010) examined how the structure even within a single habitat can affect butterfly abundance and Hinsley and Bellamy (2000) show how bird assemblages, even within one habitat, a hedge, are related to management.

Although widely used, the term ‘habitat’ remains diverse, ambiguous, and difficult to apply consistently because it is has been developed in different contexts with contrasting meanings (Bunce *et al.*, 2013).

1.3 Vegetation Mosaics

Vegetation mosaics or complexes are found when two or more communities, each occupying small areas, are found in close proximity, often as a repeating pattern. It is a constant mapping issue as scale increases (decreasing precision), because individual vegetation types can no longer be represented. The concept of vegetation complexes has been developed mainly by Schmithüsen (1948) and Tüxen (1978).

According to dynamic and landscape approaches to vegetation science, the distribution of plant associations within homogeneous regions is not random, and there is a tendency of associations to be related. These relationships can be divided into two categories, as seen below:

- Temporal (i.e. dynamic): communities substitute for each other over time, starting with a pioneer stage and evolving towards a climax community.
- Spatial: as a result of topographical factors, i.e. micromorphology of the substratum or the soil. They can be open or closed, depending on whether the mosaic elements are separated by substrate. An example is a bog system where hummocks and hollows can be shown on a large-scale map, but not at smaller scales.

A third approach is aggregating patches of the same type in order to form a bigger polygon, without representing the mosaic on the map. In the Italian project Carta della Natura (Angelini *et al.*, 2009 *in* EEA & MNHN, 2014), all the patches of the same habitat type that were separated by a distance less than a distance related to the patch size were merged, including the matrix portion that separates them. Thus, a polygon was obtained with a surface area equal to or higher than the minimum mapping unit. When this is not possible, because the patches are too distant or the surface of the aggregation is too small, the polygon is attributed to the predominant habitat types (EEA & MNHN, 2014).

1.4 Legislation

Habitats are specifically referred to in the European Union (EU) Habitats Directive which includes a list (Annex I) of habitats to be protected (European Commission, 1992). These habitats are described in various levels of detail in the Interpretation Manual (European Commission, 2007) which has been revised several times to include additional habitats and revised definitions as the EU has expanded. In the Manual there are some diagnostic features as well as lists of associated species. Criteria to identify a particular habitat or to distinguish between them are not included in the legal text of the Directive.

These habitats, together with selected species listed in Annex II, have been used to construct the Special Areas of Conservation (SAC) which together with Special Protection Areas (SPA) designated under the 1979 EU Birds Directive and Marine Protected Areas (MPA) form the Natura 2000 network which is the primary framework for site-based nature protection in the EU. EU Member states are also obliged to report on the conservation status of these habitats every six years under Article 17 of the Habitats Directive and Article 12 of the Birds Directive.

In addition, the RAMSAR Convention relates to one habitat group, wetlands. Habitats are also referred to in the Berne Convention with an agreed list of habitats to be used for selection of sites for its Emerald Network (Council of Europe, 2014). Habitat conservation is also one of the 2020 targets (Aichi targets) of the Convention on Biological Diversity and its status is an important category to report on (GEO BON, 2011). Habitats are therefore a central pillar of European nature conservation policy.

The categorisation of European habitats started with the earlier CORINE biotopes classification (Devillers *et al.*, 1991) from which the original list of habitats for Annex I was selected and then the Palearctic classification (Devillers & Devillers-Terschuren, 1996). Annex I has been progressively modified with the accession of new member states with the most recent version being 2007 and recent changes have been based on the Palearctic classification (Evans, 2006). Although Natura 2000 also protects species listed in Annex II of the Habitats Directive together with selected bird species listed in the Birds Directive it is often considered that the maintenance of a series of habitats in good condition is one of the best ways to conserve species (Bunce et al., 2013)

1.5 Research and Policy

Using a mixture of remote sensing and field methods seems to deliver the best results in mapping habitats. This requires ecologists and remote sensing experts to collaborate closely. Several projects have pioneered the use of field computers. This helps the field surveyor in data capture and eliminates the need to transcribe field notes, potentially removing a source of error. Habitat maps are important for reporting under Article 17 of the Habitats Directive where distribution maps of the Annex I habitat types are required, together with estimates of their total area and trends. Similar information is also required for compiling Red Lists of habitats, typically at the national level and currently under development at the European level.

Habitat maps are also very useful input to processes of spatial planning, including environmental impact assessments (EIAs) and assessments required under Article 6 of the Habitats Directive to protect the Natura 2000 network. They have been used when designing ecological networks from regional to continental scales, as with the Pan-European Ecological Network (PEEN), and are important in implementing the European Commission's Green Infrastructure Strategy.

More recently, the EU's Biodiversity Strategy to 2020 included three targets calling for knowledge on habitats: (a) to fully implement the Birds (Directive 2009/147/EC) and Habitats Directives; (b), to maintain and restore ecosystems and their services; and (c), to increase the contribution of agriculture and forestry to maintaining and enhancing biodiversity.

The most detailed and comprehensive classifications of vegetation types across Europe are provided by phytosociology, the discipline that studies patterns of co-occurring plant species. Phytosociology is based on the concept of association defined by Braun-Blanquet (1928 *in* EEA & MNHN, 2014) as a “*vegetal grouping, more or less stable, and in equilibrium with the environment, characterised by a particular floristic composition, in which some exclusive or almost exclusive elements (characteristic species) reveal with their presence a particular and autonomous ecology*”.

Associations are classified in a hierarchical system. A vegetation series is a list of the associations that could occur on a given area of land which is ecologically homogeneous with the same physical conditions (i.e. climate, soil type, geomorphology) depending on management, extreme events (e.g. storm damage) and processes of vegetation succession. Series are named after their most mature stage, usually the potential natural vegetation (PNV) (see figure 3).

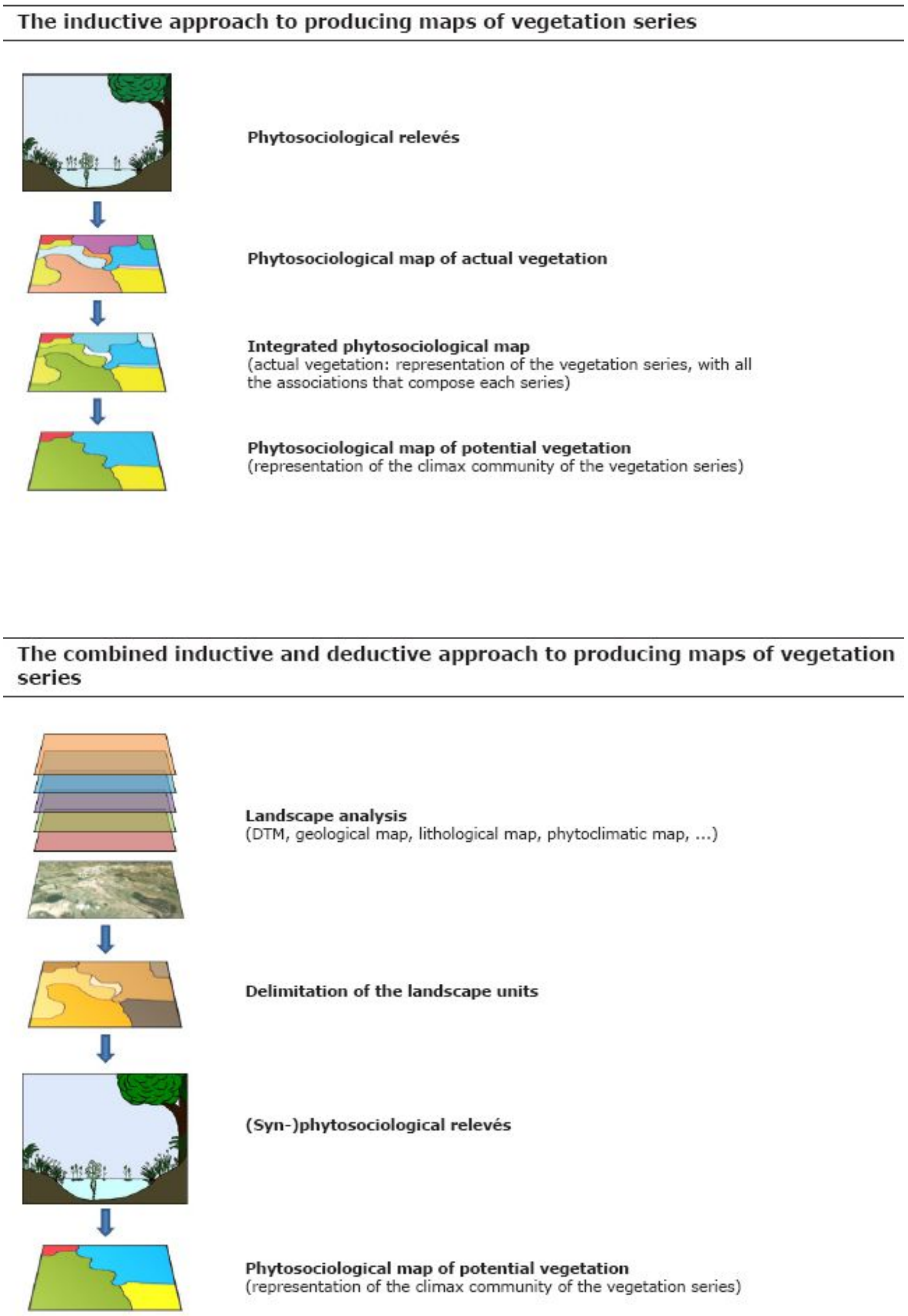

Figure 3: The inductive and the combined inductive and deductive approaches to producing maps of vegetation series (Source: EEA & MNHN, 2014).

There are many types of vegetation maps, produced for diverse reasons. First, maps may show different aspects of vegetation, based on the floristic composition, structure, the ecology of plant communities (synecology), the dynamic stages and relations of plant communities (syndynamics) and the distribution of plant communities (synchorology). Each of these may be represented on a map. Secondly, maps may vary according to scale and definition of the vegetation units. Thirdly, a vegetation map depends on the theoretical conceptions of the different geobotanical schools, and thus on the interpretation and classification of vegetation resulting from these different approaches. The hierarchical system of syntaxa governed by the International Code of Nomenclature (Weber *et al.*, 2000) is based on four principal ranks: association, alliance, order and class. Many authors also recognise sub-ranks (e.g. sub-associations or sub-alliances). Schaminée et al. (2009) showed that more than 1.8 million *relevés*[1] had been already digitised, 75% of which are found in centralised databases of countries or regions.

The term biotope mapping is used as a synonym for habitat mapping in central Europe. Increasingly, especially since the EU Habitats Directive came into force in 1992, maps are being produced which show habitat types or biotopes. Typologies based on phytosociological classification are strictly defined by plant communities, whereas habitat types or biotopes take into account geographic, abiotic and biotic features. The term biotope mapping is used as a synonym for habitat mapping in central Europe (EEA & MNHN, 2014).

The Corine Biotopes classification was published in 1991 (Devillers *et al.*, 1991) as part of the Corine Biotopes project which aimed to identify and describe the habitats of major importance for the conservation within the European Community (then comprising only 12 Member States). It is a hierarchical classification system intended to cover all habitat types but with a focus on natural and semi-natural habitats and a limited coverage of marine habitat types. Although it is clearly based on phytosociological classifications, it also includes other factors like geography, climate and soil, and covers several habitat types with no plant cover (e.g. glaciers and lava tubes). The original version of Annex I of the EU Habitats Directive as published in 1992 is a selection from the Corine biotopes classification (Evans, 2010).

In 1995, the EEA, through its European Topic Centre on Nature Conservation (the ETC/BD's predecessor), began work on the EUNIS habitat classification (Davies *et al.*, 2004): the aim is a comprehensive hierarchical classification of the terrestrial, freshwater and marine habitats for the whole of Europe, associated islands and seas. The EU INSPIRE Directive, which aims to allow for the combination of spatial data and services from different sources across Europe in a consistent way, proposes that the EUNIS habitat classification be used as a common reference for habitats (EEA & MNHN, 2014).

---

[1] A relevé is defined as each of a number of small plots of vegetation, analysed as a sample of a wider area (Oxford Dictionary, 2014 - http://www.oxforddictionaries.com/definition/english/relev%C3%A9).

The General Habitat Categories (GHC) was a classification model developed as part of the EU-funded BioHab and EBONE projects (EBONE, 2015). Tested in Europe, and for non-European Mediterranean and desert environments, the approach has been applied successfully in field inventories and for linking remote sensing information with in situ data. As habitat is a key entry to other biodiversity stock and change variables, it is important to integrate approaches.

In the EU, the most important development is the INSPIRE Directive that entered into force in May 2007. It establishes an infrastructure for spatial information to support Community environmental policies and policies or activities which may have an impact on the environment. Interoperability is understood as providing access to spatial data sets through network services, typically via the Internet. Specific data specifications are defined for habitats and biotopes. The habitat types from Annex I of the Habitats Directive and the EUNIS habitat classification have been adopted as the principal reference lists, and to be INSPIRE-compliant, all habitat features must have one or two habitat type encodings, an obligatory code using either Annex I or the 'EUNIS habitat classification' and an optional second code from a national or local habitat classification system, as long as they are well accepted, registered and documented.

Where a few years ago biodiversity conservation policies primarily focused on species and ecosystem conservation and restoration, the political focus on biodiversity has now extended to the maintenance or restoration of ecosystem services (Intergovernmental Platform on Biodiversity & Ecosystem Services (IPBES),1 EU biodiversity strategy to 2020 (EC, 2011), TEEB (2010). But also in the development of other policy frameworks such as the greening of the European Union Common Agricultural Policy, inclusion of payments for ecosystem services is considered (EC, 2010).

The current trend in policy development inevitably generates an increasing need to be informed on the status of ecosystem services and thus a need for relevant indicators. With indicators, policy-makers can identify and prioritise interventions through a more goal-orientated and time-efficient approach (Layke *et al.*, 2012). The need to monitor changes in ecosystem services provisioning has already been identified at a global level by the Group on Earth Observations Biodiversity Observation Network (GEOBON, 2011). With the recent green lights for setting up the IPBES, the demand for monitoring data on ecosystem services will become even more prominent. Within the European Union, several environmental and biodiversity monitoring schemes have been proposed and implemented, and data is collected from EU-wide general land cover mapping to specific red list species in Annex I habitats. These monitoring schemes have been developed and implemented to monitor changes, to identify and to analyse trends, to support and/or to evaluate policy effectiveness (Geijzendorffer & Roche, 2013).

A map is a representation of the world and cannot depict its true complexity: it is produced for a specific objective. Therefore a balance must be found between the scale and the resulting precision, the type of object mapped and the level of detail required and the extent of the map.

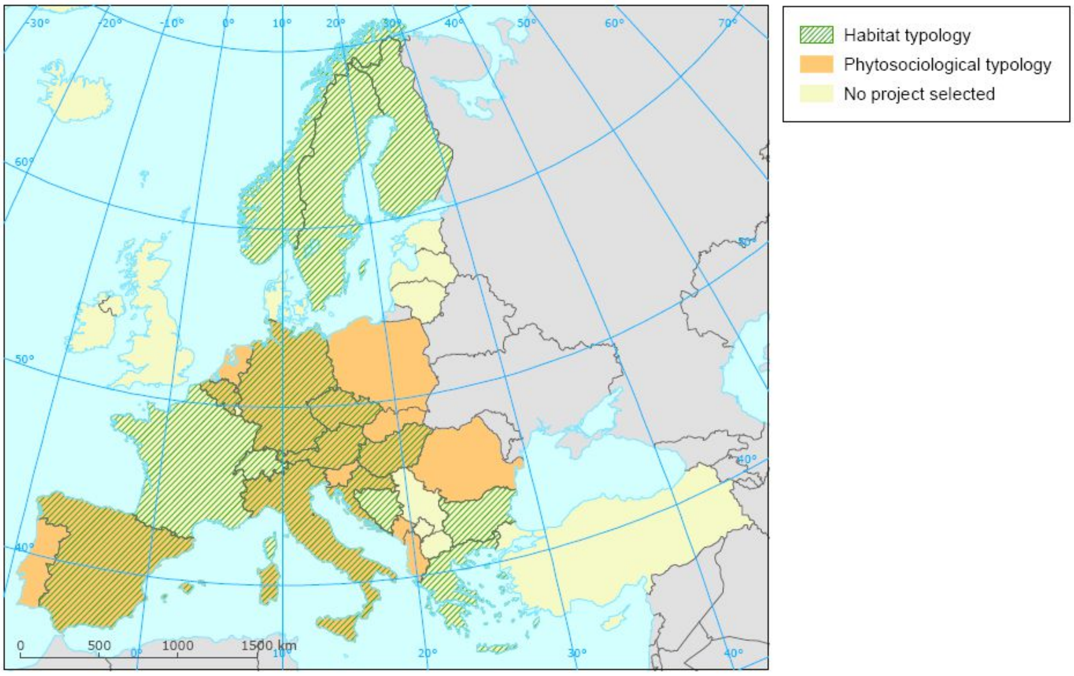

Figure 4: Typologies used by selected habitat-mapping projects in Europe (Source: EEA & MNHN, 2014).

Up to 45 potential natural vegetation (PNV) maps were identified in 24 European countries (see figure 4); most of them (86%) are at landscape scale (i.e. 1:100,000 or smaller). According to EEA & MNHN (2014), the only large-area PNV maps at large scale (i.e. 1:50,000) are from Spain (Basque country, Catalonia and Navarre) and Slovenia (see figure 4) (Noirfalise, 1987 *in* EEA & MNHN, 2014).

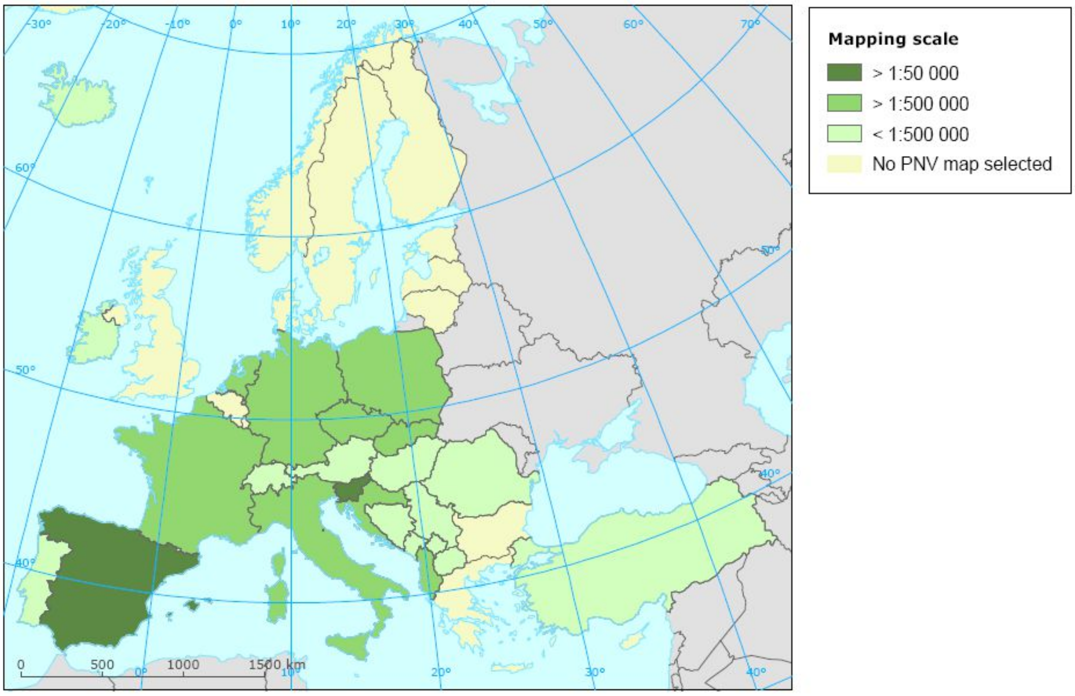

Figure 5: National or regional maps of PVN in Europe (EEA & MNHN, 2014).

In Greece, an important project aimed to identify, describe and map all habitat types in all 237 terrestrial Sites of Community Importance (SCIs) (20,000 km²). The project (1999–2001) was mainly designed for inventory purposes including detailed characterisation of the vegetation communities and mapping. A second project (2013–2015) is using the same methodology but with a focus on monitoring. The vegetation relevés taken within each site were used to identify and describe the vegetation communities, and thus to document the presence, extent and spatial distribution of Annex I habitat types present in Greece (85), as well as a number of habitat types considered of Greek importance (30) (Dimopoulos *et al.*, 2012).

1.6 Remote Sensing and Monitoring Ecosystems

Remote sensing plays an important role in assessing the condition of protected areas and facilitating this broadening of focus from protected areas to entire landscapes. For example, resource managers and conservation practitioners are making extensive use of land-cover and land-use information to portray and analyze the landscape context of conservation areas at multiple scales. Data gathered by remote sensing for the same areas over time are being used to assess changes in landscapes and associated factors, again at multiple scales (Wiens *et al.*, 2009).

Moreover, remote sensing data sets are increasingly being considered by EU Member States, in order to fulfil their reporting obligations under the Habitats Directive (Lengyel *et al.*, 2008). However, the use of satellite-based remote sensing for accurate, detailed and complete conservation status assessment and monitoring of natural and semi-natural habitats, as required under the Habitats Directive, is still rare (Vanden Borre *et al.*, 2011). The coupling of remote sensing and field data can result in an increase in precision and in area estimates of various habitat classes (McRoberts *et al.*, 2002).

The best way forward in modelling vegetation and habitat distributions is to combine top-down modelling with bottom-up knowledge. However, exploitation of bottom-up knowledge demands considerable efforts in terms of data collection and harmonisation (EEA & MNHN, 2014).

The adequacy and quality of spatial data sets and data sources is an important consideration. The choice of the spatial resolution depends on the spatial scale, the distribution and the heterogeneity of the species and habitats being monitored, the factors that control species distributions, and the availability of ancillary data sets related to, for example, soils, drainage networks, geology, topography, population and/or management regimes, that provide additional insights required for interpretation of remote sensing data sets (Nagendra, 2001).

	Very high spatial resolution (e.g. aerial photos, IKONOS, QuickBird, GeoEye, WorldView-2)	**Medium-to-high spatial/temporal resolution (e.g. Landsat, IRS, SPOT)**	**Coarse spatial resolution and very high temporal resolution (e.g. MODIS, AVHRR)**	**Hyperspectral (e.g. MyMap, CASI, Hyperion)**
Level 1 **Distinction between broad physiognomic types: grass, shrub, tree**	++ (besides open water and bare soil)	++ (besides open water and bare soil)	++ (only in landscapes with large vegetation patches)	++ (besides open water and bare soil)
Level 1 **Distinction between the broad physiognomic type: Forest**	++	+ 3 classes: deciduous/pines/other conifers	−/+ 3 classes: deciduous/ coniferous/mixed forest	++
Level 2 **Distinction within the physiognomic type: Grasslads**	+ With multiseasonal imagery: grassland types with different levels of agricultural improvement	++ With multi-seasonal imagery: distinction between marshy grasslands (*Molinia*- or *Juncus*-dominated), unimproved (*Festuca* dominated), semiimproved and improved	−	++ Determining the species composition
Level 2 **Distinction within the physiognomic type: Heathlands**	++ Seasonal phenological variation Can discriminate the evergreen *Calluna vulgaris* from the decidious *Vaccinium myrtillus*	++ With multi-seasonal imagery: distinction between heath types (e.g. *Genista* and *Erica*)	−	++ Distinction between dry and wet heathland, heathland types (*Calluna*, *Molinia*, *Deschampsia*, *Erica* etc.) and heath age classes

Level 2 **Distiction within the type: Wetlands**[2]	+ Detection of riparian vegetation species	+ Seasonal imagery allows mapping the spatial extent of seasonally submerged wetlands and some vegetation species	–	++ Distinction between aquatic macrophytes species (*Typha*, *Phragmites*, *Scirpus*)
Note: The degrees of suitability of the sensor to the identification of a given parameter are: **– = unsuitable** **–/+ = more or less suitable** **+ = suitable** **++ = recommended**				

Table 1: Contribution of various remote sensing techniques to the mapping of natural habitats at two classification levels (Source: EEA & MNHN, 2014).

Remote sensing observations can complement and add to field observations as they deliver a synoptic view and offer the opportunity to provide consistent information in time and space (Nagendra, 2001; Nagendra & Rocchini, 2008; Vanden Borre *et al.*, 2011). For the purpose of habitat monitoring, remote sensing methods and especially hyperspectral techniques are promising, but existing remote sensing data and classification methods fall short in several aspects: (a) airborne hyperspectral data are suitable, but coverage is still limited; (b) existing methods have not addressed the issue of habitat structure and functioning, which is a key factor for assessing habitat quality; and (c) most existing remote sensing methodologies have not been tested vigorously for operational purposes (Hufkens *et al.*, 2010).

Hyperspectral sensors offer finer spectral measurements than multispectral instruments, with often hundreds of spectral bands of narrow width being recorded, allowing a near continuous spectrum to be reconstructed for each pixel. This presents opportunities for more precise identification of biochemical and biophysical properties of the vegetation compared to when broadband multispectral sensors are used. New spaceborne hyperspectral sensors are on their way, in parallel to the existing very high spatial resolution (VHSR) multispectral sensors such as Worldview-II and (with a spatial resolution of 2 m for the 8 multispectral bands and 0.5 m for the

---

[2] Wetlands are not a physiognomic type per se, but are various physiognomic types that have adapted to the continuous or temporary presence of water

panchromatic band). For example, Italy's ASI space agency plans to launch PRISMA, a medium-resolution hyperspectral imaging mission with about 235 channels in the visible, NIR and SWIR wavelength regions, by the end of 2013. The German Aerospace Centre (DLR) and the German Research Centre for Geosciences (GFZ) are planning to launch the EnMAP hyperspectral satellite in 2015 to map the Earth's surface in over 250 narrow wavebands. And in 2015 or 2016, NASA plans to launch the HyspIRI mission, which will acquire medium-resolution imagery across 210 spectral bands. Thus, high resolution multispectral and medium resolution hyperspectral spaceborne data are going to become increasingly available by the end of the decade (Mücher *et al.*, 2013).

Natural complexity can be best explored using spatial analysis tools based on concepts of ecosystems or landscapes as process continuums, which can be partially decomposed into objects or patches. Object based image analysis (OBIA), often referring to object-based image segmentation, classification concepts and tools, has been proposed as a strong toolset to identify, delineate, describe and label the required patches in a consistent way (Blaschke, 2010). Nevertheless, OBIA techniques have been criticised for being still less suitable for the assessment of continuous gradients related to structural and functional processes. Schmidtlein *et al.* (2007) for example combined ordination measures derived from floristic field data with spectral data from HyMap hyperspectral imagery to derive continuous maps which represent abrupt transitions between habitats as well as gradual transitions and within habitat heterogeneity.

Another approach for continuous vegetation mapping is the use of spectral mixture analysis (SMA). In SMA, the reflectance of a single pixel is considered to be a mixture of endmembers, each with a specific spectrum, and each relating to a vegetation or species class present in the pixel. Because the same endmember can be used to analyse a time sequence, SMA has the capability to estimate changes in abundance (Rosso *et al.*, 2005). Hestir *et al.* (2008) also showed the potential of SMA to estimate the spatial distribution and abundance of invasive species and vegetation. Thus, SMA has great values for monitoring aspects related to habitat structure and function (e.g. grass encroachment), because changes in patterns can be detected and quantified (Mücher *et al.*, 2013).

The choice of an appropriate scale, or spatial resolution, for a particular application depends on several factors. These include the information desired about the ground scene, the analysis methods to be used to extract the information, and the spatial structure of the scene itself. In most scientific endeavors the investigator selects the scale at which observations are collected. However, when using remotely-sensed imagery from space-borne sensors, investigators are limited to specific scales of observations. The appropriate scale for observations is a function of the type of environment and the kind of information desired. The techniques used to extract information from imagery also interact with these variables to influence the selection of an appropriate scale. Thus, the problem of selecting an appropriate scale is fairly complex.

The elements in a scene model may vary, depending on the interests of the investigator. For example, in a forest, we may be interested to consider individual leaves, branches, trees, or stands of trees. Common backgrounds in a forest scene include soil, snow, and vegetative understory. Nested models of scenes are also possible, in which one level of elements is used to derive the properties of a new level, or larger elements. Again, forest scenes serve as a good example. At one level, the individual trees might serve as elements in a scene model. At the same time, groups of trees, or stands, might serve as a higher level in the scene model. In this situation, the properties of the individual trees are used to determine the characteristics of the stands (Woodcock & Strahler, 1987).

One methodological issue resulting from the observed graphs of local variance as a function of resolution concerns the relationship between the size of the objects in the scene and the spatial resolution of peak local variance. It was initially hypothesized that the peak would occur when the size of the resolution cells matched the size of the objects. However, in each of the graphs with a well developed peak in local variance the peak occurs at a resolution cell size somewhat smaller than the size of the objects in the scene. Boundary pixels have a mix of elements, and reducing the number of mixed pixels reduces confusion in the classification process, re- suiting in higher classification accuracy (Woodcock & Strahler, 1987).

Ideally, the size of the pixel should be matched so that it is one quarter to one third of the size of the smallest patches of habitat, species assemblage or individual plant/tree being mapped. Some studies exploring the use of medium-resolution (few tens of metres) and high-resolution (a few metres) satellite images for assessing plant species richness (Rocchini *et al.*, 2007) or for ecological prediction (Stickler & Southworth, 2008) found that Landsat performed better than IKONOS or QuickBird VHR satellites, across a range of measures of species richness (EEA & MNHN, 2014).

We conclude by commenting on several aspects that may affect the use of remote sensing in conservation: the resolution of the remote sensing data; the value of ground sampling; matching the scale of the data to the conservation objectives; and balancing the costs against the benefits of remote sensing (Wiens *et al.*, 2009).

1.7 Object Based Image Analysis (OBIA)

With the continuously growing availability of the very high resolution (VHR) imagery with the spatial resolution having pixel sizes significantly smaller than the average size of the object of interest, there grows also the need for reliable methods capable to classify them efficiently. As proved already in many studies, object-oriented approach offers an optimal solution for classifying such data. This approach brings the ability to group relatively homogenous pixels into meaningful objects based on their radiometric values and then extract useful extra information such as size, shape, texture or contextual information (Machala & Zejdová, 2014).

The development of object based image analysis (OBIA) stems primarily from the desire to use the important semantic information necessary to interpret an image, which is not presented in single pixels but rather in meaningful objects and their mutual relations. In particular in OBIA, homogeneous image objects at a chosen resolution are first extracted and subsequently classified. In addition to spectral information, this allows a multitude of additional information, such as shape, texture, area, context, topological relationship with other objects, and information from other object layers, to be derived from objects and used in image classification (Shackelford & Davis 2003).

Pixel-based classification identifies the class of each pixel by comparing its value with the training data and allocates it to a proper class based on a certain algorithm. In the classification based on segmentation result, image is firstly segmented and then classified based on the mean spectral information of the segments. OBIA in eCognition comprises two parts: multi-resolution segmentation and context-based classification. Segmentation, the first step in the object-oriented approach, involves merging the pixels in the image into image object primitives called objects or segments with a certain heterogeneous and homogeneous criterion. This step is critical because segmentation generates the objects that will be treated as a whole in the classification (Mitri & Gitas, 2004).

Multi-resolution segmentation allows generating image objects on an arbitrary number of scales taking into account criteria of homogeneity in colour and shape. Additionally, the created segments are embedded into a hierarchical network in which each object knows its neighbouring objects in horizontal and vertical direction (Baatz & Schape, 1999). The image objects can then be described and classified by an extensive variety of features that include colour, texture, form, and context properties in several forms. This is usually done with a standard nearest neighbour classifier (NN) or fuzzy membership functions, or a combination of both. The variety of object features can be used either to describe fuzzy membership functions, or to determine the feature space for NN (Baatz & Schape, 1999; Gao *et al*., 2007). OBIA, which is based on a fuzzy concept, is an approach that uses not only spectral information but also spatial information. Fuzzy theory replaces the 'yes' or 'no' in the binary theory by the continuous (0–1), where 0 means 'exactly no' and 1 means 'exactly yes'; thus all values between 0 and 1 represent a more or less certain status of yes and no (Mitri & Gitas, 2004).

eCognition Developer 8.64 software (formerly Definiens) of Trimble Germany GmbH (München, Germany), which was specifically created as an instrument for OBIA analyses, was chosen for the purposes of this study. However, trial and error is still a standard approach of eCognition to finding proper segmentation parameters for achieving a proper segmentation of objects of interest. In the segmentation, operator's knowledge of the image and experience of the segmentation process play an important role for the success of the segmentation (Zhang *et al*., 2010).

1.8 Segmentation

To find the boundary of an image object or segment an object, eCognition implemented a region merging approach to segmentation called "Fractal Net Evolution" approach. This technique starts with individual adjacent pixels as initial objects, and then measures:

(1) the spectral heterogeneity change, $h_{spectral}$, and

(2) the shape heterogeneity change, h_{shape}, between the two neighbor pixels (objects) to determine whether they need to be merged together, or not. Once the two pixels are merged into one object, the region of the object grows one step. This measurement and merging process continues iteratively until a user defined threshold is reached (Zhang *et al.*, 2010). In the figure (6) below the segmentation process is diagrammatically illustrated.

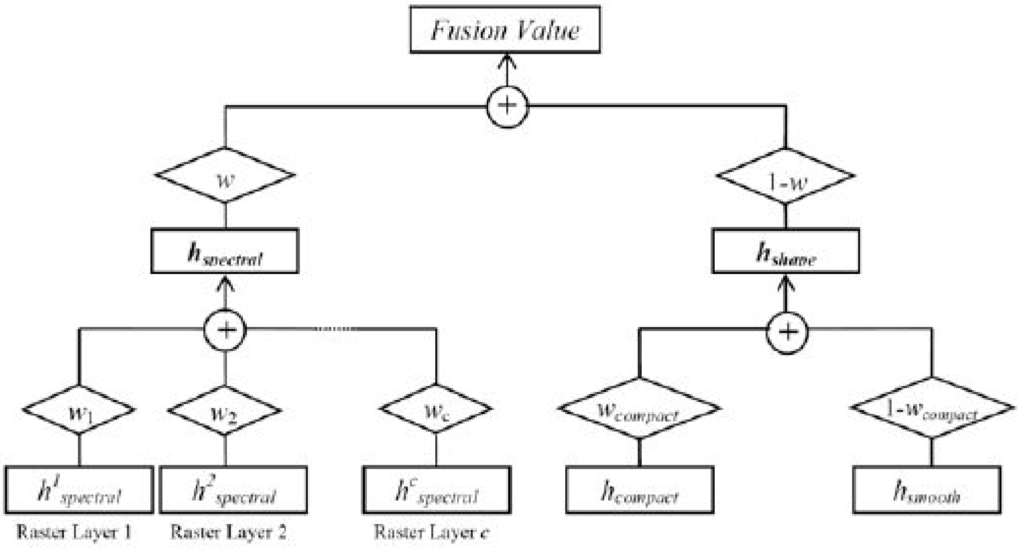

Figure 6: Relationship between the segmentation parameters (user determined weights) in eCognition. Usually, the weights for individual spectral layers (bands) (w_1, w_2, … w_c) are set to 1. Users need to give the value for Smoothness weight ($1-w_{compact}$) (or Compactness weight ($w_{compact}$)) and Shape weight (1-w). The weights ($1-w_{compact}$) and (1-w) are used to calculate the Fusion Value (f). The value f is then compared with a user specified Scale value (s) to estimate whether the two adjacent objects need to be merged, or not (if $f < s^2$, merge the two objects; if $f \geq s^2$, stop the merging) (Source: Zhang *et al.*, 2010).

The region of the object then stops growing, resulting in a one image segment. The region merging and region growing process was designed with the view to meeting six aims (Baatz & Schape, 2000):

a. Production of homogeneous image object-primitives;

b. Adaptability to different scales;

c. Production of similar segment sizes for a chosen scale;

d. Applicability to a variety of data sets;

e. Reproducibility of segmentation results; and

f. Requirement for reasonably fast performance.

The purposes of the segmentation parameters are (Hofmann, 2001):

(1) Scale parameter: influence the average object size. It determines the maximal allowed heterogeneity of the objects. The larger the scale parameter, the larger the objects become.

(2) Shape/Color: adjust the influence of shape vs. color homogeneity on the object generation. The higher the shape value, the less spectral homogeneity influences the object generation.

(3) Smoothness/Compactness: determine the compactness or smoothness of the resulting object. With a selected shape value, the user can influence the compactness or smoothness of the final object.

(4) Image Layer weights: determine the weight of each spectral band in the segmentation. It is used to control the influence of each band on the object generation.

(5) Level settings: determine whether a newly generated image level will either overwrite a current level or whether the generated objects shall contain sub- or super-objects of an existing level. The order of the level generation affects the objects' shape (top-down vs. bottom-up segmentation).

To address the issues existing in the trial-and-error selection of segmentation parameters, a tool for supervised segmentation parameter determination should meet the following requirements (Maxwell, 2005 *in* Zhang *et al.*, 2010):

a. Each execution of the tool is aimed at extracting one land cover type and results in one level of the object hierarchy;

b. Segmentation must be controlled and refined in an iterative manner based on an object model;

c. The tool must rely on an initial segmentation as a start state;

d. Scale, shape, and smoothness parameters must be determined;

e. Parameter selection must be reproducible; and

f. The tool must demonstrate reasonably fast and efficient performance.

The segmentation of an input image is performed on a number of different levels to permit objects of different scales to be extracted on their own level. By using this approach, objects can be classified on the level where the segments are the most meaningful and best represent the object of interest. This infers that the user must have a specific land cover class in mind when segmenting the image so that the parameters can be best estimated and then refined through iteration. As a result, the tool must aim to extract one particular land cover type each time it is executed. By running the tool a number of times, a hierarchy of object levels can then be developed (Zhang *et al.*, 2010).

1.9 Spectral Signatures of Forest Trees

In a time of rapid climate change there is urgency to better characterise and understand ecosystems and the species that live within them. Forest ecosystems present particular challenges, mainly because of the intrinsic difficulties to access. Remote sensing techniques have been used to address some of the problems inherent in forest ecosystem studies. With the advent of sensors capable of collecting high-spectral-resolution radiance data has come the expectation that, if measurements are made with sufficient spatial resolution to avoid spectral mixing, most types of rock, soil and vegetation should be remotely identifiable. However, despite the creation of spectral libraries for various materials and plant species, the unique identification of many materials has proven difficult due to the numerous problems present in real-world measurements, such as angle of view, atmospheric properties, spectral mixture, moisture content and illumination angle, to mention just a few. Furthermore, Price (1994) has suggested that several species may actually have quantitatively similar spectra due to the spectral signature variation present within a species. In short, spectral signatures may not be unique.

The spectral separability of vegetation provides special difficulties because its spectral behaviour is described by a small number of independent variables (Price, 1994). Specifically, the response of vegetation reflectance spectra in visible wavelengths (400–700nm) is primarily determined by the composition and concentration of chlorophyll a, chlorophyll b and carotenoids (Tucker & Garrett, 1977). Conversely, the response of reflectance spectra in the near-infrared wavelengths (700–1300 nm) is a function of the number and configuration of the air spaces that form the internal leaf structure (Danson & Plummer, 1995). In summary, the reflectance of vegetation from different species is highly correlated due to their common chemical composition (Portigal *et al.*, 1997).

In recent years, advances have been made in classifying vegetation using optimal spatial resolutions, red-edge first derivatives and green peak statistical indices (Portigal *et al.*, 1997). Price (1994) has suggested the need to expand spectral libraries such that they can account for intraspecies variability, but there are no guidelines on how to measure such variability. Variance can occur within a species due to micro-climates, soil characteristics, precipitation, topography and a host of other environmental factors (Portigal *et al.*, 1997). In addition, stress factors such as air pollution, heavy metals and drought can change the spectral properties of foliage. Furthermore, both foliage age (for maquis) (Roberts *et al.*, 1998) and position in the canopy (Danson & Plummer, 1995) have been shown to cause substantial differences in the spectral signatures of some species. In addition, an extensive amount of variability is found in the spectral response of foliage within a species and even within a single tree.

Though many problems are posed for the discrimination of different species using remotely sensed data, the potential for separation of different species based on foliar reflectance does exist. Variation of the reflectance from the foliage within a species necessitates the consideration that species inhabit a spectral region and not a specific location. If sufficient data exist, this spectral space can be defined and used directly (shape filtering) or statistically (e.g. red-edge first derivatives[3]), as a superior discrimination tool for classifying spectrally similar entities. Due to the non-unique nature of spectral responses in vegetation, separation of vegetation at the species level is never likely to be perfect, but it can be a useful tool. Variations in leaf angle, crown structure, non-photosynthetic vegetation and other factors will make datasets more complex but need not preclude separation of species. As reflectance from foliage is defined by a spectral shape, so too should the other aspects of vegetation. Therefore, it may be possible to use training sets from high-resolution (spatially and spectrally) data to define the spectral shapes of vegetation classes or species of interest. These shapes can then be modified to optimally discriminate features of interest at a given scale. Misclassifications will occur, but if the imagery scale is smaller than the features of interest, then correctly classified entities should form clusters (e.g. tree crowns), while misclassifications should be more evenly scattered (e.g. individual branches). Therefore, post-classification filtering for noise may improve overall classification accuracy (Cochrane, 2000).

Hyperspectral visible to short wave infrared (VSWIR; 0.4-2.5 µm) imagery has been especially valuable. VSWIR absorption features are dominated by water and pigments within the leaf volume and as these constituents are present in all plants they typically do not produce distinctive signatures unique to individual species. In contrast to their VSWIR spectral behaviour, fresh leaves are particularly opaque in thermal infrared spectra (TIR; 8.0-14.0 µm). Consequently, the spectral response is dominated by the plant tissue that forms the external surfaces, namely the cuticular membrane and the outer cell walls. Different species are known to have a variety of spectral features related to differences in chemical composition of the surface tissues (Ribeiro da Luz & Cowley, 2010).

Challenges to the identification of thermal infrared (TIR) spectral features at the canopy level include the following: leaves have subtle emissivity features that can only be retrieved from at-sensor radiance data by using very effective atmospheric compensation and temperature-emissivity separation methods. Temperature

---

[3] The position of the inflexion point in the red edge (680 nm to 780 nm) is termed the red-edge position (REP) (Cochrane, 2000).

variations inside a canopy due to differential solar heating and variations in leaf angle and shading might impede emissivity retrievals. Also the already weak spectral features of tree canopies might be further attenuated by canopy voids, as well as the superposition of emitted and reflected energy components (Ribeiro da Luz & Cowley, 2010).

Cover type	Approximate height of mature vegetation upper canopy	Ground surface covered by vegetation	Seasonality	Leaf type
Evergreen needleleaf forests	>5m	>60%	Almost all trees remain green all year	Needleleaf
Evergreen broadleaf forests	>5m	>60%	Almost all trees remain green all year	Broadleaf
Deciduous needleleaf forests	>5m	>60%	Trees shed their leaves almost simultaneously in response to dry or cold seasons	Needleleaf
Deciduous broadleaf forests	>5m	>60%	Trees shed their leaves almost simultaneously in response to dry or cold seasons	Broadleaf
Mixed forests	>5m	>60%	Neither broadleaf or needleleaf forest types has <25% or >75%	Interspersed mixtures or mosaics of needleleaf or broadleaf forest types
Woodlands	>5m	Tree canopy cover >40% and <60%	Can be either evergreen or deciduous with woody or herbaceous understories	Either broadleaf or needleleaf

Wooded grasslands/shrublands	>5m	Tree canopy cover >10% and <60%	Can be either evergreen or deciduous with woody or herbaceous understories	Either broadleaf or needleleaf
Closed bushlands or shrublands	Bushes and shrubs <5m	Bush and shrub canopy coverage >40%. Tree canopy coverage is either bare or herbaceous	Shrubs or bushes can be either evergreen or deciduous	Either broadleaf or needleleaf
Open shrublands	Shrubs <2m	Shrub canopy coverage >10% and <40%	Shrubs can be either evergreen or deciduous	NA
Grasses	NA	Continuous herbaceous cover and <10% tree cover	NA	NA
Croplands	NA	>80% covered in crop-producing fields	NA	NA
Bare	NA	<10% vegetated cover during anytime of the year. Includes exposed soil, sand, rocks, snow or ice	NA	NA

Table 2: Definitions, land cover types and characteristics (Source: De Fries *et al.*, 1998).

In a study by De Fries *et al.* (1998), the spectral signatures of cover types with regard to mean annual NDVI[4] and maximum annual NDVI values suggested that it is possible to classify almost all pixels in the global land mass as one of the 13 cover types listed in figure 6. There is however overlap between some of the cover types, for example woodlands and wooded grasslands, indicating the not unexpected requirement to discriminate between cover types with metrics in addition to mean and maximum annual NDVI values. This study also indicates that some cover types are not normally distributed, that is they are clearly multimodal, for example needleleaf evergreen forest. The classification algorithm therefore needs to be based on non-parametric statistics or the cover types need to be further subdivided into homogeneous clusters (De Fries *et al.*, 1998).

According to Ribeiro da Luz and Cowley (2010), successful plant species identification using TIR canopy measurements appears to involve at least five factors: 1) Spectrum shape and contrast — the greater the spectral contrast and the more diagnostic the shape, the better the identification success; 2) Morphology of leaves — larger leaves with relatively simple shapes and large surface areas give a more distinct TIR spectral response; 3) Disposition of leaves — planophile canopies give a better spectral response than canopies with leaves arranged in drooping or erectophile configurations, both of which tend to accentuate blackbody behavior; 4) Canopy closure — some canopies naturally contain more voids between leaves and/or between layers of leaves, tending to dilute the total canopy spectral response; 5) Size of the canopy — larger canopies may be discernable even when their spectral contrast with other scene materials is only moderately strong.

For example, *F. grandifolia* (Beech) had one of the best identification results. This species was found to show high spectral contrast (approx. 6%), to have medium-sized leaves with relatively smooth surfaces and margins, and a closed planophile canopy. Large leaf size and canopy closure are important because this increases the chance that at least some pixels will be filled by leaves rather than canopy voids. Larger leaves also help to ensure that the sensor FOV is filled by emitters at or near the same temperature. This facilitates an accurate temperature–emissivity separation.

---

[4] The Normalized Difference Vegetation Index (NDVI) is a simple graphical indicator that can be used to analyse remote sensing measurements and assess whether the target being observed contains live green vegetation or not.

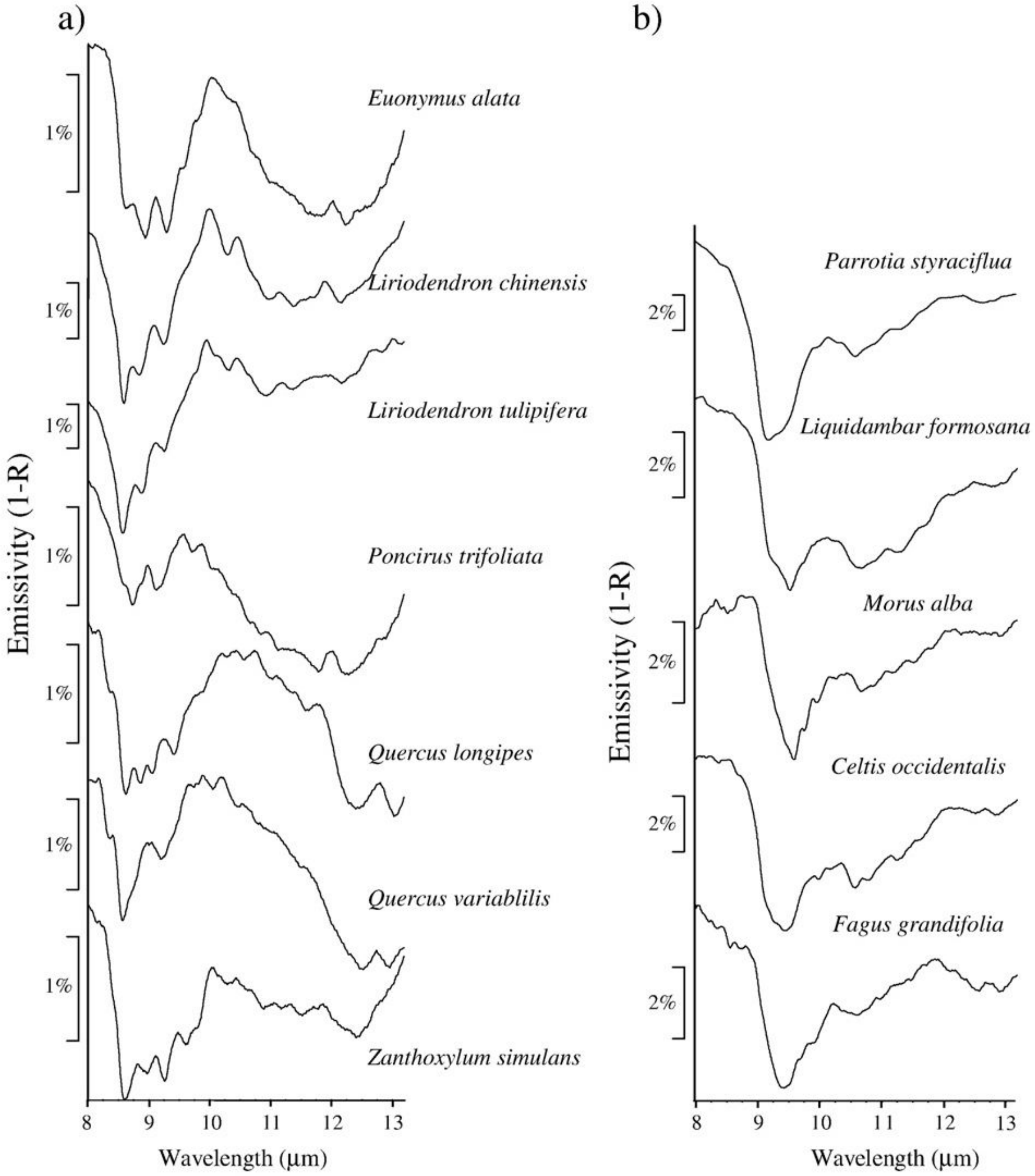

Figure 7: Some species have similarities in composition that may cause spectral confusion. a) Species that show spectral similarities related to cutin-rich cuticles. b) Species that show spectral similarities related to silica-rich cuticles (Source: Ribeiro da Luz & Cowley, 2010).

Another example is pine, which exhibits the higher radiance in the visible bands is a consequence of the lack or reduction of leaf pigments. Chlorophyll a and b, A Carotene and ß xanthophyll cause a strong absorption in the region about 0.445jnm, while chlorophyll also absorbs in the red region (0.645jurn). Therefore, the values of burned vegetation are higher in the blue and red bands. On the other hand, the scorched pine displays a lower reflectance in the near infrared as a result of the deterioration in the internal cellular structure of the leaf (Chuvieco & Congalton, 1988).

2. Methods

2.1 Study Area

2.1.1 Geography

The University Forest of Taxiarchis is located on the southern and southwestern slopes of Mount Cholomontas in Chalkidiki, in the Central Macedonia region. It extends from 40°23′E to 40°28′E and 23°28′N to 23°34′N and covers an area of 60 km^2 (see figure 1). The terrain of the study area is diverse and very rough at places as a result of sharp alterations in altitude, which ranges between 320 and 1200 m. The Mediterranean climate of the area is characterised by short periods of drought, hot summers and mild winters. Main characteristic of the climate is the large fluctuations of rainfall during summer as well as the double dry season (July and September) with limited duration and intensity (Mallinis *et al.*, 2014).

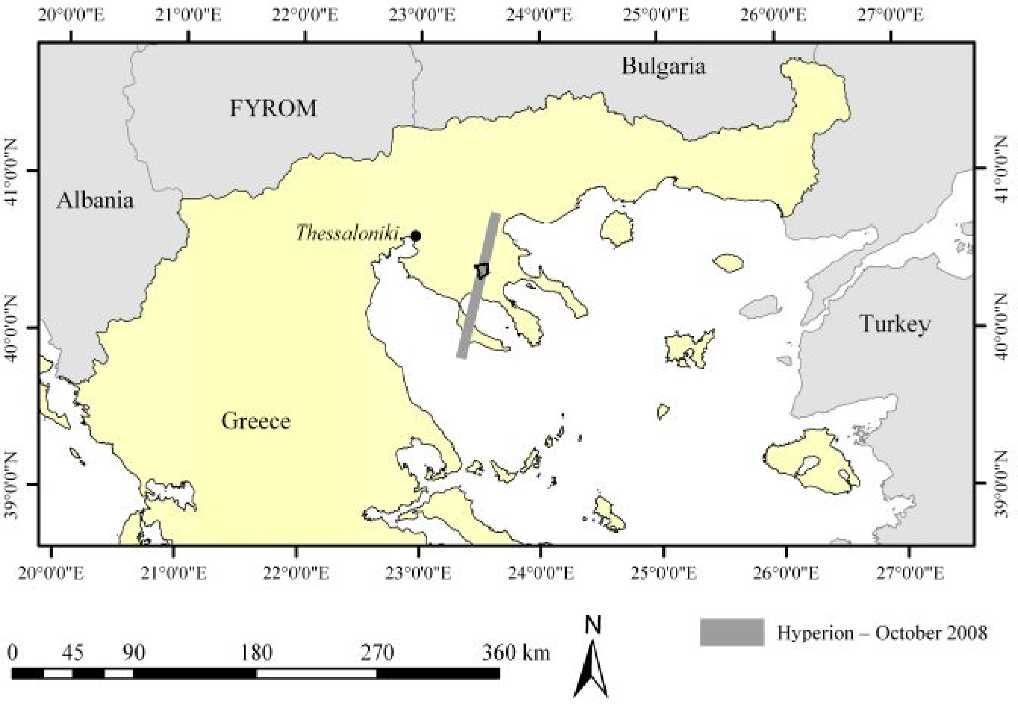

Figure 8: Location of the study area and spatial extent of the Hyperion imagery (Source: Stavrakoudis *et al.*, 2014).

The study area forms a complex mosaic. Common forest species are Italian oak (*Quercus frainetto*), Calabrian pine (*Pinus brutia*), Black pine (*Pinus nigra*) and Beech (*Fagus sylvatica*). Forest tree communities mainly comprise of mixed stands, as deciduous species have gradually invaded the areas occupied by pines. In addition, patches within the forest are covered with maquis species (*Quercus ilex*, *Quercus coccifera*, *Erica arborea*, etc.), low herbaceous vegetation and scattered oak trees (Mallinis *et al.*, 2008).

There are mainly deciduous forests in this area, which is divided in three zones: *Quercetalia ilicis*, *Quercetalia pubescentis* and *Fagetalia*. These zones are formed based on flora composition, altitude, petrology, soil conditions, the exposure and incline of the slopes, air temperature and rainfall. The area is mostly covered with broad-leaved oak trees. The flora of the area also includes beech trees, black pine trees, brutian pine trees and Aleppo pine trees, as well as other ligneous plants, such as *Quercus ilex*, *Erica arborea* (a plant of beekeeping interest), holly oak trees, arbutus trees, *Fraxinus* trees, plane trees, willow trees, etc. Hence, there are about 60 ligneous plant species and more than 200 herbaceous plant species. The area is also home to rich fauna, including large populations of wild boars. The animal species displayed in the museum can also be found in the forest. Villagers coexist harmoniously with wild boars and refrain from poaching (Aristotle University of Thessaloniki, 2014).

Broad-leaved species that grow in Greece prevail in the area of the university forest. They are regenerated naturally and, when weather conditions are adverse, they are artificially regenerated. The systematic and sustainable management of the forest over the last decades has encouraged local populations to continue to reside in their villages. The main forest products include oak, beech, pine firewood and charcoal. Since the forest is not mature enough, little timber is produced (wooden beams, planks, parquet elements, etc.). In total, 30-35 people work in the timber industry every year. Fir trees are also very important to the region; they are planted by villagers in order to sell them as Christmas trees. Villagers have been trading Christmas trees for 30 years. There are more than 2 million fir trees in the area, offering income opportunities to villagers, protecting the land and providing shelter to wildlife (Aristotle University of Thessaloniki, 2014).

The University Forest area is also part of the NATURA2000 network (GR1270001-Oros Cholomontas) (Mallinis *et al.*, 2014). Moreover, Mount Cholomontas was granted protection under an EU order, mainly with regards to the predator birds living in the forest; there are many wildlife shelters in the forest, where any form of hunting is forbidden (Aristotle University of Thessaloniki, 2014).

Implementing a different policy for sustainable forestry development, focusing on forest preservation and, at the same time, trying to meet human needs, the University Forest Administration and Management Fund has spent money on the following infrastructure:

- A large forest road network (A-B-C category),
- A firebreak and water intake network, observation posts and a state-of-the-art remote sensing system for additional firebreak protection,
- Two shelters for wildlife, covering an area of 3,000 hectares,
- A large number of experimental fields, established in collaboration with the Faculty of Forestry and Natural Environment,
- Projects to promote tourism in the area, such as constructing trails and greenways, an artificial lake, stands, kiosks, as well as embellishing chapels, etc.

A sufficient number of building facilities has been constructed over the years in the area of the University Forest, which houses the administration offices and offers accommodation for the administrative personnel, teaching personnel, students and researchers who carry out various projects. The building complex has many dormitories, a restaurant, laboratories, storerooms and two conference halls.

The Forest Museum is also housed in the building facilities of the University Forest. Native flora and fauna, as well as natural resources are displayed in the museum, which was founded in 2008. Its founding was funded by the Aristotle University Property Development and Management Company. There are special cases in the museum where aspects of forest management planning are represented, and stuffed birds and animals are displayed. Moreover, all plant and seed species displayed, as well as multimedia displays provide visitors and students, who specialise in the field of forestry, with information. The Forest Museum at the University Forest in Taxiarchis offers visitors and students of the Faculty of Forestry and Natural Environment training seminars, as well as environmental education, whilst promoting tourism in the area (Aristotle University of Thessaloniki, 2014).

2.1.2 The trees of Taxiarchis forest

Among several tree species present in Taxiarchis University Forest, we selected those with representation in two or more sample patches of the ground sampling. The tree species' categories, used in the classification classes of this study are listed and described below. Please note that all the tree species are referred to for the most part of this study, using the name, which is also used in the Aristotle University management plan, however each class is also taxonomically defined below:

- **Maquis**

Figure 9: Acer platanoides (Wikipedia, 2015).

Common name: Norway maple

Species: *Acer platanoides*

Other closely related species present in the area: *Acer campestre*

Family: Aceraceae

Height: 25 m

Shape: Broadly columnar

Leaf persistence: Deciduous

Native region: S.W. Asia, Europe

Habitat: Mountain woods

Leaves: Palmately lobed, up to 15 cm long and 17.5 cm across, with five lobes, each lobe ending in several teeth with long, slender points, bright green, smooth when mature on both sides, turning yellow or sometimes red in autumn; the long, slender leaf stalks exudes milky juice when cut.

Bark: Grey and smooth.

Flowers: Small and bright yellow-green, borne in conspicuous clusters in spring before and with the youngest leaves.

Fruit: With large, spreading wings, up to 5 cm long.

Remark: A fast-growing species, which quickly reaches its maximum height. In cultivation, it has many ornamental forms, selected for both foliage and habit.

- **Oak**

Figure 10: *Querqus cossifera* L.

Common name: Turkey oak

Species: *Querqus cerris* (*Querqus coccifera* L.)

Other closely related species present in the area: *Quercus ilex*, *Quercus pubescens*, *Quercus petraea*, *Quercus frainetto*

Family: Fagaceae

Height: 35 m

Shape: Broadly spreading

Leaf persistence: Deciduous

Native region: C. and S. Europe

Habitat: Woods

Leaves: elliptic to oblong, up to 12 cm long and 7.5 cm across, deeply lobed, toothed, glossy dark green above, downy when young becoming smooth beneath.

Bark: Dark grey-brown, thick, rough and deeply ridged.

Flowers: Males in yellow-green, drooping catkins, females inconspicuous, borne separately on the same plant in early summer.

Fruit: An acorn, up to 2.5 cm long, one-half enclosed in a cup, the cup covered in long, slender scales.

- **Castanea**

Common name: Sweet chestnut

Species: *Castanea sativa*

Other closely related species present in the area: *Castanea vesca*

Family: Fagaceae

Height: 30 m

Shape: Broadly columnar

Leaf persistence: Deciduous

Native region: N. Africa, S.W. Asia, Europe

Habitat: Woods

Leaves: Oblong, up to 20 cm long and 7.5 cm across, usually rounded or heart-shaped at the base, taper-pointed at the tip, toothed, glossy dark green and smooth above, paler becoming smooth beneath.

Figure 11: *Castanea sativa* (Wikipedia, 2015).

Bark: Grey and smooth, becoming brown and usually spirally ridged with age.

Flowers: Males and females both small and creamy yellow, in catkis up to 25 cm long, separate, but usually on the same spike in the summer.

Fruit: A spiny husk, up to 6 cm across, enclosing one to three edible, glossy, red-brown nuts.

- **Fir**

Common name: King Boris Fir, Bulgarian Fir

Species: *Abies borisii regis*, *Abies alba* (silver fir) subspecies *acutifolia*

Other closely related species present in the area: *Pseudotsuga menziesii*

Figure 12: *Abies borisii regis*

Family: Pinaceae

Height: 40 m

Shape: Narrowly conical

Leaf persistence: Evergreen

Native region: Bulgaria, northern Greece, Albania, and former Yugoslavia

Habitat: Mountain forests

Leaves: Linear, up to 3 cm long, with a notched tip, glossy dark green above, with two whitish bands beneath, spreading either side of the shoot, shorter and pointing forward above.

Bark: Grey and smooth, cracking into small plates with age.

Flowers: Males yellow, beneath the shoot, females green, upright, borne in separate clusters on the same plant in spring.

Fruit: A cylindrical upright cone, up to 15 cm long, green at first ripening to brown, with protruding, down-turned bracts.

- **Beech**

Common name: Balkan beech

Species: *Fagus moesiacae*, considered the same species as the Crimean beech, *Fagus taurica* and a hybrid between *F. orientalis* and *F. sylvatica* (often referred to as a subspecies of *F. sylvatica*)

Other closely related species present in the area: *Fagus sylvatica*

Family: Fagaceae

Height: 30 m

Shape: Broadly spreading

Leaf persistence: Deciduous

Native region: S.E. Europe

Habitat: Hills and mountains

Figure 13: Fagus moesiacae (National Park Sutjeska, 2015).

Leaves: Elliptic to obovate, up to 12 cm long and 6 cm across, usually with a wavy margin, untoothed or slightly toothed, with up to 12 pairs of veins beneath, turning yellow in autumn.

Bark: Grey and smooth, sometimes furrowed.

Flowers: Males and females both small, males yellow, females green, in separate clusters on the same plant in mid-spring.

Fruit: A bristly husk, up to 2.5 cm long, enclosing one to three small, edible nuts.

- **Pinus brutia**

Common name: Turkish pine, Calabrian pine

Species: *Pinus brutia* (sometimes considered a subspecies of *Pinus halepensis*)

Other closely related species present in the area: *Pinus halepensis, Pinus pinaster*

Figure 14: *Pinus brutia*

Family: Pinaceae

Height: 35 m

Shape: Narrowly columnar

Leaf persistence: Evergreen

Native region: S.E. Europe

Habitat: Mountains

Leaves: Needle-like and stiff, in pairs, slender, mostly 10–16 cm long, bright green to slightly yellowish green.

Bark: Orange-red, thick and deeply fissured at the base of the trunk, and thin and flaky in the upper crown

Flowers: Males yellow, females red in separate clusters on the young shoots in late spring to early summer.

Fruit: Stout, heavy and hard, 6–11 cm long and 4–5 cm broad at the base when closed, green at first, ripening glossy red-brown when 24 months old.

- **Pinus nigra**

Common name: Austrian pine

Species: *Pinus nigra*

Family: Pinaceae

Height: 40 m

Shape: Broadly columnar

Leaf persistence: Evergreen

Figure 15: *Pinus nigra*

Native region: C. and S.E. Europe

Habitat: Mountains and hills, often on limestone

Leaves: Needle-like and stiff, up to 15 cm long, in pairs, sharp-pointed, very dark green, on stout, glossy brown shoots.

Bark: Nearly black, scaly, ridged.

Flowers: Males yellow, females red in separate clusters on the young shoots in late spring to early summer.

Fruit: An egg-shaped, brown cone, up to 8 cm long.

- **Pinus sylvestris**

Figure 16: *Pinus sylvestris* (Wikipedia, 2015).

Common name: Scots pine

Species: *Pinus sylvestris*

Family: Pinaceae

Height: 35 m

Shape: Broadly spreading

Leaf persistence: Evergreen

Native region: Asia, Europe

Habitat: Mountains, on sandy or gravelly soil.

Leaves: Needle-like stout, and twisted, up to 7 cm long, in pairs, blue-green to blue-grey.

Bark: Purple-grey, peeling in irregular plates; orange and flaking towards the top of the plant.

Flowers: Males yellow, females red, in separate clusters on young shoots in late spring to early summer.

Fruit: An egg-shaped cone, up to 7.5 cm long, green ripening to brown.

Remark: This species makes a broadly spreading tree in open situations, but is narrow in confined spaces.

- **Pinus halepensis**

Figure 17: *Pinus halepensis* (Greenscenelandscape, 2015).

Common name: Aleppo pine, Jerusalem pine

Species: *Pinus halepensis*

Other closely related species present in the area: *Pinus pinaster*, *Pinus brutia* (often considered a subspecies of Aleppo pine), *Pinus sylvestris*

Family: Pinaceae

Height: 25 m

Shape: Broadly columnar

Leaf persistence: Evergreen

Native region: Mediterranean region

Habitat: Hills and mountains

Leaves: Very slender, up to 12 cm long, distinctly yellowish green, and produced in pairs (rarely a few in threes).

Bark: Orange-red, thick, and deeply fissured at the base of the trunk, and thin and flaky in the upper crown.

Flowers: Males yellow, females red, in separate clusters on young shoots in late spring to early summer.

Fruit: Narrow conic, up to 12 cm long and 3 cm across at the base when closed, green at first, ripening glossy red-brown when 24 months old. They open slowly over the next few years, a process quickened if they are exposed to heat such as in forest fires.

- **Pinus maritime**

Common name: Maritime pine

Species: *Pinus pinaster*

Figure 18: *Pinus pinaster*

Other closely related species present in the area: *Pinus Halepensis*, *Pinus Brutia*, *Pinus sylvestris*

Family: Pinaceae

Height: 35 m

Shape: Broadly columnar

Leaf persistence: Evergreen

Native region: N. Africa, S.W. Europe

Habitat: Sandy soil

Leaves: Needle-like and stiff, up to 20 cm long, in pairs, sharp-pointed, grey-green becoming dark green, borne on stout shoots.

Bark: Purple-brown, ridged, deeply-fissured.

Flowers: Males yellow, females red, in separate clusters on the young shoots in early summer.

Fruit: A conical, glossy brown cone, up to 20 cm long, the scales with sharp prickles, persisting for many years.

- **Pinus radiata**

Common name: Monteray pine

Species: *Pinus radiata*

Other closely related species present in the area:

Family: Pinaceae

Height: 30 m

Shape: Broadly conical

Leaf persistence: Evergreen

Native region: USA - California

Habitat: Dry slopes, near coast.

Figure 19: Pinus radiata (Wikipedia, 2015).

Leaves: Needle-like and slender, up to 15 cm long, in clusters of three, bright green on grey-green shoots.

Bark: Dark grey, deeply fissured.

Flowers: Males yellow-brown, females red-purple, in separate clusters on the young shoots in early summer.

Fruit: A brown cone, up to 12 cm long, persisting for years.

(Coombes, 1992; Aristotle University of Thessaloniki, 2013; Filotis, 2015)

A full list of tree species found in Taxiarchis forest can be found in Appendix VI.

2.1.3 Ground Derived Vector Data and Tree Distribution

The classes used for all classifications were based on a field study by the Aristotelian University of Thessaloniki, as shown in the map below (figure 20), illustrating the distribution of tree species and habitats.

It should be noted that the tree species' names in the key presented in figure 21 are based on those used in the forest management plan, compiled by the Department of Forestry of the Aristotle University of Thessaloniki. Thus certain disambiguations concerning the names name used in the study, the common name, the species name and the common Greek name of each tree may be resolved by referring to appendix VII.

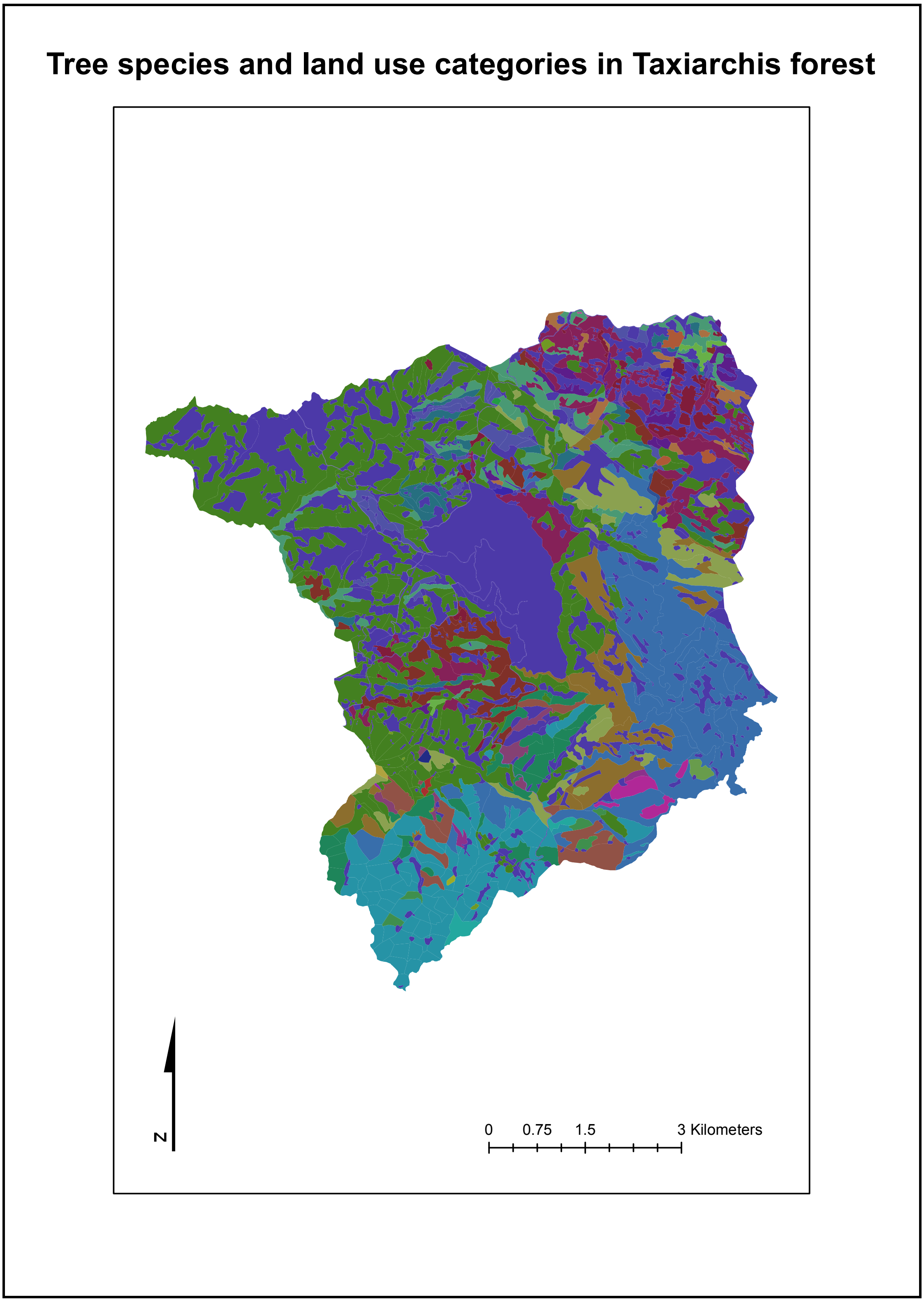

Figure 20: Tree species distribution in Taxiarchis Forest (see figure 21 for a colour-tree species index table)

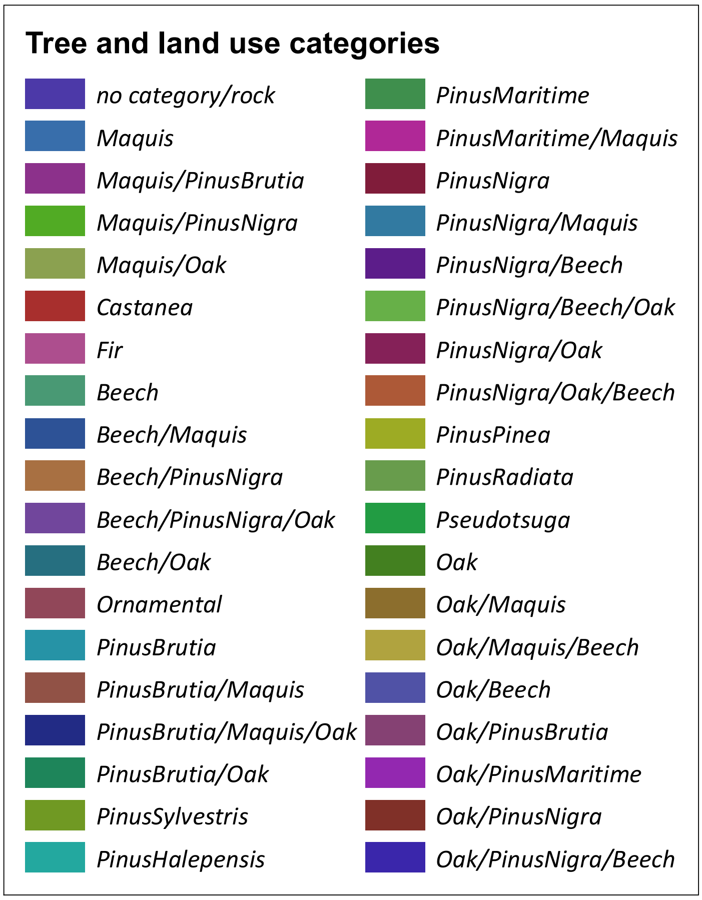

Figure 21: Colour-tree species index key.

2.2 Satellite and Aerial Imagery

The imagery used in this study includes satellite and aerial imagery of varying spatial resolutions and band range (see figure 2 for methodology outline diagram). The multispectral satellite imagery used includes Landsat 8 OLI (low resolution) and GeoEye - 2 (high resolution) imagery, while the hyperspectral imagery includes both satellite and aerial imagery, Hyperion (low resolution) and CASI (high resolution) respectively. The date each image was taken, as well as their spatial resolution is listed in table 3, below.

Imagery	Date data was acquired	Spatial resolution
Landsat 8 OLI	1/6/2013	15 m
GeoEye - 2	19/4/2013	0.5 m
Hyperion	10/2008	30 m
CASI	25/7/2013	2 and 5 m

Table 3: Date of data acquisition and spatial resolution of satellite and aerial imagery.

The following sections of this chapter provide a description of the sensors and the characteristics of these images used.

2.2.1 CASI

CASI (Compact Airborne Spectrographic Imager) is a VIS/NIR pushbroom imaging spectrograph[5] with a reflection grating and a two-dimensional CCD (charge coupled device) solid-state array detector. This relatively lightweight and compact instrument may be flown on light aircraft, helicopters or mounted on a lift. The instrument

---

[5] Pushbroom imaging spectrograph = An imaging spectrometer is an instrument used in hyperspectral imaging and imaging spectroscopy to acquire a spectrally-resolved image of an object or scene, often referred to as a datacube due to the three-dimensional representation of the data. A push broom scanner is a technology for obtaining images with spectroscopic sensors, regularly used for passive remote sensing from space and in spectral analysis on production lines, for example with near-infrared spectroscopy (NASA, 2013).

operates by looking down in a fixed direction and imaging successive lines of the scene under the platform, building up a two-dimensional image as the platform moves forward. The CASI instrument has been used in a variety of applications from forest cover mapping to pollution monitoring.

Details:

The CASI instrument is composed of 6 components weighing a total of 55 kg. The components are:

Instrument Control Unit

- Keyboard Unit
- Power Supply Unit
- Sensor Head Unit
- Video Display Unit
- 60 Hz Inverter

The CCD sensor is a P86520 series frame transfer device. The array is thermoelectrically cooled to reduce dark current. The imaging area of the array is 512 x 288 pixels with each element measuring 15.5 by 22 um. The instrument can be run on 110 volts at 2.4 amps. For DC operation the inverter supplied with the system requires 28 VDC, 13 amps peak. For the optional gyro another inverter supplies 400Hz AC.

The 512 image pixels across the field of view (FOV) of 35 degrees give a 1.23 meter ground resolution (cross track) per 1 km AGL altitude. The along track ground resolution is approximately the product of the integration time and the aircraft speed. The required integration time is directly proportional to the number of bands collected in spatial mode or in spectral mode the number of views. For example, if the aircraft speed is traveling at 51 m/s (100 knots), and the CASI sensor integration time is 100 ms the along track pixel size is 5.2 m.

The CCD sensor is read out and digitized to 12 bits by a programmable electronics system which is controlled by an internal single-board computer. Data are recorded on a built-in digital recorder (Exabyte) which uses 8mm video cassettes as the recording medium. This gives up to two gigabytes of data per tape. The frame rate is configuration dependent up to a maximum of 85 lines/sec. The CCD can be read out to select and sum groups of rows, to create high spatial resolution bands, or sample columns from the array, to create high spectral resolution views. This capability allows the instrument to operate in different modes, as follows:

1) Imaging mode (Spatial). This mode has 512 spatial pixels across a 35 degree swath. The user selects the band center spectral row (wavelength) and number of spectral rows to sum (bandwidth) to create up to 15 non-overlapping bands.

2) Multispectrometer mode (Spectral). All 288 spectral rows are sampled in up to 39 view directions across 35 degree swath. The view directions are user selected columns from the CCD. There is a programmable scene recovery Band in this mode. The scene recovery Band gives all 512 CCD elements (pixels) at one wavelength (i.e. one spectral row).

3) Full-frame mode. The device samples all 288 spectral rows for all 512 spatial columns. This mode requires long image recording times limiting it to stationary or slow moving platforms (NASA, 2013).

In this study the Multispectrometer mode (spectral) was used for the data collection.

2.2.2 Landsat

The Landsat 8 satellite images the entire Earth every 16 days. Data collected by the instruments onboard the satellite are available to download at no charge from GloVis, EarthExplorer, or via the LandsatLook Viewer within 24 hours of reception.

Landsat 8 carries two instruments: The Operational Land Imager (OLI) sensor, which includes refined heritage bands, along with three new bands: a deep blue band for coastal/aerosol studies, a shortwave infrared band for cirrus detection, and a Quality Assessment band. The Thermal Infrared Sensor (TIRS) sensor provides two thermal bands. These sensors both provide improved signal-to-noise (SNR) radiometric performance quantized over a 12-bit dynamic range. (This translates into 4096 potential grey levels in an image compared with only 256 grey levels in previous 8-bit instruments). Improved signal to noise performance enable better characterisation of land cover state and condition. Products are delivered as 16-bit images (scaled to 55,000 grey levels) (see appendix I) (USGS, 2014).

The data (satellite images) used in this study were from Landsat 8 were taken on the 1st of June 2013. The spatial resolution of the images is 30 m, but combining data from the panchromatic spectrum, this was 15 m.

2.2.3 GeoEye

The GeoEye-1 satellite sensor was launched on September 6, 2008. This satellite provides a resolution of 0.46 meters. The GeoEye-1 satellite collects images at 0.41-meter panchromatic (black-and-white) and 1.65 meter multispectral resolution. The satellite can collect up to 350,000 square kilometers of pan-sharpened multispectral imagery per day. This capability is ideal for large-scale mapping projects. GeoEye-1 can revisit any point on Earth once every three days or sooner.

The GeoEye-1 satellite sensor was successfully launched on September 6, 2008. The satellite, which was launched at Vanderberg Air Force Base, California, provides a resolution of 0.46 meters. The GeoEye-1 Satellite sensor is optimized for large projects, as it can produce over 350,000 square kilometers of pan-sharpened multispectral satellite imagery every day.

GeoEye-1 has been flying at an altitude of about 681 kilometers and is capable of producing imagery with a ground sampling distance of 46 centimeters, meaning it can detect objects of that diameter or greater.

During late summer of 2013 the orbit altitude of the GeoEye-1 Satellite sensor was raised to 770 Km/ 478 Miles. GeoEye-1 new nadir ground sample distance (GSD) is 46cm compared to the previous GSD of 41cm.

Sensor specifications:

Resolution	0.46 m / 1.51 ft* panchromatic (nominal at Nadir) 1.84 m / 6.04 ft* multispectral (nominal at Nadir)
Spectral Range	Panchromatic: 450 - 800 nm Blue: 450 - 510 nm Green: 510 - 580 nm Red: 655 - 690 nm Near Infra Red: 780 - 920 nm

Table 4: Sensor specifications for GeoEye satellite data (Source: Satellite Imaging Corporation, 2014)

2.2.4 Hyperion

The Hyperion instrument provides a new class of Earth observation data for improved Earth surface characterisation. The Hyperion provides a science grade instrument with quality calibration based on heritage from the LEWIS Hyperspectral Imaging Instrument (HSI). The Hyperion capabilities provide resolution of surface properties into hundreds of spectral bands versus the ten multispectral bands flown on traditional Landsat imaging missions. Through these spectral bands, complex land ecosystems can be imaged and classified.

The Hyperion provides a high resolution hyperspectral imager capable of resolving 220 spectral bands (from 0.4 to 2.5 µm) with a 30-meter resolution. The instrument can image a 7.5 km by 100 km land area per image, and provide detailed spectral mapping across all 220 Bands with high radiometric accuracy. The major components of the instrument include the following:

- System fore-optics design based on the Multi-Purpose Satellite (KOMPSAT) Electro Optical Camera (EOC) mission. The telescope provides for two separate grating image spectrometers to improve signal-to-noise ratio (SNR).
- A focal plane array which provides separate Short Wavelength Infrared (SWIR) and Visible and Near Infrared (VNIR) detectors based on spare hardware from the LEWIS HSI program.
- A cryocooler identical to that fabricated for the LEWIS HSI mission for cooling of the SWIR focal plane.

Hyperspectral imaging has wide ranging applications in mining, geology, forestry, agriculture, and environmental management. Detailed classification of land assets through the Hyperion will enable more accurate remote mineral exploration, better predictions of crop yield and assessments, and better containment mapping (USGS, 2011).

2.2.5 ASTER Global Digital Elevation Model (ASTER GDEM)

The ASTER Global Digital Elevation Model (ASTER GDEM) is a joint product developed and made available to the public by the Ministry of Economy, Trade, and Industry (METI) of Japan and the United States National Aeronautics and Space Administration (NASA). It is generated from data collected from the Advanced Spaceborne Thermal Emission and Reflection Radiometer (ASTER), a spaceborne earth observing optical instrument. The aim of the project is to develop a user-friendly topographic information data set of the global terrain. The ASTER Global Digital Elevation Model (ASTER GDEM) is a DEM data which is acquired by a satellite-borne sensor "ASTER" to cover all the land on earth.

The ASTER GDEM is the only DEM that covers the entire land surface of the Earth at high resolution. Since the release of the Version 1 on June 29, 2009, the ASTER GDEM has been widely used by many users and it has greatly contributed to the global earth observing community.

Version 2 of the ASTER GDEM is developed, employing an advanced algorithm to improve GDEM resolution and elevation accuracy and reprocessing a total of 1.5 million scene data including additional 250,000 scenes acquired after the previous release. Accuracy of this latest version is validated by the collaborate effort between Japan and the United States, which shows significant improvements over Version 1. The ASTER GDEM Version 2 was formally released as an upgrade to Version 1 on October 17, 2011 (ASTER GDEM, 2011).

The spatial resolution of ASTER GDEM, used here has a spatial resolution of 25 m.

2.3 Pre-Processing

Pre-processing of remotely sensed images is a preparatory phase that, in principle, improves image quality for further analyses. Corrections, such as noise removal and adjustments, such as orthorectification are described below for each imagery used. The quality of these processing steps may affect the final outcome of classification to a high degree, as we will see in the results and discussion sections.

2.3.1 Vegetation Sampling – Vector Data

A Training and Test Area (TTA) mask was generated, based on field sampling vector data, as illustrated in figure 20 for each of the categories of interest. Figure 21 includes a reference colour index of the tree species and combined categories (this key can be referred back to throughout this study). Training samples were created using a TTA mask of randomly selected samples (simple random sampling) from the vegetation ground data presented in figure 20 (these training samples will be illustrated in the results section and are mentioned here because they are derived from the TTA masks of figures 22 and 23 depending on the categories used). The random selection of tree category data samples and TTA generation was carried out using the QGIS software.

For the classification, two sets of categories were used and assessed for their accuracy in each image dataset, group A and group B. Not all classes of tree species were used, due to the fact that certain classes were represented in only one restricted in area polygon, which was not considered sufficient or indicative as spectral signature sample. Group A included all categories, of satisfactory representation in the study area, including mixed and non-mixed categories, which were represented in the ground-data (used to generate samples) by two or more polygons, while group B included only non-mixed tree species categories.

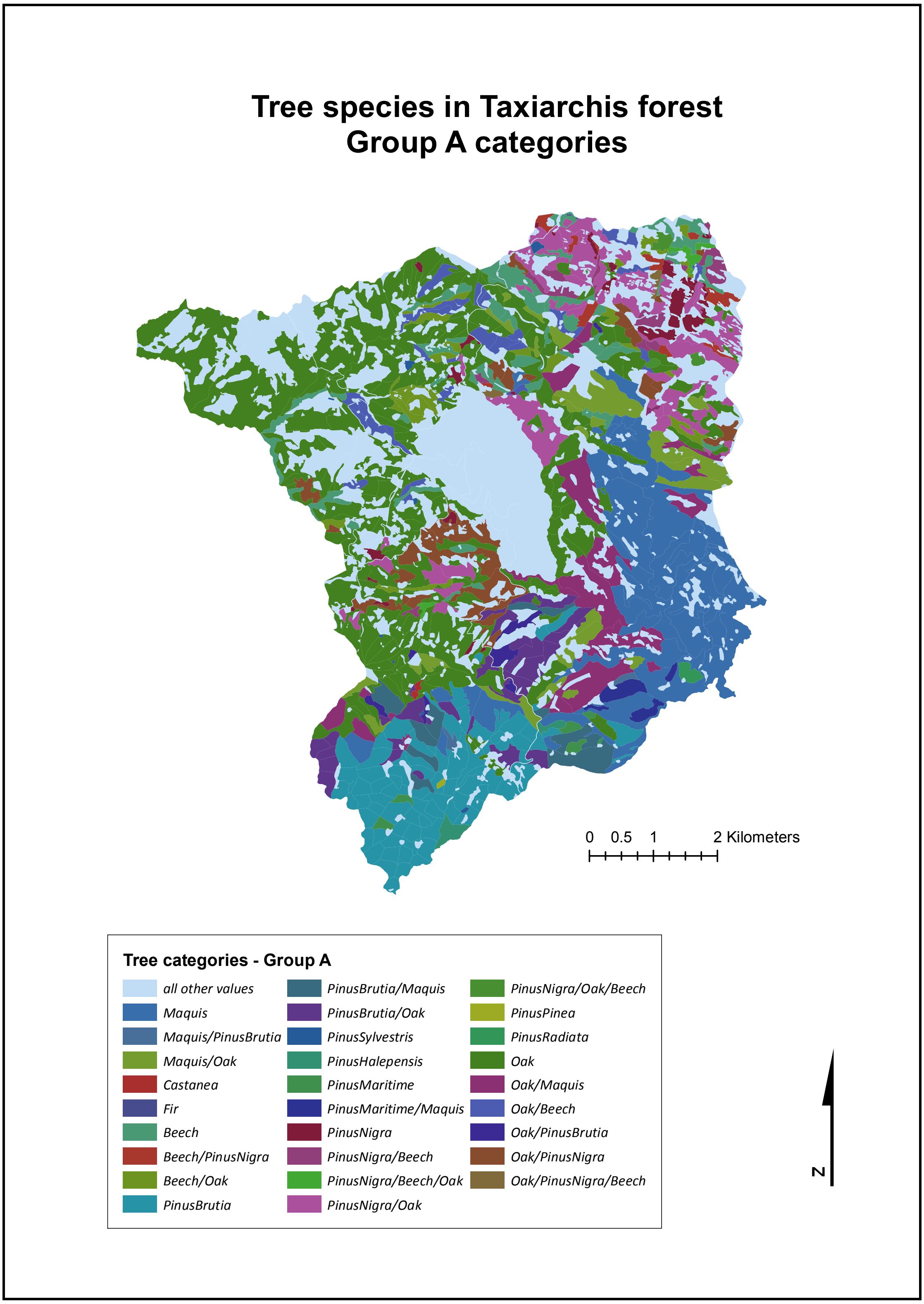

Figure 22: Group A categories and map (TTA mask for samples and accuracy evaluation for group A categories generated from this template of forest tree species' distribution).

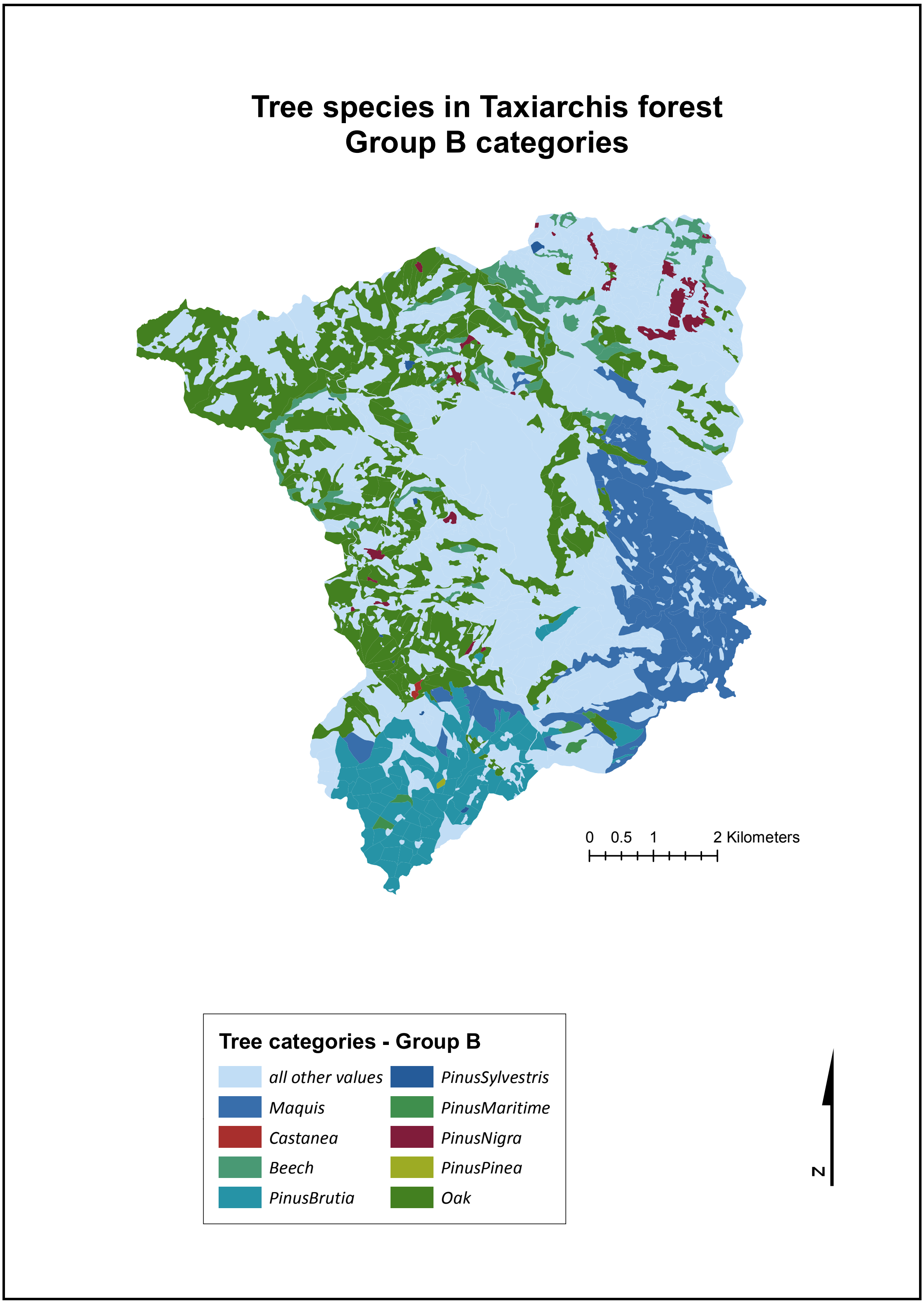

Figure 23: Group B categories and map (TTA mask for samples and accuracy evaluation for group B categories generated from this template of forest tree species' distribution)

It should be noted that the samples of group B categories were not considered satisfactory in number and distribution and thus in certain projects samples were taken manually for classes Castanea, *Pinus sylvestris*, *Pinus maritime* and *Pinus pinea*.

The accuracy in all cases was evaluated using the classification result compared to the complete TTA mask of species for each category group, as illustrated in figures 22 and 23 for categories of group A and B respectively.

2.3.2 ASTER GDEM

We have produced slope and aspect maps (layers) based on the GDEM with specialised filters using the ER Mapper software.

Slope is measured in % with 200% corresponding to a 90° slope and aspect measured in degrees (0-361° with 361 corresponding to horizontal areas).

The ASTER GDEM layers were included in all projects and have a spatial resolution of 25 m.

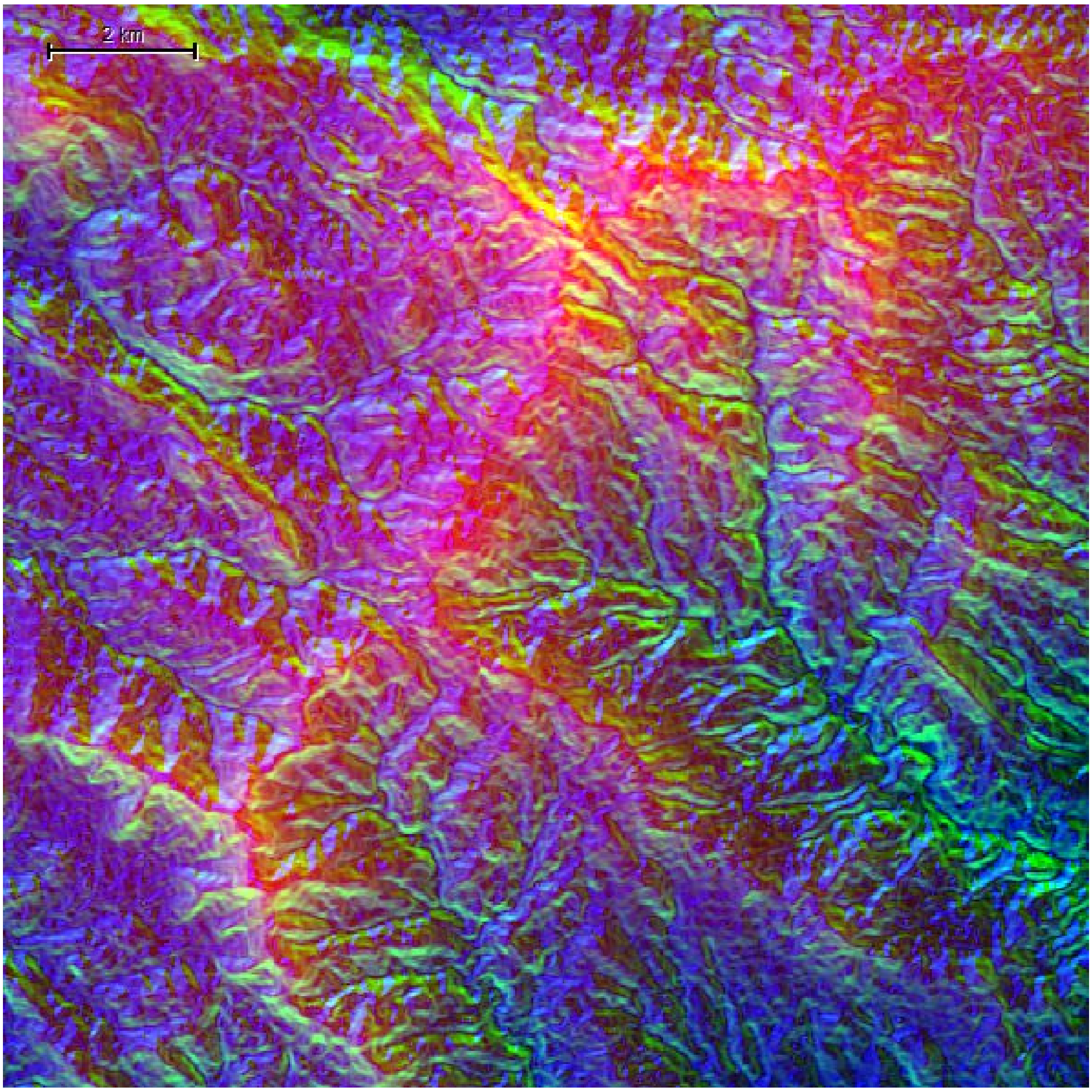

Figure 24: Aster GDEM imagery for Taxiarchis forest, which includes three layers: elevation, slope and aspect.

2.3.3 Satellite and Aerial Imagery

2.3.3.1 CASI

Radiometric correction, as well as orthorectification was performed to bring the remotely sensed data into registration with the topographic maps and to make the images geographically comparable. The imagery was also subjected to mosaicing. Mosaicing is one of the techniques of image processing which is useful for tiling digital images. Mosaicing is blending together of several arbitrarily shaped images to form one large radiometrically balanced image so that the boundaries between the original images are not seen. In addition, geometric corrections included adjustments, compensating for any tilt of the aircraft, as well as the agglutination of the strips.

The influence of the atmospheric degradation was reduced by radiometric correction, using the ATCOR 4 software, in order to correct any influence from clouds or other atmospheric factors affecting the reflectance at the time of the data collection. Both atmospherically and non-atmospherically corrected CASI images were used for classification, in order to assess the quality of each imagery and of the atmospherical correction process. In addition, CASI images of spatial resolutions 2 and 5 m were also used and tested.

2.3.3.2 Landsat

The imagery used was taken from Landsat 8 OLI and was already radiometrically corrected and orthorectified. Pansharpening was also performed using the LMVM method. The spatial resolution of the image is 30 m, but in merging it with the panchromatic bands, the resolution became 15 m (USGS, 2014).

2.3.3.3 GeoEye - 2

Orthorectification was performed to bring the remotely sensed data into registration with the topographic maps and to make the images geographically comparable. The ENVI software tool was used for geometric corrections, while the imagery was already radiometrically corrected. Pansharpening was performed using the LMVM method, as well as subsetting of the image.

The spectral bands for the GeoEye image include the following:

- Panchromatic: 450 - 800 nm
- Blue: 450 - 510 nm
- Green: 510 - 580 nm
- Red: 655 - 690 nm
- Near Infra Red: 780 - 920 nm

The panchromatic band was fused with other bands giving a spatial resolution of 0.5 m.

2.3.3.4 Hyperion

The Hyperion imagery was already radiometrically corrected and orthorectified. No further pre-processing was performed other than subsetting of the image. Hyperion provides imagery with 30 m spatial resolution imagery over a 7.5 km wide swath perpendicular to the satellite motion (see appendix II).

The image comprises a total of 242 contiguous spectral bands. Of these, 196 are well calibrated, but 24 bands are considered uncalibrated because they do not meet the desired performance requirements or are noisy. Bands with very low SNR (signal-to-noise ratio) and strong atmospheric water absorption features were also removed. Specifically, 87 bands were removed spanning the spectral ranges: 355.6–416.6 nm, 935.6–935.6 nm, 942.7–962.9 nm, 1346.3–1467.3 nm, 1800.3–1971.8 nm, 2002.1–2022.3 nm, and 2365.2–2577.1 nm. From the remaining 155 bands, those which were not calibrated were also removed (according to appendix II), leaving 31 channels, which were used for the classification.

2.3.4 Feature Extraction Methodology for Hyperspectral Images

Hyperspectral imagery includes a large number of bands, which make these files particularly heavy and the process of analysing them particularly time-consuming independent of the quality of hardware. In addition, hyperspectral remote sensing provides very high spectral resolution image data and the potential for discrimination of subtle differences in ground covers. High-dimensional data spaces are mostly empty, indicating that the data structure involved exists primarily in a subspace. As a result, there is a need for feature extraction methods that can reduce the dimensionality of the data to the right subspace without losing the original information that allows for the separation of classes. In other words, dimension reduction is the transformation that brings data from a high order dimension to a low order dimension, thus overcoming the "curse" of dimensionality (Plaza *et al.*, 2005).

2.3.4.1 Principal Component Analysis (PCA)

The principal component analysis is based on the fact that neighboring bands of hyperspectral images are highly correlated and often convey almost the same information about the object. The analysis is used to transform the original data so to remove the correlation among the bands. In the process, the optimum linear combination of the original bands accounting for the variation of pixel values in an image is identified. The PCA employs the statistic properties of hyperspectral bands to examine band dependency or correlation. Though, one may find many synonyms for PCA, such as the Hotellling transformation or Karhunen-Loeve transformation (Gonzalez & Woods 1993), all these transformations are based on the same mathematical principle known as eigenvalue decomposition of the covariance matrix of the hyperspectral image bands to be analyzed. Below is a brief formulation of the principle (Rodarmel & Shan, 2002).

An image pixel vector is estimated with the following formula:

$$x_i = [x_1, x_2 \ldots\ldots x_N]_i^T \qquad (1)$$

with all pixel values x_1, x_2,…….x_N at one corresponding pixel location of the hyperspectral image data. The dimension of that image vector is equal to the number of hyperspectral bands N. For a hyperspectral image with m rows and n columns there will be M=m*n such vectors, namely i=1,…,M. The mean vector of all image vectors is denoted and calculated as:

$$m = \frac{1}{M}\sum_{i=1}^{M}\left[x_1, x_2 \ldots x_N\right]_i^f \qquad (2)$$

The covariance matrix of x is defined as:

$$Cov(x) = E\left\{(x - E(x))(x - E(x))^T\right\} \qquad (3)$$

where:

E = expectation operator;

T superscript = transpose operation;

and

Cov = notation for covariance matrix.

The covariance matrix is approximated via the following calculation:

$$c_x = \frac{1}{M}\sum_{i=1}^{M}(x_i - m)(x_i - m)^T \qquad (4)$$

The PCA is based on the eigenvalue decomposition of the covariance matrix, which takes the form of:

$$C_x = ADA^T \qquad (5)$$

Where:

$$D = diag(\lambda_1, \lambda_2 \ldots \lambda_N) \qquad (6)$$

is the diagonal matrix composed of the eigenvalues λ_1, $\lambda_2 \ldots \lambda_N$ of the covariance matrix C_X, and A is the orthonormal matrix composed of the corresponding N dimension eigenvectors a_k (k=1,2,…, N) of C_X as follows:

$$A = (a_1, a_2, \ldots . a_N) \qquad (7)$$

The linear transformation defined by:

$$y_i = A^T x_i (I = 1,2,\ldots.., M) \qquad (8)$$

is the PCA pixel vector, and all these pixel vectors form the PCA (transformed) bands of the original images.

Let the eigenvalues and eigenvectors be arranged in descending order so that $\lambda_1 > \lambda_2 > \ldots > \lambda_N$, thus the first K (K < N, usually K<<N) rows of the matrix A^T, namely the first K eigenvectors $a_j^T\,(j = 1,2,....K)$, can be used to calculate an approximation of the original images in the following way:

$$z_i = \begin{bmatrix} z_1 \\ z_2 \\ \vdots \\ z_K \end{bmatrix}_i = \begin{bmatrix} a_{11} & a_{12} & \cdots & a_{1K} & \cdots & a_{1N} \\ a_{21} & a_{22} & \cdots & a_{2K} & \cdots & a_{2N} \\ \vdots & \vdots & \vdots & \vdots & \vdots & \vdots \\ a_{K1} & a_{K2} & \cdots & a_{KK} & \cdots & a_{KN} \end{bmatrix} . \begin{bmatrix} x_1 \\ x_2 \\ \vdots \\ x_K \\ \vdots \\ x_N \end{bmatrix} \left(i = 1,2,....M \right) \qquad (9)$$

where pixel vector z_i will form the first K bands of the PCA images.

Such formed PCA bands have the highest contrast or variance in the first band and the lowest contrast or variance in the last band. Therefore, the first K PCA bands often contain the majority of information residing in the original hyperspectral images and can be used for more effective and accurate analyses because the number of image bands and the amount of image noise involved are reduced. According to Gonzalez and Woods (1993), the PCA bands are mutually independent or orthogonal and their covariance matrix takes the form of:

$$C_z = diag(\lambda_1, \lambda_2 ... \lambda_K) \qquad (10)$$

The geometry of the PCA concept is illustrated in Figure 25, where the original data consist of two bands, band 1 and band 2. There is considerable correlation between the two bands: a move in band 1 creates an almost linear change in band 2. Once the PCA takes place, however, the correlation between the PCA band 1 and 2 vanishes. Another aspect of PCA analysis that can be seen in this illustration pertains to the variability within bands. Once the transformation has taken place, PCA band 1accounts for the maximum amount of variability or contrast possible in the image and PCA band 2 accounts for the second largest amount. This trend is likely to continue in the first few PCA bands, with the remainder containing less and less useful information (Rodarmel & Shan, 2002).

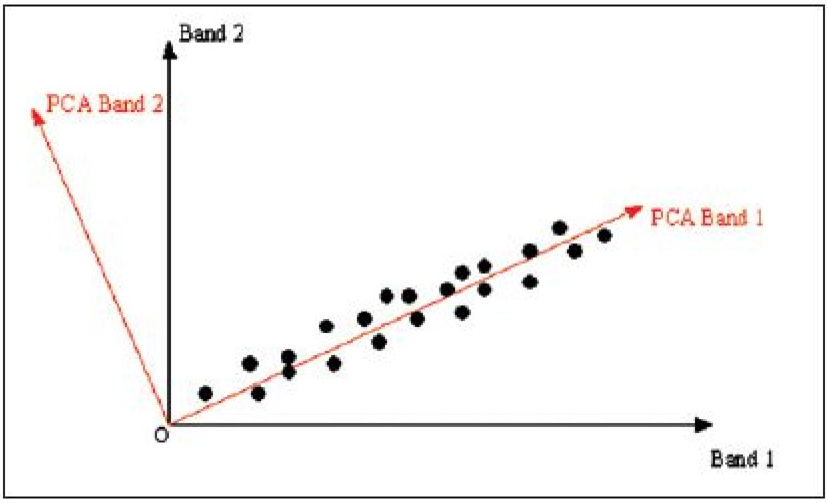

Figure 25: Geometry of the principal component analysis and PCA bands (source: Rodarmel & Shan, 2002)

2.3.4.2 Minimum Noise Fraction Transform (MNF)

In 1988, Green *et al.* first presented the MNF transform method. The MNF transform generates new components ordered by image quality and provides better spectral features in major components than the PC transform method, no matter how the spectral noise is distributed. Using the theory of MNF, James *et al.* (1990) presented the noise-adjusted principal component (NAPC) transform aiming at the noise characteristics of GER hyperspectral scanner. The most important work in MNF transform is to accurately estimate the noise covariance matrix (NCM) (Xiang *et al.*, 2009).

One of the most common measures of image quality is the signal-to-noise ratio. Thus, instead of choosing new components to maximize variance, as the principal components transform does, we now choose them to maximize the signal-to-noise ratio. Our choice should then achieve the desired optimal ordering in terms of image quality. This transformation can be defined in several ways. It can be shown that the same set of eigenvectors is obtained by procedures that maximize either the signal-to-noise ratio or the noise fraction (Green *et al.*, 1988).

Let us consider a multivariate data set of p-bands with grey levels:

$$Z_i(x), \qquad i = 1,\dots,p$$

Where x gives the coordinates of the sample. We shall assume that:

$$Z(x) = S(x) + N(x)$$

Where $Z^T(x) = \{Z(x)\} = \Sigma = \Sigma_S + \Sigma_N$ and $S(x)$ and $N(x)$ are the *uncorrelated* signal and noise components of $Z(x)$. Thus:

$$Cov\{Z(x)\} = \Sigma = \Sigma_s + \Sigma_N$$

Where Σ_S and Σ_N are the covariance matrices of $S(x)$ and $N(x)$ respectively. Note that, although we are assuming additive noise, the techniques described in principle can also be applied to multiplicative noise by first taking logarithms of the observations.

We define the noise fraction of the i^{th} band to be:

$$Var\{N_i(x)\}/Var\{Z_i(x)\}$$

the ratio of the noise variance to the total variance for that band. The maximum noise fraction (MNF) transform chooses linear transformations:

$$Y_i(x) = a_i^T Z(x) \qquad\qquad i = 1,\dots,p$$

such that the noise fraction for $Y_i(x)$ is maximum among all linear transformations orthogonal to $Y_j(x), j = 1,\dots,i$.

Using arguments similar to those used in the derivation of principal components, it can be shown that the vectors a_i are the left-hand eigenvectors of $\Sigma_N \Sigma^{-1}$, and that μ_i, the eigenvalue corresponding to a_i, equals the noise fraction in $Y_i(x)$. Hence, from the definition of the MNF transform, we see that $\mu_1 \geq \mu_2 \geq \dots \geq \mu_p$, and so the MNF components will show steadily *increasing* image quality (unlike the usual ordering of principal components).

For here onwards, it will be assumed that the eigenvectors a_i are normed so that:

$$a_i^T \Sigma a_i = 1 \qquad\qquad i = 1,\dots,p.$$

This norming is for mathematical convenience only, and has no effect on the noise removal procedures. It will also be convenient at certain points to express the MNF transform in the matrix form:

$$Y(x) = A^T Z(x)$$

Where $Y^T(x) = (Y_1(x),\dots,Y_p(x))$ and $A = (a_1,\dots,a_p)$.

A property of the MNF transform (not shared by principal components) is that, because it depends on signal-to-noise ratios, it is invariant under scale changes to any band. Another useful property is that it orthogonalises $S(x)$ and $N(x)$, as well as $Z(x)$. To obtain the MNF transform, we need to know both Σ and Σ_N. In many practical situations, these covariance matrices are unknown and need to be estimated. Usually, Σ is estimated using the sample covariance matrix of $Z(x)$.

Noise removal

Once data have been transformed into components with decreasing noise fraction (increasing *S/N* ratio), it is logical to spatially filter the noisiest components and subsequently to transform back to the original coordinate system. As the transformed components filtered by this procedure contain a reduced signal component, the resulting signal degradation will be much less than if the same smoothing were performed on the untransformed data. This procedure should allow much more intense smoothing to be applied without serious signal degradation.

Noise reduction is achieved by using the high between band correlation that often exists in the signal components of remotely sensed data. A multivariate signal can be considered to lie between two extremes: perfect between-band correlation and zero between-band correlation. In the former case, we would expect to be able to achieve a maximal noise reduction (viz. var (*S*) /var (*N*) improved by a factor of p if the S/N ratio is constant). In the latter case no improvement can be made by the procedures discussed here. The amount of noise reduction achieved in each situation depends on the degree of between-band correlation, the relative powers of the noise in each input band, and the type of smoothing performed on the transformed components.

In general, although the low-order MNF components contain more noise, they still have a signal constituent. If these signals need to be retained, each MNF component must be filtered before retransformation to obtain a cleaned image. Under these conditions it is difficult to estimate the losses in both signal and noise, as they are dependent upon the nature of the filtering process. However, when the signal content of a MNF component is so low that it can be neglected, it is easy to estimate the signal and noise losses in such a process.

Noise in more than one band

When there is noise in more than one band and its covariance structure is not known, we must find some way of estimating it from the data. In general, this will involve computing the covariance matrix of new variables resulting from some type of spatial filtering of each input band. The selection of the appropriate filter must be determined by the spatial characteristics of the noise that it is designed to isolate, and on the spatial characteristics of the signal in which it is buried. No filter will extract noise completely. Hence, careful analysis will be required to establish the conditions under which the covariance matrix so generated approximates Σ_N (Green *et al.*, 1988).

2.3.5 Feature Selection Methodology for Hyperspectral Images

2.3.5.1 Band selection based on correlation statistics of spectral signatures per classification category

A hyperspectral image can be considered as an image cube where the third dimension is represented by hundreds of contiguous spectral bands. As a result, a hyperspectral pixel is actually a column vector with dimensions equal to the number of spectral bands. Such between-band spectral information is very useful and can be used for spectral characterisation. Many measures proposed in signal processing and pattern recognition can be used for this purpose. Nevertheless, most of them are spatial-based measures, and they are not particularly designed to measure spectral properties inherent in a single pixel vector (Chang, 2003).

Spectral Information Measure is a hyperspectral measure derived from the Kullback-Leibler information distance to capture the spectral variability of a pixel vector. In addition, Spectral Information Divergence is also introduced below. These two measures are analysed in order to explain the theoretical background of the Signature-to-Signature Spectral Correlation (SSSC), which is one of the reprocessing techniques used in this paper (Chang, 2003).

A hyperspectral image is generally acquired by hundreds of spectral channels. As a result, a scene pixel vector is usually presented by a column vector, in which each component contains specific spectral information provided by a particular channel. Therefore, a greater number of spectral channels translate more spectral information provided by a particular channel. This implies that a hyperspectral image pixel vector generally contains more spectral information than does a multispectral image pixel vector. In many situations, such spectral information is valuable and crucial in data analysis. In order to capture and characterise the spectral properties vector provided in a single pixel vector by hundreds bands, the SIM spectral measure is introduced.

The Spectral Information Measure (SIM) is an information theoretic measure that models the spectral band-to-band variability as uncertainty results from randomness. It considers each pixel vector as a random variable with the probability distribution obtained from normalizing its spectral histogram to unity. With this interpretation, SIM can measure the spectral variability of a single hyperspectral pixel vector resulting from band-to-band correlation. It not only can describe the randomness of a pixel vector, but also can generate high-order statistics of each pixel vector based on its spectral histogram. So, with SIM each hyperspectral image pixel vector can improve in material detection, discrimination, classification and identification. Because SIM is a statistical measure, it can generate higher order statistics that can further be used to characterise spectral variability, such as variance, skewness and kurtosis. This advantage cannot be achieved by any deterministic measure, such as Euclidean distance (Schowengerdt, 1997).

The Spectral Information Divergence (SID) measures spectral similarity. It originates from the concept of divergence in information theory and measures the discrepancy of probabilistic behaviours between the spectral signatures of two pixel vectors. In other words, the spectral similarity between two pixel vectors is measured by SID based on the discrepancy between their corresponding spectral signature-derived probability distributions. The idea of using divergence is not new and has also been found in pattern recognition and band selection, such as Jeffries-Matusita measure. But what is new for SID is that it is designed from SIM for spectral similarity. Essentially, SID measures the distance between the probability distributions produced by the spectral signatures of two pixel vectors and is quite effective in capturing spectral variability (Chang, 2003).

Band selection for remotely sensed image data is an effective means to mitigate the problem of dimensionality. Taking advantage of spectral correlation to achieve optimal band selection is one of the unique features in multispectral/hyperspectral images. Many criteria have been proposed for band selection in the past to find bands that are crucial and significant in terms of information conservation. For example, distance measures, information theoretic approaches (divergence, transformed divergence, mutual information) and eigen-analysis (PCA) have been applied to multispectral images for optimal band selection. In particular, the use of the divergence measure for band selection has received considerable interest in multispectral imagery.

The Signature-to-Signature Spectral Correlation (SSSC) is a band selection method for hyperspectral images, which uses a library of the spectral signatures of the objects subject to classification, as criteria (Kolokoussis, 2008). After having calculated mean reflectance values for all pixels and objects, a histogram is plotted of bandwidth against % reflectance (x1000) for each object, in order to define the behaviour of the object spectral signatures per band. Bands are selected based on the assumption that the most valuable, in terms of information content, bands are the ones where object spectral signatures are most divergent and are essentially those where object reflectance allows for the highest degree of material detection, discrimination, classification and identification, similar to SIM. A correlation function between the reflectance of each object in comparison with all other objects, for each band, is the criterion used to exclude bands. A correlation below a certain threshold (in this case 0.98) for at least one comparison of each object with all others provides us with a bandwidth of interest, according to the formula:

$$Correl(X,Y)=\frac{\sum_{j_{-3}}^{j_{+3}}(x_i-\overline{x_i})(y_i-\overline{y_i})}{\sqrt{\sum_{j-3}^{j_{+3}}(x_i-\overline{x_i})^2\sum_{j_{-3}}^{j_{+3}}(y_i-\overline{y_i})}}$$

Where x_i and y_i are values from two datasets corresponding to the % reflectance multiplied by 1000 (for storage reduction reasons) for object (or forest tree species) X and Y, while j is corresponding to position from a list of a discreet numbers of bandwidths in ascending order.

In this case, each time the correlation is calculated between 3 spectral bands above and 3 below a central bandwidth (total 7) for all bandwidths.

The bands that are selected at the end are the ones where at least two (2) of the correlations have given a value below 0.98.

The bands used in classifications can be found in the results section.

2.4 Processing – Object Based Image Analysis (OBIA)

Object – based image analysis (OBIA), a technique used to analyze digital imagery, was developed relatively recently compared to traditional pixel-based image analysis (Burnett & Blaschke, 2003). While pixel-based image analysis is based on the information in each pixel, object-based image analysis is based on information from a set of similar pixels called objects or image objects. More specifically, image objects are groups of pixels that are similar to one another based on a measure of spectral properties (i.e. color, size, shape and texture) as well as context from a neighborhood surrounding the pixels (Nearest Neighbour – NN feature space).

Classification was carried out using the eCognition software with standard nearest neighbour classifier. All projects were carried out using OBIA, initially with classification based solely on the spectral signature of tree species determined using the training areas provided by the TTA mask. After using accuracy statistics for selecting imagery giving better results, classification was also based on fuzzy-logic-based restrictions concerning the elevation, slope and aspect specifications for each tree species.

3. Results

eCognition Developer 8.64 software (formerly Definiens) of Trimble Germany GmbH (München, Germany) was specifically created as an instrument for OBIA and is used in all processes described below, unless otherwise stated. Classification was carried out using the standard nearest neighbour (NN) classifier and all projects included the three layers (elevation, slope and aspect) of the ASTER GDEM imagery.

For all (multiresolution) segmentations the bands of each image were taken into account, having been given equal weights (1), including the three GDEM layers (elevation, slope and aspect). For each (hierarchical) classification a Standard Nearest Neighbour Feature Space was generated based on the spectral signatures of each class as a result of taking into consideration all bands of the respective imagery (GDEM layers were not taken into account for the classifications). Simpson's biodiversity index was estimated on a different level (a level above) with greater area and was dealt with differently than all other classification processes, as we will see in the last section of this chapter.

For all classification results illustrated below, one should refer to the colour key of figure 21.

3.1 Object Based Image Analysis (OBIA) on Remote Sensing Multispectral and Hyperspectral Data

3.1.1 CASI 2m spatial resolution imagery

Figure 26, below illustrates the CASI imagery of 2 m spatial resolution, which includes all 72 bands. The ASTER Global Digital Elevation Model (ASTER GDEM) (three bands: elevation, slope and aspect) is also included in the project.

The colour composite used in all figures presenting CASI imagery is as follows:

- Red: band 27
- Green: band 14
- Blue: band 2 (see appendix III for bandwidths).

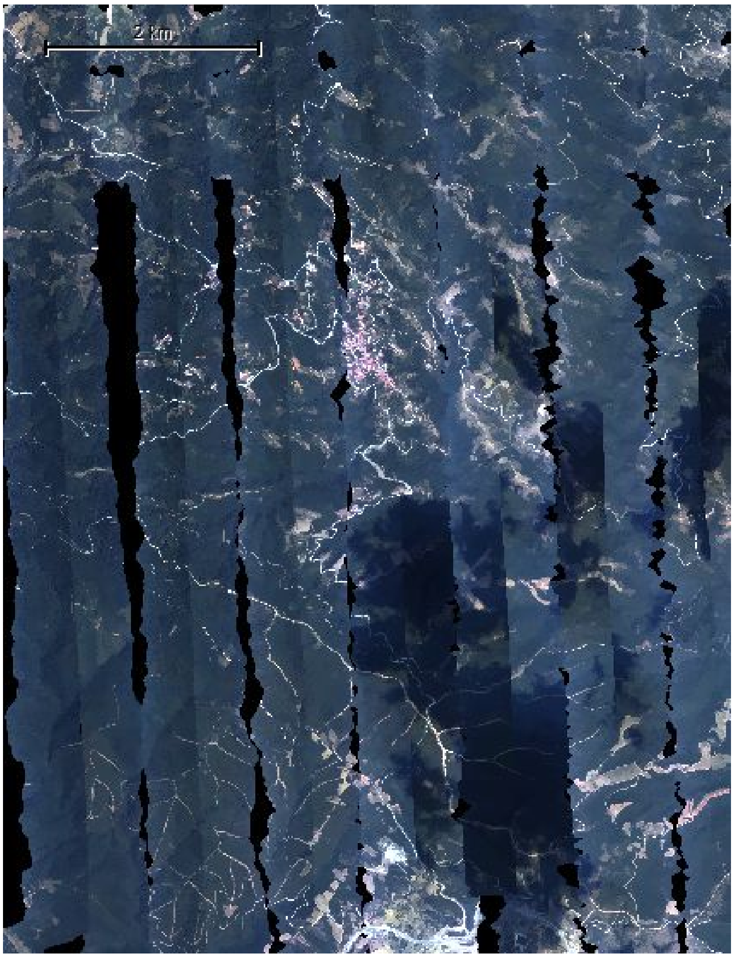

Figure 26: CASI 2m spatial resolution imagery (GDEM layers are also included, but not visible).

In figure 26, there are gaps every two strips of cover for the CASI image. This was possibly due to the relative position of the receiver to the aircraft or a problem in calibrating the instrument. A 40% overlap between strips of received reflectance was desired but not achieved. There was an overlap of approximately 80% every two strips and a 20% gap. This was compensated for by excluding these gaps from the TTA mask used for generating training areas and estimating the accuracy of the classification relative to the ground data.

The CASI image was segmented with multi-resolution segmentation. The level used for classification was created with scale factor 100, colour factor 0.8, compactness 0.5 (see figure 27.2).

It should be noted, that for all images a variety of segmentations was performed with different scale factors. In each case, the segmentation scale selected for further processing was the highest possible scale showing the least mixing of categories, based on the colour shade, representing vegetation (green or other for PCA and MNF). The choice was made based on visual evaluation and trial-and-error.

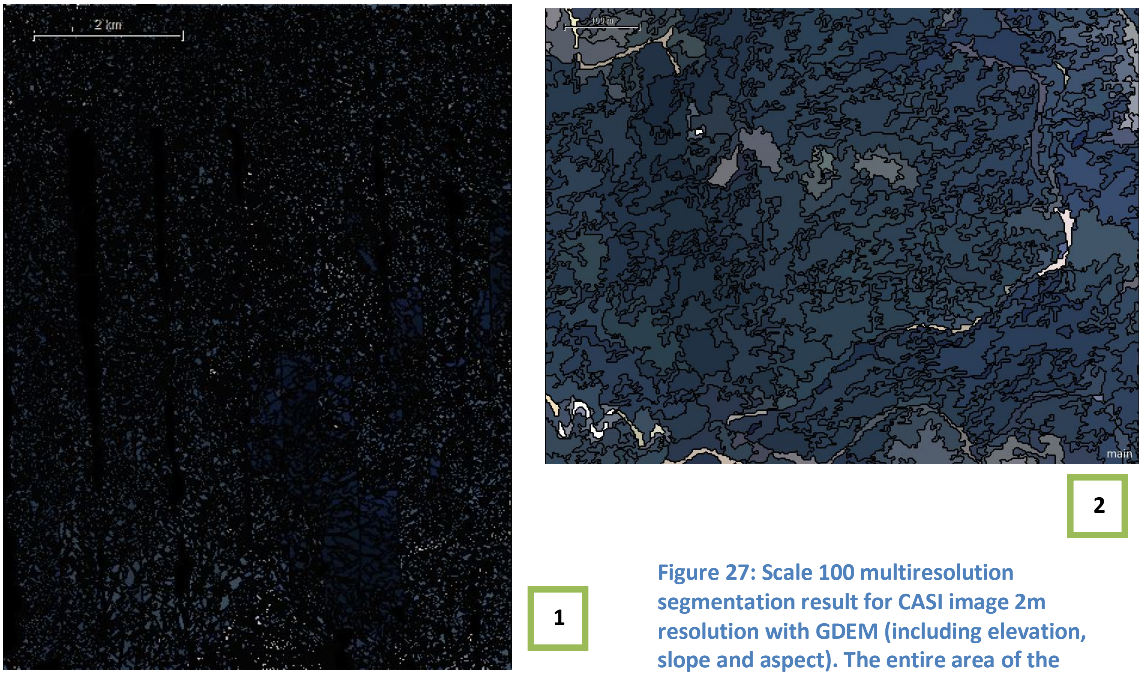

Figure 27: Scale 100 multiresolution segmentation result for CASI image 2m resolution with GDEM (including elevation, slope and aspect). The entire area of the image is illustrated in figure 1, while figure 2 depicts a zoomed on area and illustrating the way polygons were separated during segmentation.

Figures 28.1 and 28.2, below, illustrate the training areas, as taken using random samples from the TTA masks of figures 22 and 23 for groups A and B respectively, while figures 28.3 and 28.4 illustrate the classification result (class distribution based on spectral signatures).

For all classification results illustrated below, one should refer to the colour key of figure 21.

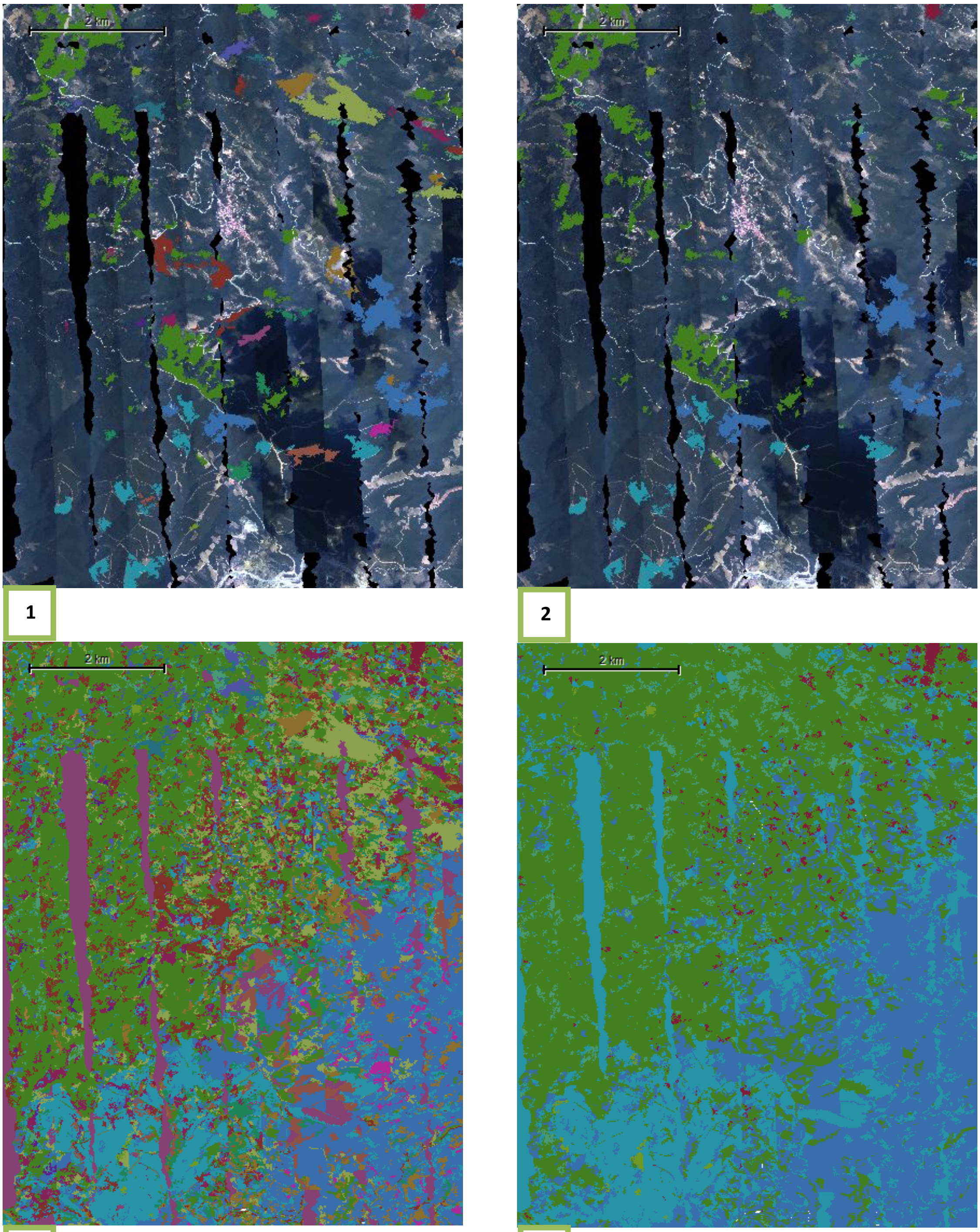

1

2

3

4

Figure 28: CASI 2 m spatial resolution training areas and classification result (refer to figure 21 for a colour key). Figures 27.1 and 27.2 show the training areas for classes of groups A and B respectively. Figures 27.3 and 27.4 illustrate the classification result for group A and B groups of classes respectively.

3.1.2 CASI 5 m spatial resolution imagery

The reduced spatial resolution of this image, provided that it is still quite high (5 m is marginally sufficient resolution for the identification of individual tree crowns of mature trees, provided that the image quality is satisfactory), relative to the satellite images, serves the purpose of reducing the size of the file under processing and thus the processing time.

The colour composite remains the same as in the previous CASI imagery of 2 m resolution.

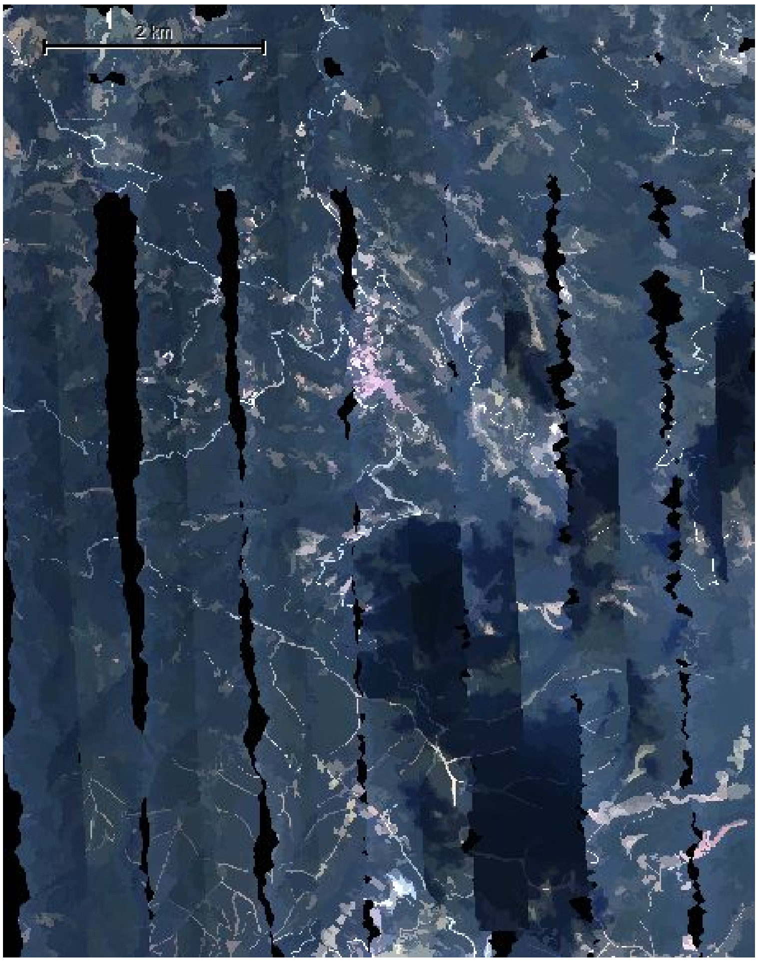

Figure 29: CASI 5m resolution. Colour composite: Red: band 27, Green: band 14, Blue: band 2.

The CASI image was segmented with multi-resolution segmentation. The level used for classification was created with scale factor 40, colour factor 0.8, compactness 0.5.

1

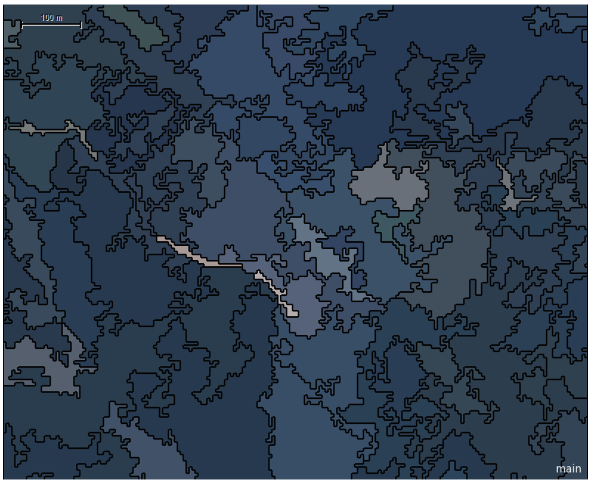

2

Figure 30: Scale 100 multiresolution segmentation result for CASI image 5m resolution with GDEM (including elevation, slope and aspect). The entire area of the image is illustrated in figure 1, while figure 2 depicts a zoomed on area and illustrates the way polygons were separated during segmentation.

Figures 31.1 and 31.2, below, illustrate the training areas, as taken using random samples from the TTA masks of figures 22 and 23 for groups A and B respectively, while figures 31.3 and 31.4 illustrate the classification result (class distribution based on spectral signatures).

For all classification results illustrated below, one should refer to the colour key of figure 21.

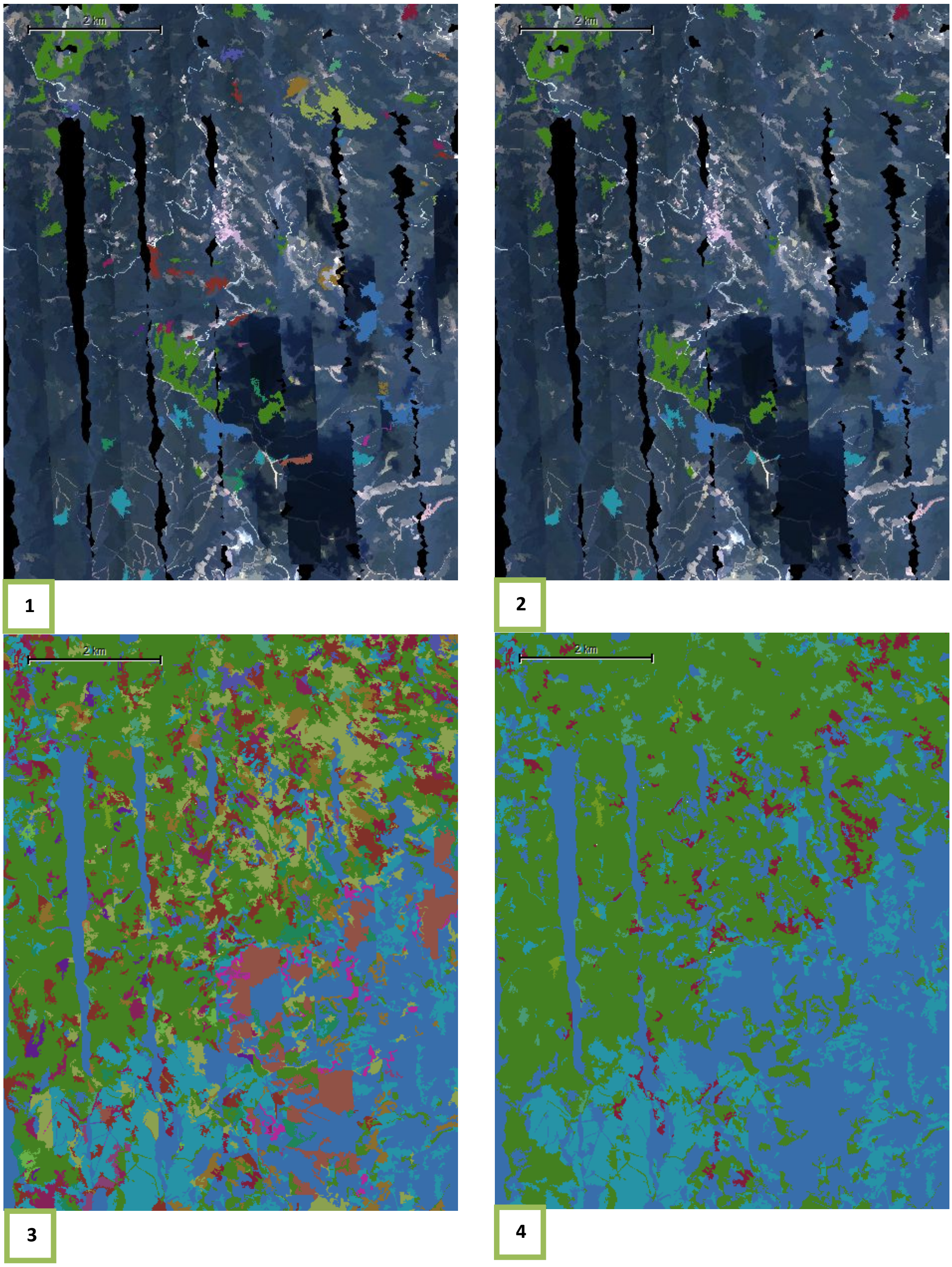

Figure 31: CASI 5 m spatial resolution training areas and classification results. Training areas (figures 1 and 3) and classification result (figures 3 and 4) for group A (figures 1 and 3) and B (figures 2 and 4) classes respectively.

3.1.3 CASI 2m spatial resolution atmospherically corrected (ATM) imagery

The CASI image was segmented with multi-resolution segmentation. The level used for classification was created with scale factor 100, colour factor 0.8 and compactness 0.5 (see figure 32.2).

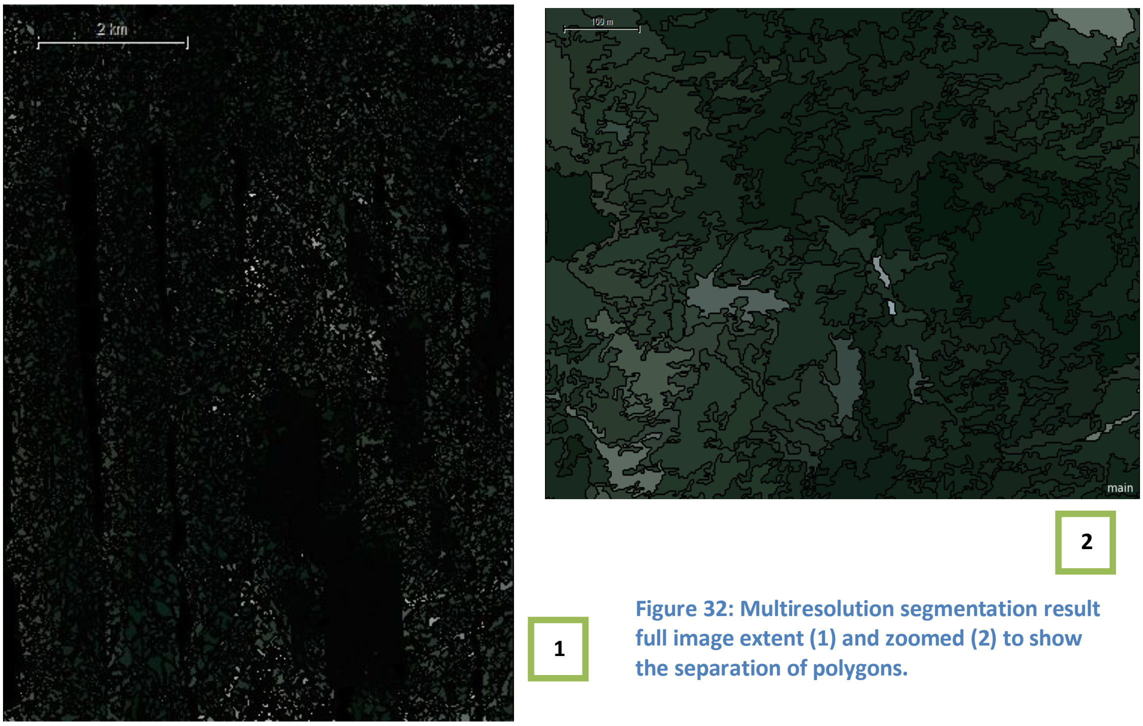

Figure 32: Multiresolution segmentation result full image extent (1) and zoomed (2) to show the separation of polygons.

Figures 33.1 and 33.2, below, illustrate the training areas, as taken using random samples from the TTA masks of figures 22 and 23 for groups A and B respectively, while figures 33.3 and 33.4 illustrate the classification result (class distribution based on spectral signatures).

For all classification results illustrated below, one should refer to the colour key of figure 21.

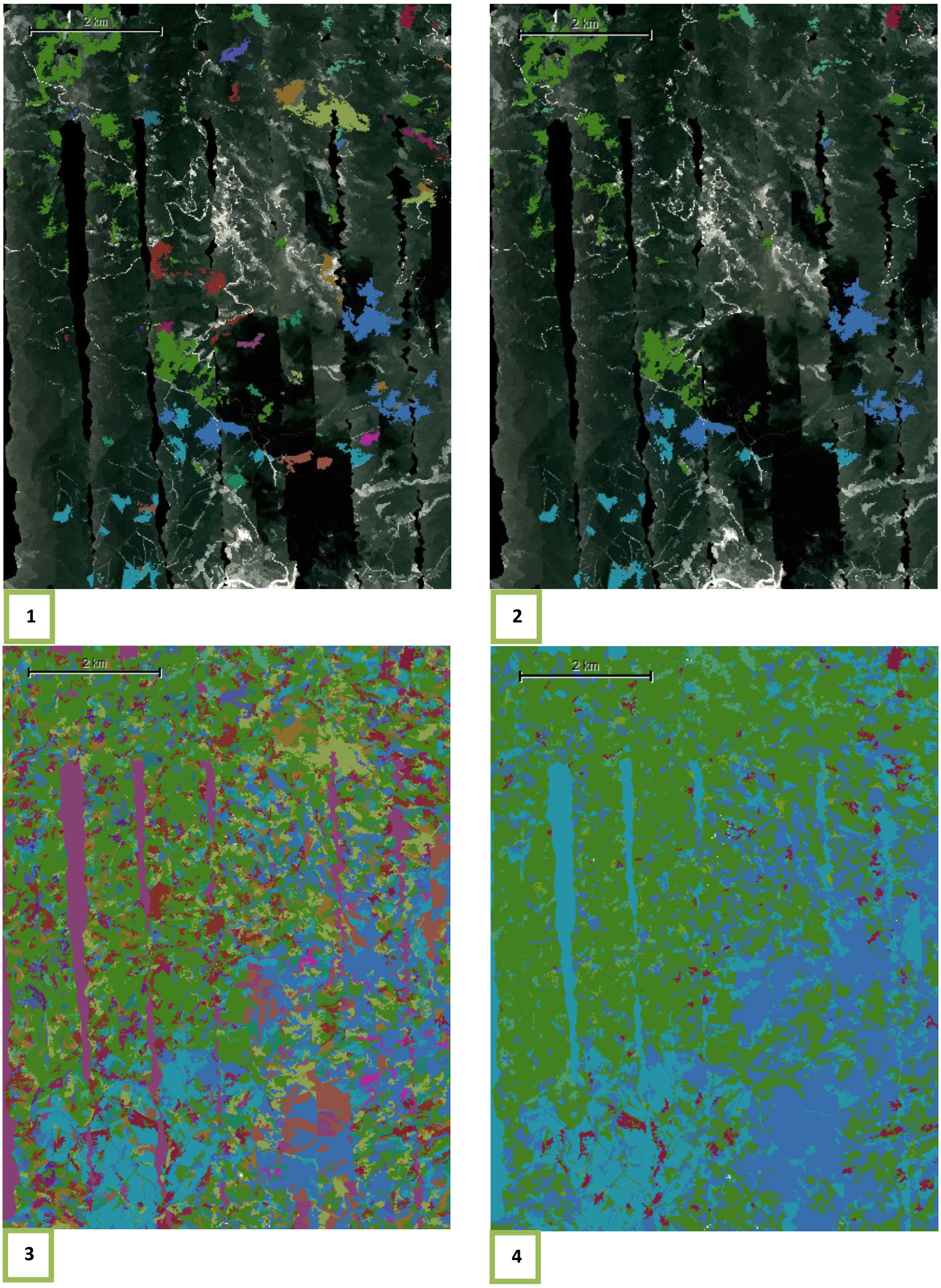

Figure 33: Atmospherically corrected (ATM) CASI 2 m spatial resolution training areas and classification result. Training areas (figures 1 and 3) and classification result (figures 3 and 4) for group A (figures 1 and 3) and B (figures 2 and 4) classes respectively.

3.1.4 Classification accuracies for CASI imagery

The accuracy of the classification result was compared to the ground data (as depicted in figures 22 and 23) for group A and group B classes. The accuracy is much better for group B classes, containing less and non-mixed classes. This conclusion could be anticipated, as the spectral signature of classes containing various tree species is expected to be less distinct than that of tree species with one particular species of tree and thus a specific and distinct chemical composition. It also becomes evident from the table below that the atmospheric correction for the CASI imagery did not improve the quality of our data, since greater accuracies were achieved for the non-atmospherically corrected imagery. In a study by Stavrakoudis *et al.* (2014) in Taxiarchis forest, the astmospheric correction performed on CASI also gave reduced classification accuracy results.

All bands	**CASI 2m**		**CASI 5m**		**CASI-ATM 2m**	
	Group A	Group B	Group A	Group B	Group A	Group B
Overall Accuracy	0.45	0.73	0.39	0.68	0.38	0.65
KIA	0.35	0.59	0.27	0.51	0.26	0.48

Table 5: Accuracies for classification results of projects with all available bands used relative to the ground data generated TTA mask

3.1.5 Landsat imagery

The colour composite used in all figures presenting the Landsat 8 OLI image is as follows:

- Red: band 4
- Green: band 3
- Blue: band 2 (see appendix I for a full list of Landsat 8 OLI spectral bands.)

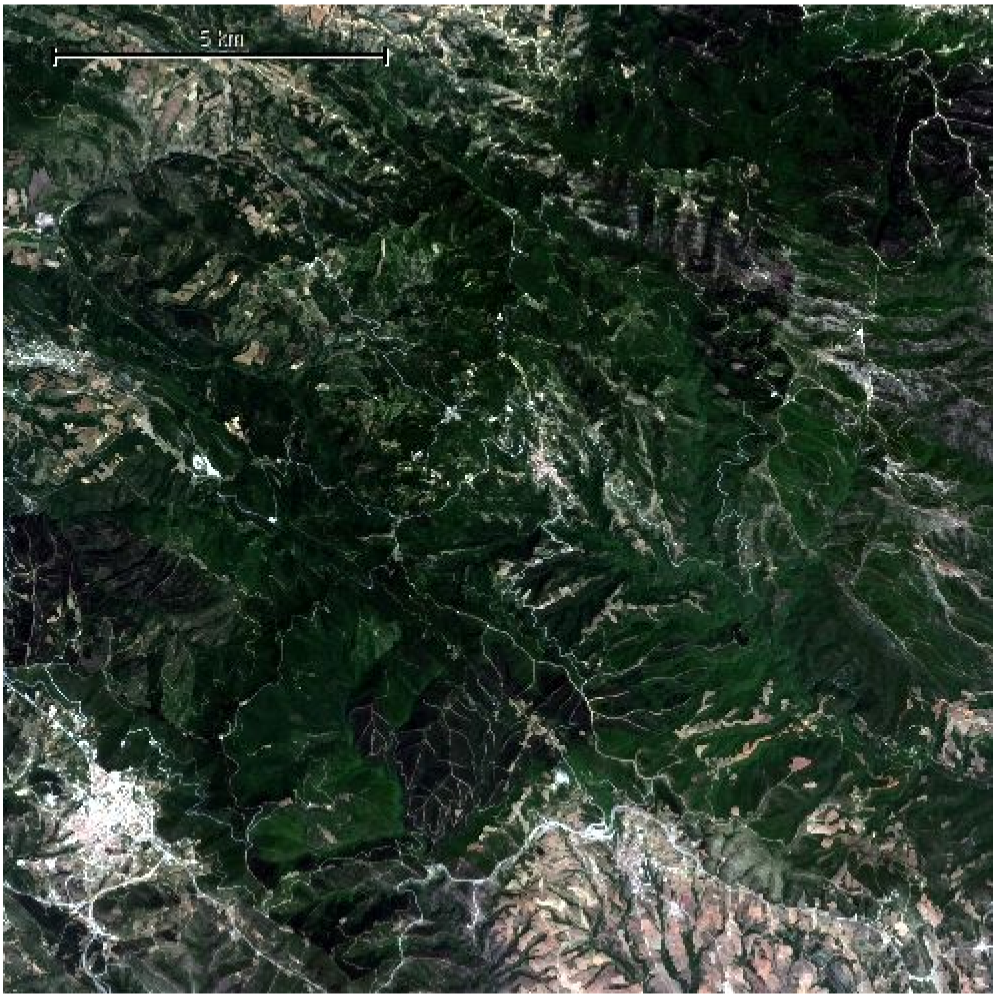

Figure 34: Landsat image with colour composite representing true colours.

The Landsat image was segmented with multi-resolution segmentation. The level used for classification was created with scale factor 20, colour factor 0.8 and compactness 0.5 (see figure 35).

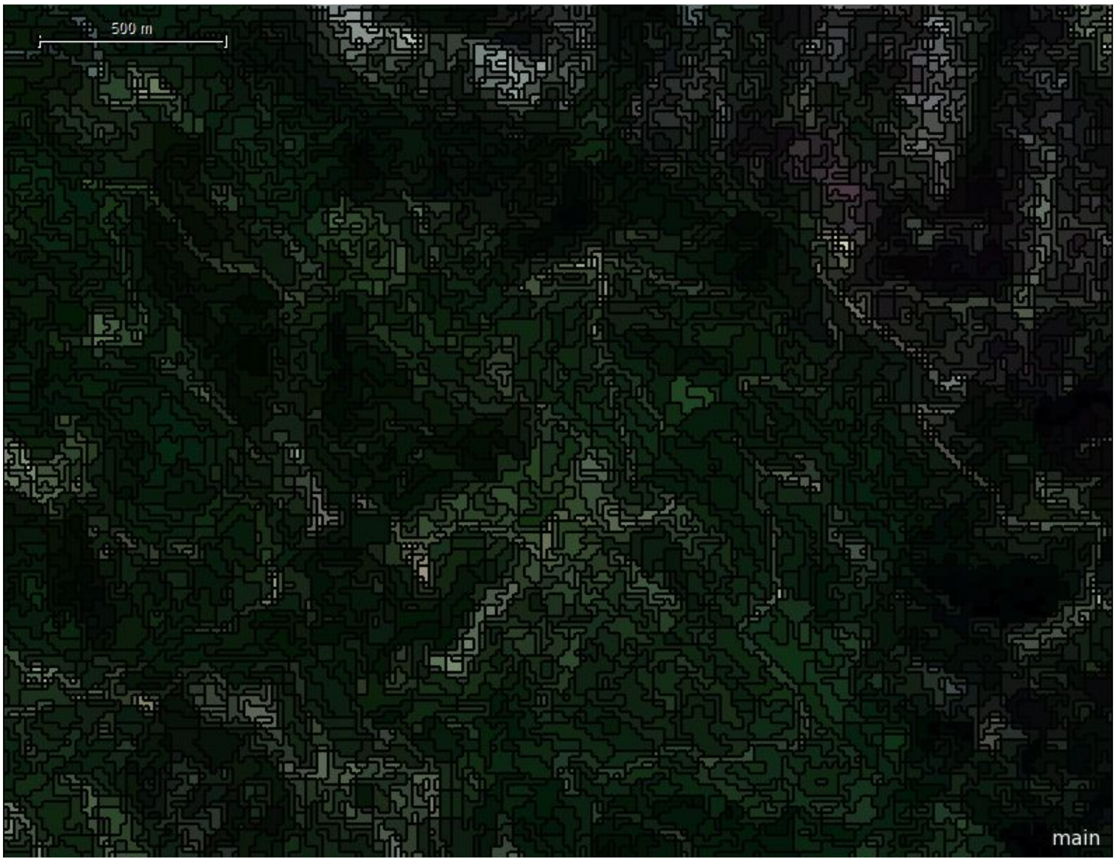

Figure 35: Multiresolution segmentation for the Landsat image.

Figures 36.1 and 36.2, below, illustrate the training areas, as taken using random sampling from the TTA masks of figures 22 and 23 for groups A and B respectively, while figures 36.3 and 36.4 illustrate the classification result (class distribution based on spectral signatures).

For all classification results illustrated below, one should refer to the colour key of figure 21.

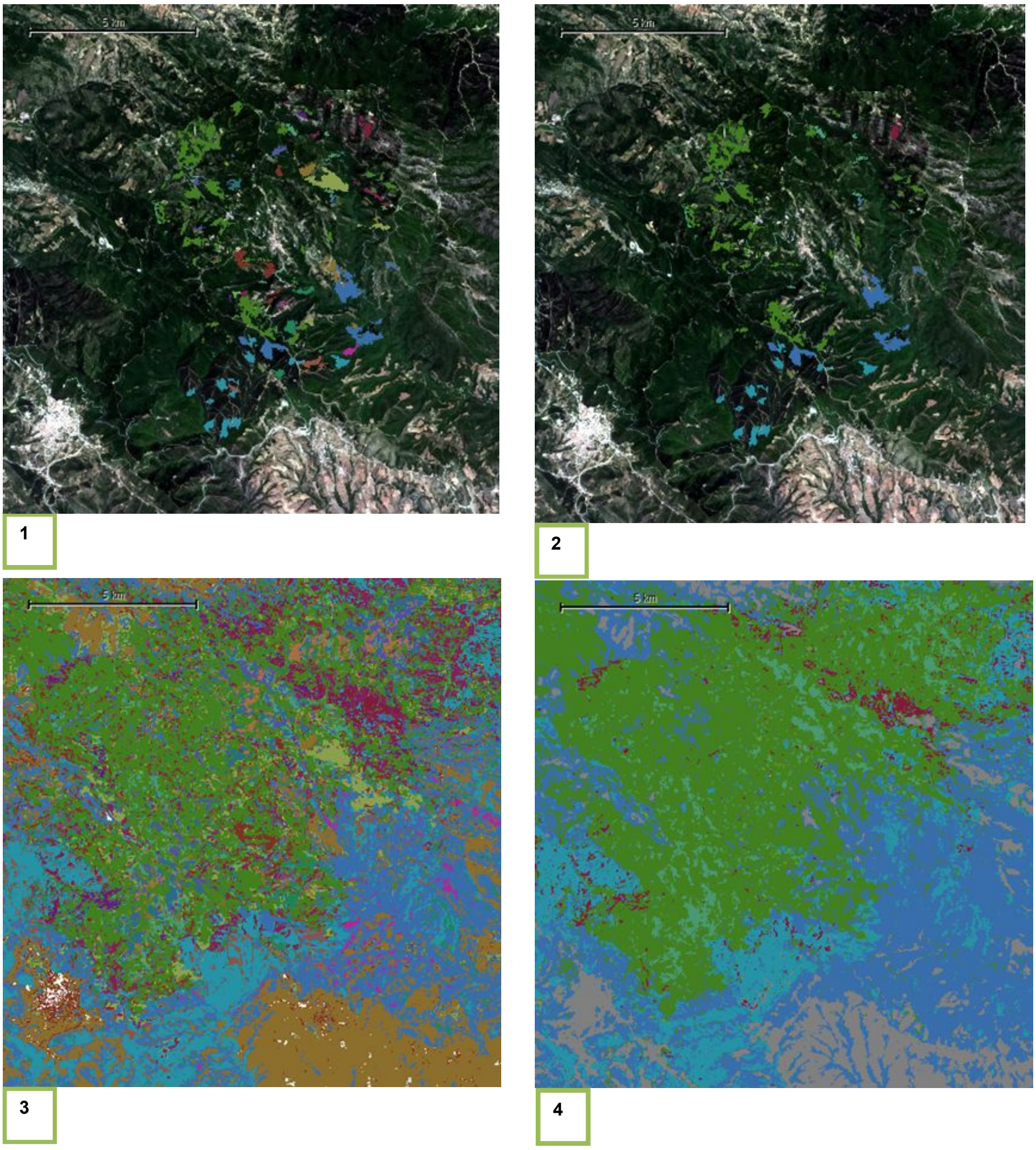

Figure 36: Landsat training areas and classification result. Training areas (figures 1 and 3) and classification result (figures 3 and 4) for group A (figures 1 and 3) and B (figures 2 and 4) classes respectively.

3.1.6 GeoEye imagery

The colour composite in all figures presenting the GeoEye imagery is as follows:

Blue: 450 - 510 nm
Green: 510 - 580 nm
Red: 655 - 690 nm

The resulting colour composite is illustrated in figure 37.1, below.

The GeoEye image was segmented with multi-resolution segmentation. The level used for classification was created with scale factor 50, colour factor 0.8, compactness 0.5 (see figure 37.2 for the segmentation).

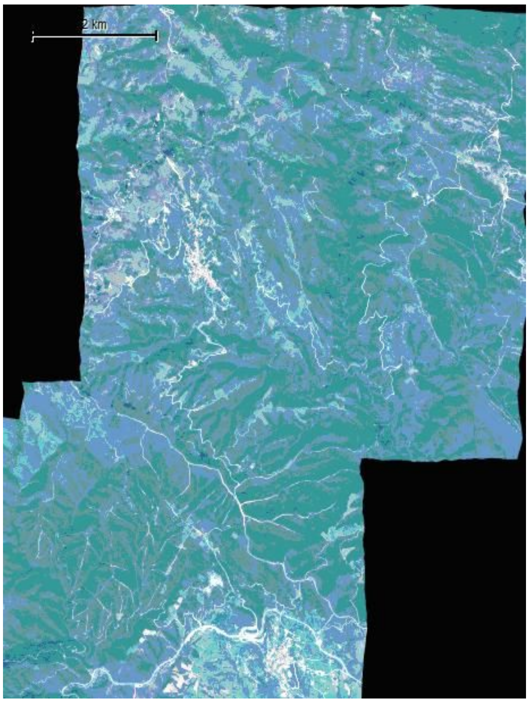

1

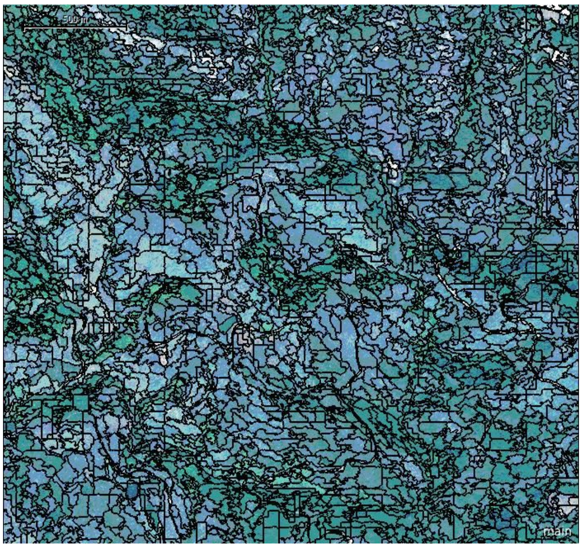

2

Figure 37: Geoeye image (1) and multiresolution segmentation zoomed (2) to show the separation of polygons.

Figures 38.1 and 38.2, below, illustrate the training areas, as taken using random samples from the TTA masks of figures 22 and 23 for groups A and B respectively, while figures 38.3 and 38.4 illustrate the classification result (class distribution based on spectral signatures).

For all classification results illustrated below, one should refer to the colour key of figure 21.

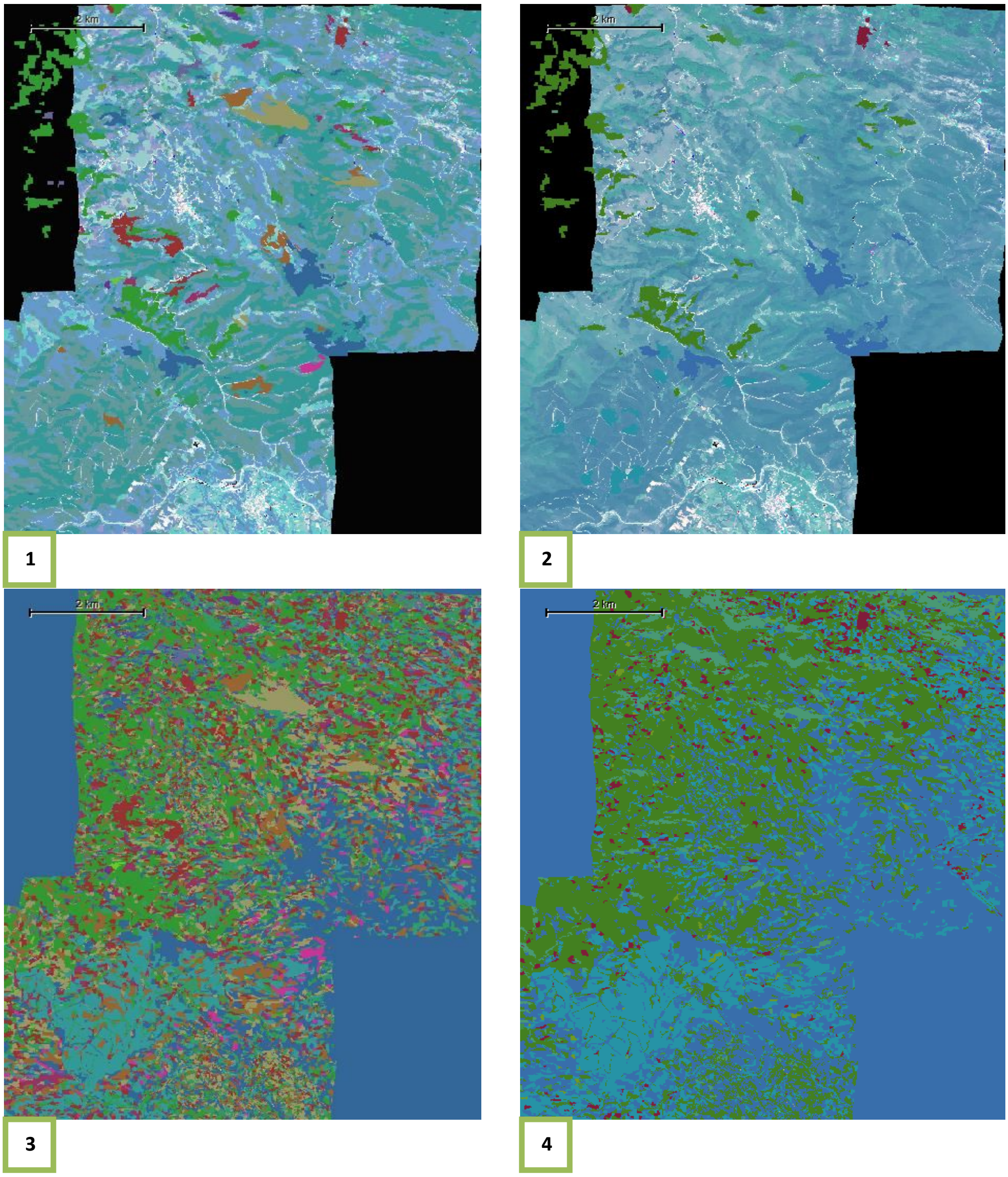

Figure 38: GeoEye samples and classification result. Training areas (figures 1 and 3) and classification result (figures 3 and 4) for group A (figures 1 and 3) and B (figures 2 and 4) classes respectively.

3.1.7 Hyperion imagery

The colour composite, presenting the imagery in true colours (see figure 39.1), is as follows:

- Red: 630 – 680 nm
- Green: 520 – 590 nm
- Blue: 450 – 515 nm

The Hyperion image was segmented with multi-resolution segmentation. The level used for classification was created with scale factor 10, colour factor 0.8, compactness 0.5 (see figure 39.2).

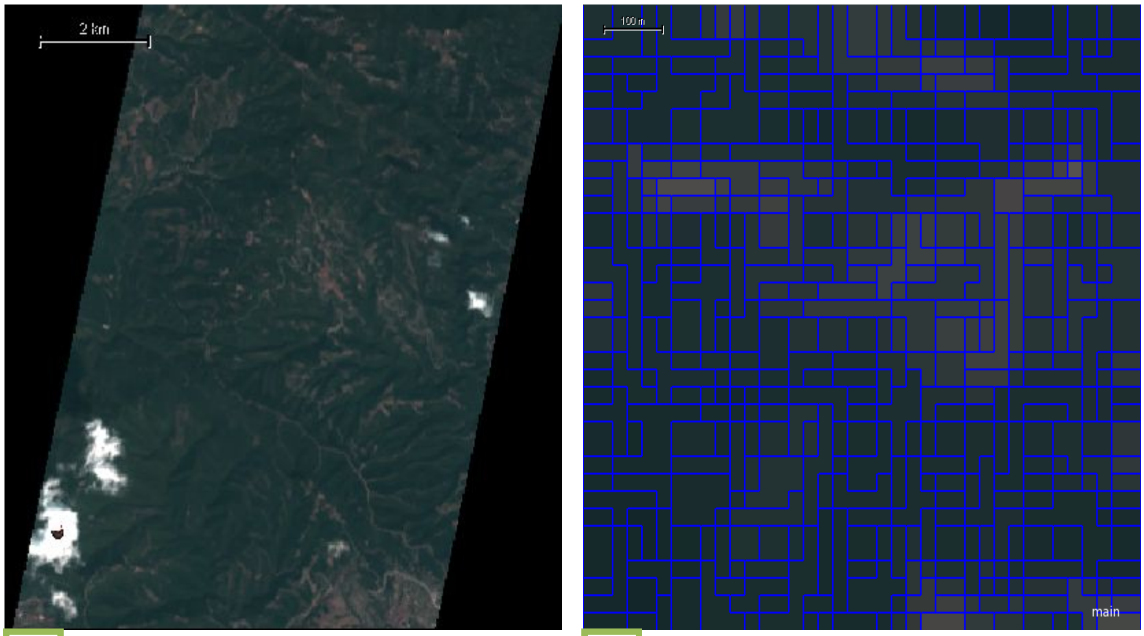

1 2

Figure 39: Hyperion image (1) and multiresolution segmentation zoomed (2) to show the separation of polygons.

Figures 40.1 and 40.2, below, illustrate the training areas, as taken using random samples from the TTA masks of figures 22 and 23 for groups A and B respectively, while figures 40.3 and 40.4 illustrate the classification result (class distribution based on spectral signatures).

For all classification results illustrated below, one should refer to the colour key of figure 21.

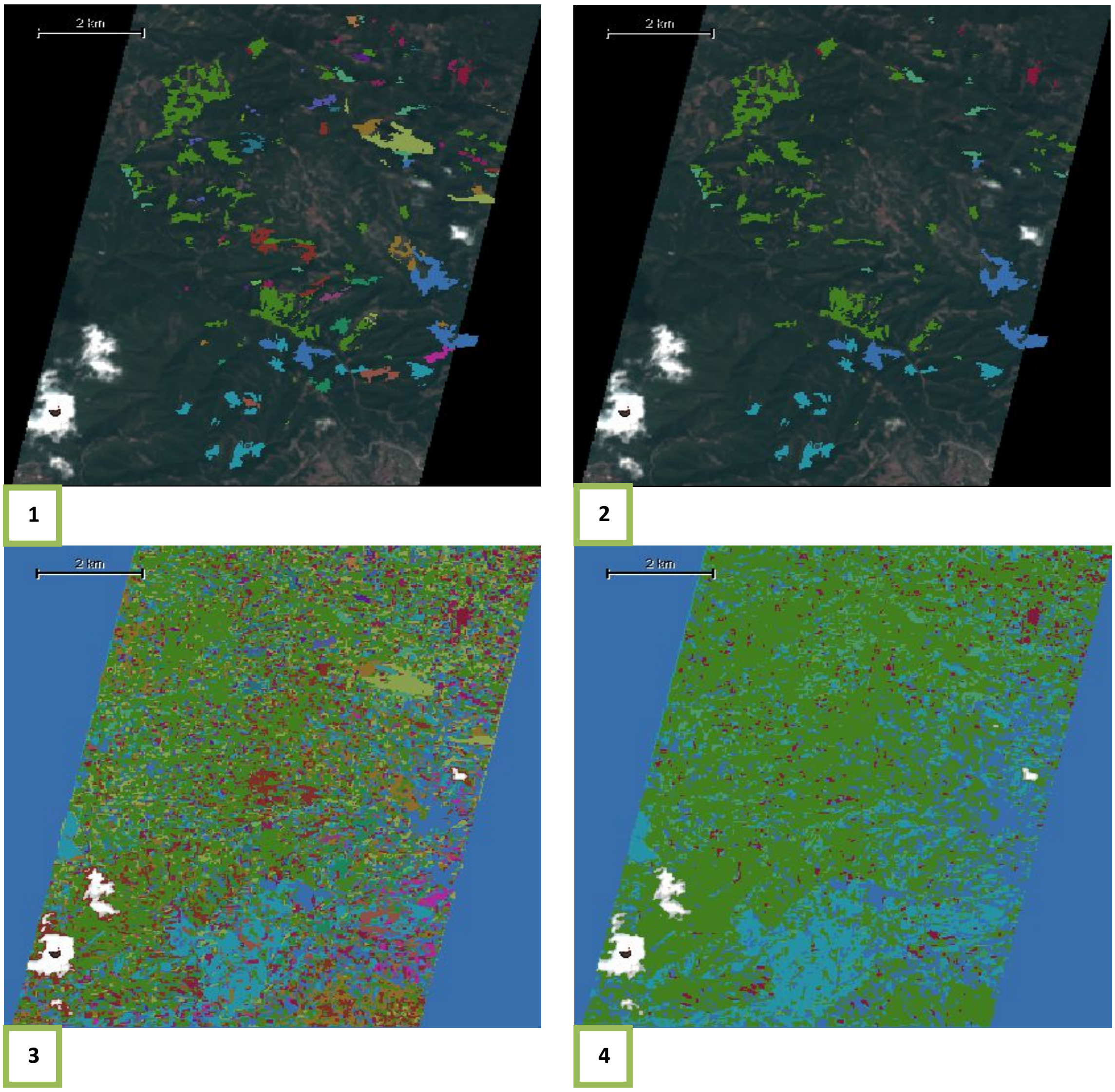

Figure 40: Hyperion training areas and classification result areas (figures 1 and 3) and classification result (figures 3 and 4) for group A (figures 1 and 3) and B (figures 2 and 4) classes respectively.

3.1.8 Classification accuracies for satellite imagery

The highest accuracy achieved for the satellite images is for Landsat group B classes. In fact, it is the highest accuracy achieved (before physiographic corrections), despite the spatial resolution being 15 m (after being combined with the panchromatic bands). The quality of the Landsat image is better than the GeoEye and Hyperion images, both with a greater number of bands and thus containing more information. This could be due to a lack in radiometrically induced noise or atmospheric factors. Thus, on a preliminary level, we can conclude that noise removal constitutes the main obstacle for mapping vegetation using hyperspectral and multispectral imaging.

	LANDSAT		**GEOEYE**		**HYPERION**	
All bands	Group A	Group B	Group A	Group B	Group A	Group B
Overall Accuracy	0.49	0.77	0.39	0.66	0.39	0.66
KIA	0.39	0.65	0.30	0.51	0.28	0.48

Table 6: Accuracies for classification results of satellite data (GeoEye, Hyperion and Landsat) projects relative to the ground data generated TTA mask

3.2 OBIA on Principal Component Analysis (PCA) transformed Hyperspectral Imagery

3.2.1 PCA transformed CASI 5m spatial resolution imagery

The CASI 5m spatial resolution image was transformed using Principal Component Analysis (PCA), thus extracting five (5) bands with the least noise and most information, according to the PCA methodology, described in section 2.3.4.1, whilst reducing processing time.

The CASI image was segmented with multi-resolution segmentation. The level used for classification was created with scale factor 40, colour factor 0.8, compactness 0.5 (see figure 41.2).

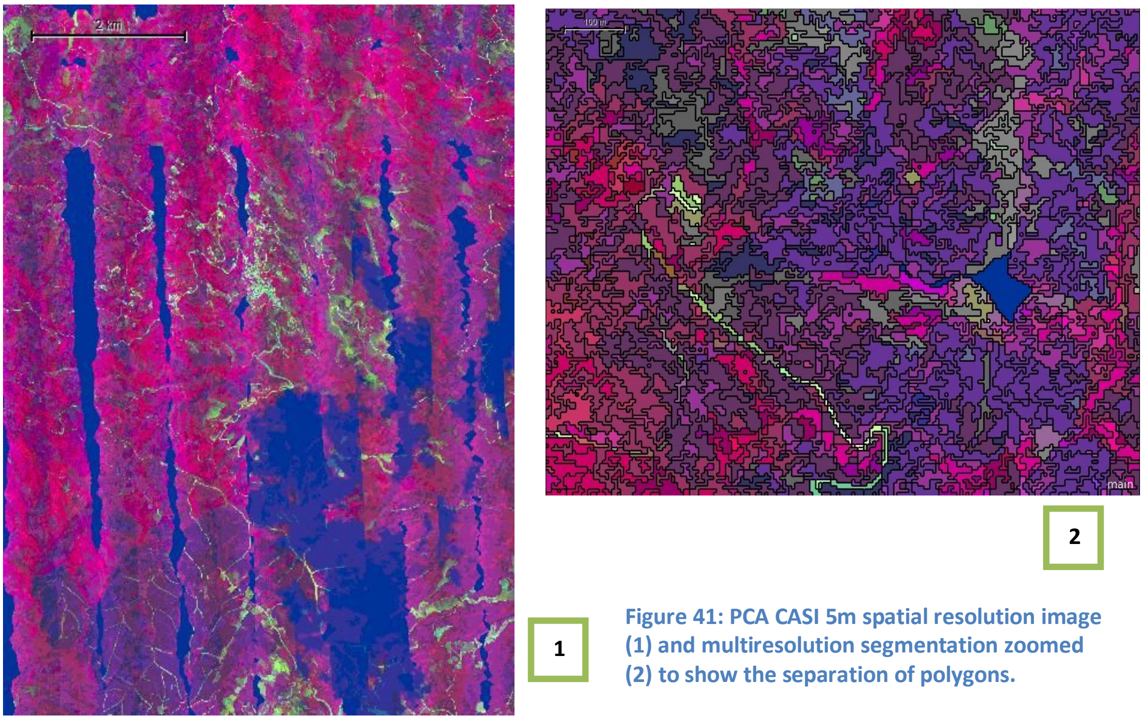

Figure 41: PCA CASI 5m spatial resolution image (1) and multiresolution segmentation zoomed (2) to show the separation of polygons.

Figures 42.1 and 42.2 illustrate the classification result (class distribution based on spectral signatures), based on the training areas taken using random samples from the TTA masks of figures 22 and 23 for groups A and B respectively (see figures 30.1 and 30.2 for a training area illustration).

For all classification results illustrated below, one should refer to the colour key of figure 21.

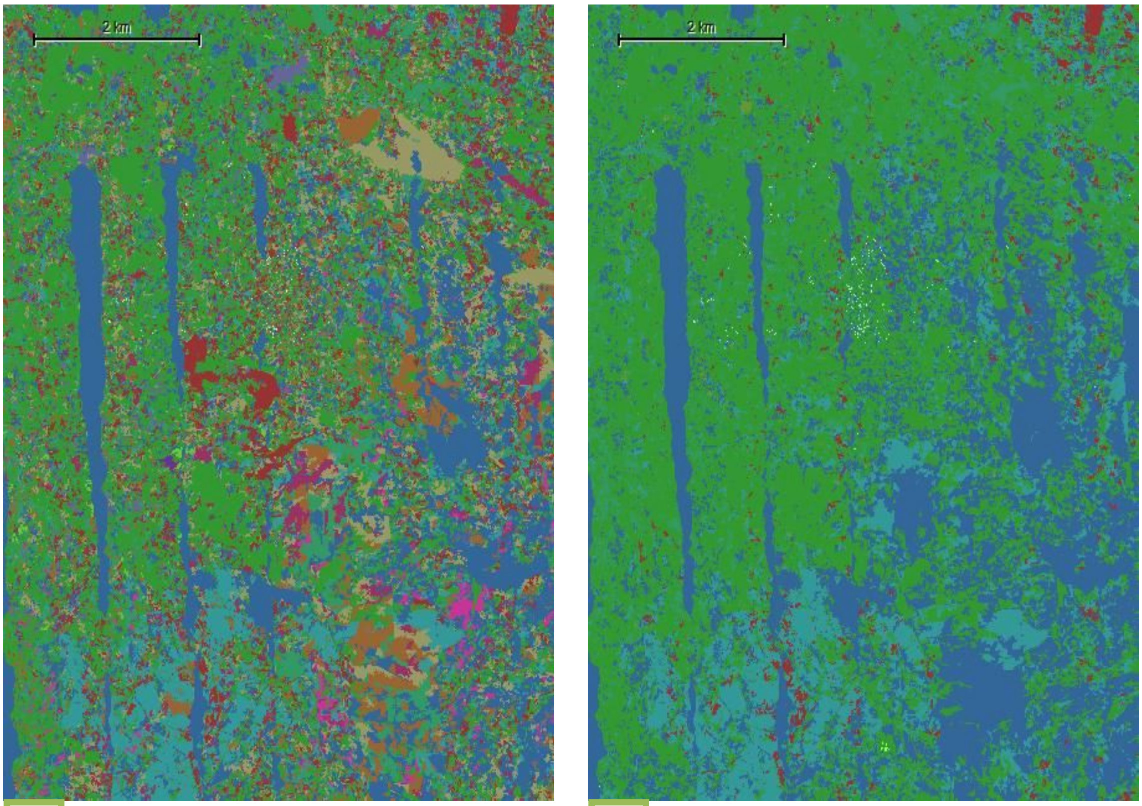

1

2

Figure 42: PCA CASI 5 m spatial resolution imagery classification result (figures 1 and 2) for group A (figure 1) and B (figure 2) classes respectively.

3.2.2 PCA transformed CASI 2 m and 5 m spatial resolution atmospherically corrected (ATM) imagery

The PCA transformed CASI image (5 PCAs extracted and used with equal weights (1) as previously for segmentation and classification) was segmented with multi-resolution segmentation. The level used for classification was created with scale factor 100 for the 2 m and 40 for the 5 m spatial resolution image, colour factor 0.8, compactness 0.5 (see figure 43.2 and 43.3) (for all spatial resolutions).

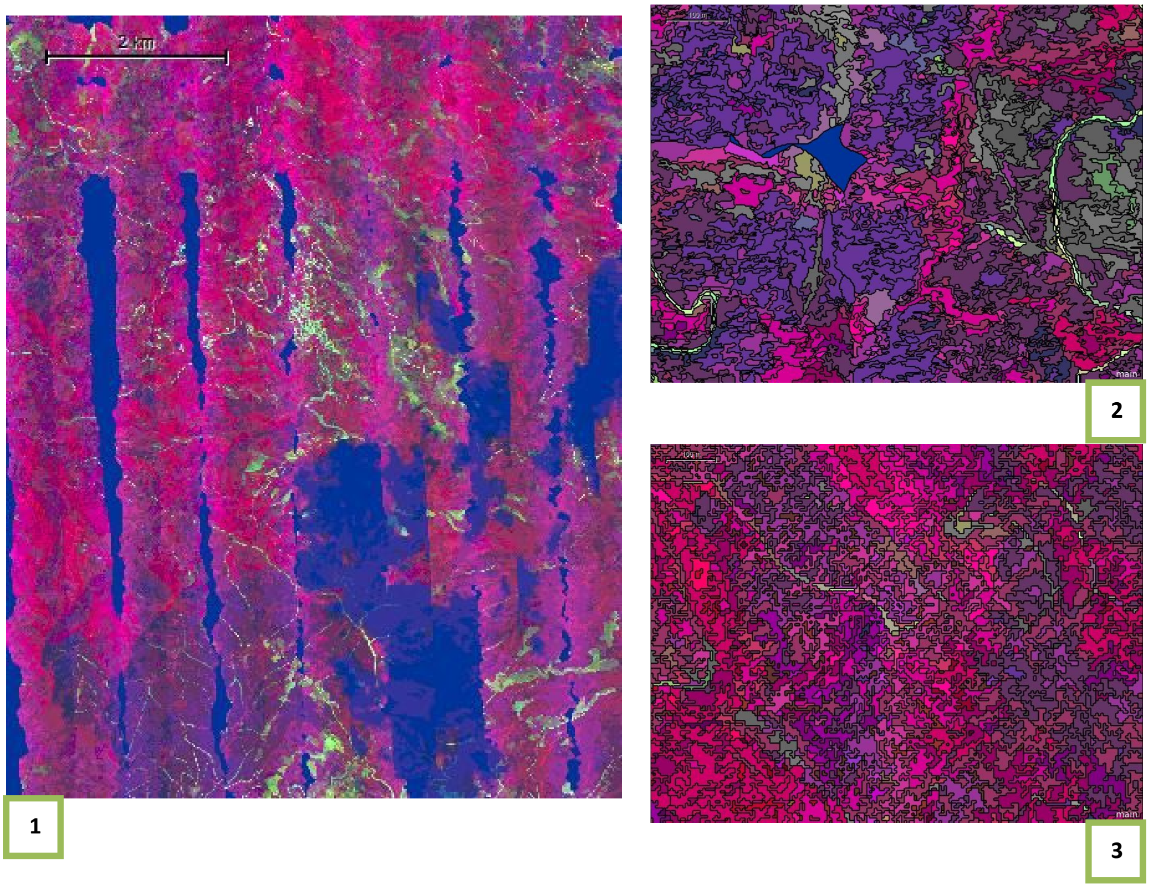

Figure 43: PCA transformed atmospherically corrected (ATM) CASI 2m (see figure 1) (for segmentation see figure 2) and 5m (for segmentation see figure 3) spatial resolution imagery.

Figures 44.1 and 44.2, below, illustrate the training areas, as taken using random samples from the TTA masks of figures 22 and 23 for groups A and B respectively, while figures 44.3 and 44.4 illustrate the classification result (class distribution based on spectral signatures).

For all classification results illustrated below, one should refer to the colour key of figure 21.

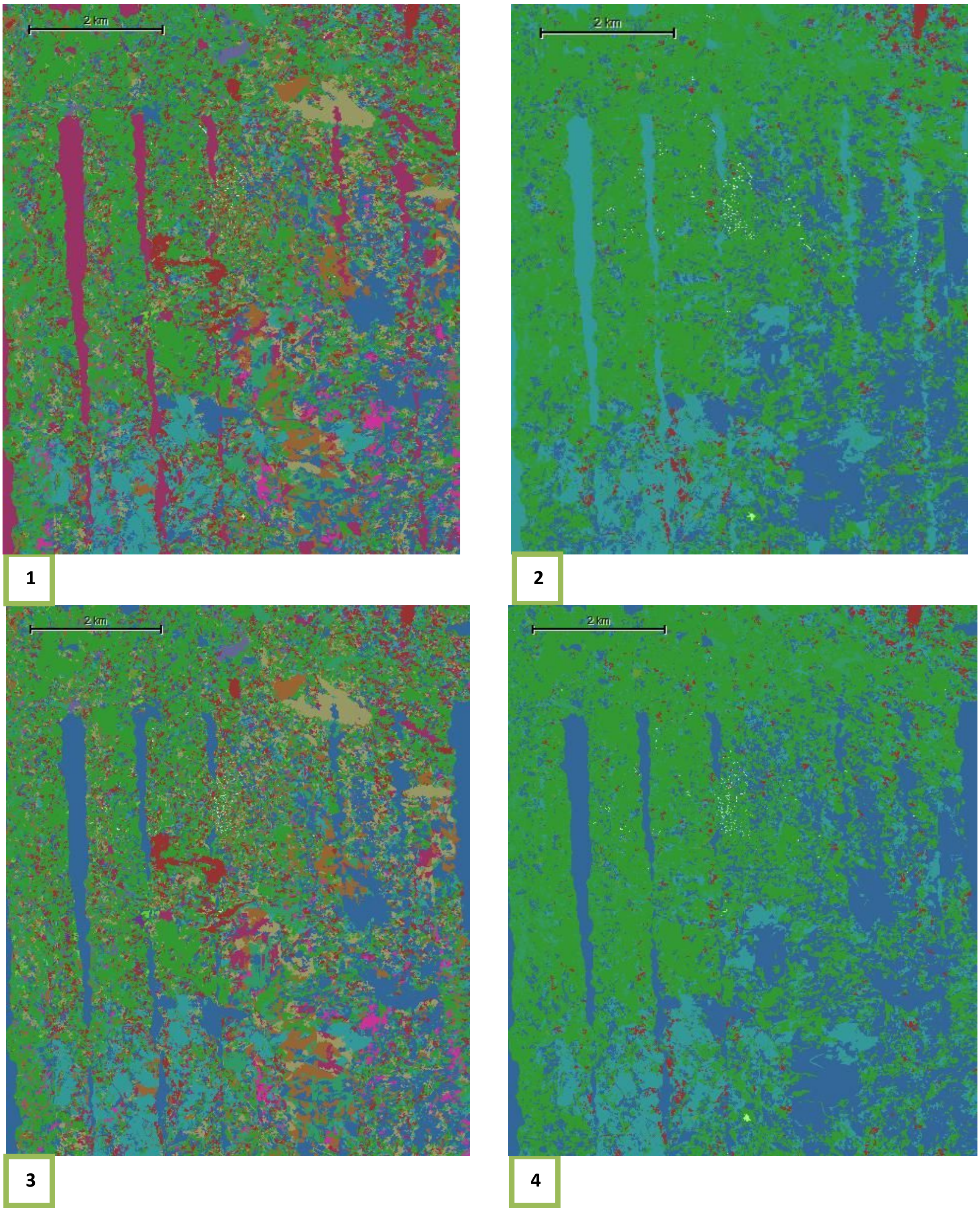

Figure 44: PCA transformed CASI ATM 2m and 5m spatial resolution classification results (for 2m spatial resolution classification result see figures 1 and 2, and for 5m spatial resolution see figures 3 and 4) for group A (figures 1 and 3) and B (figures 2 and 4) classes respectively.

3.2.3 PCA transformed Hyperion imagery

The PCA transformed Hyperion image (see figure 45.1) was segmented with multi-resolution segmentation. Six (6) PCAs were extracted and were given equal weights (1) at the segmentation and classification processes. The level used for classification was created with scale factor 50, colour factor 0.8, compactness 0.5 (see figure 45.2 and 45.3).

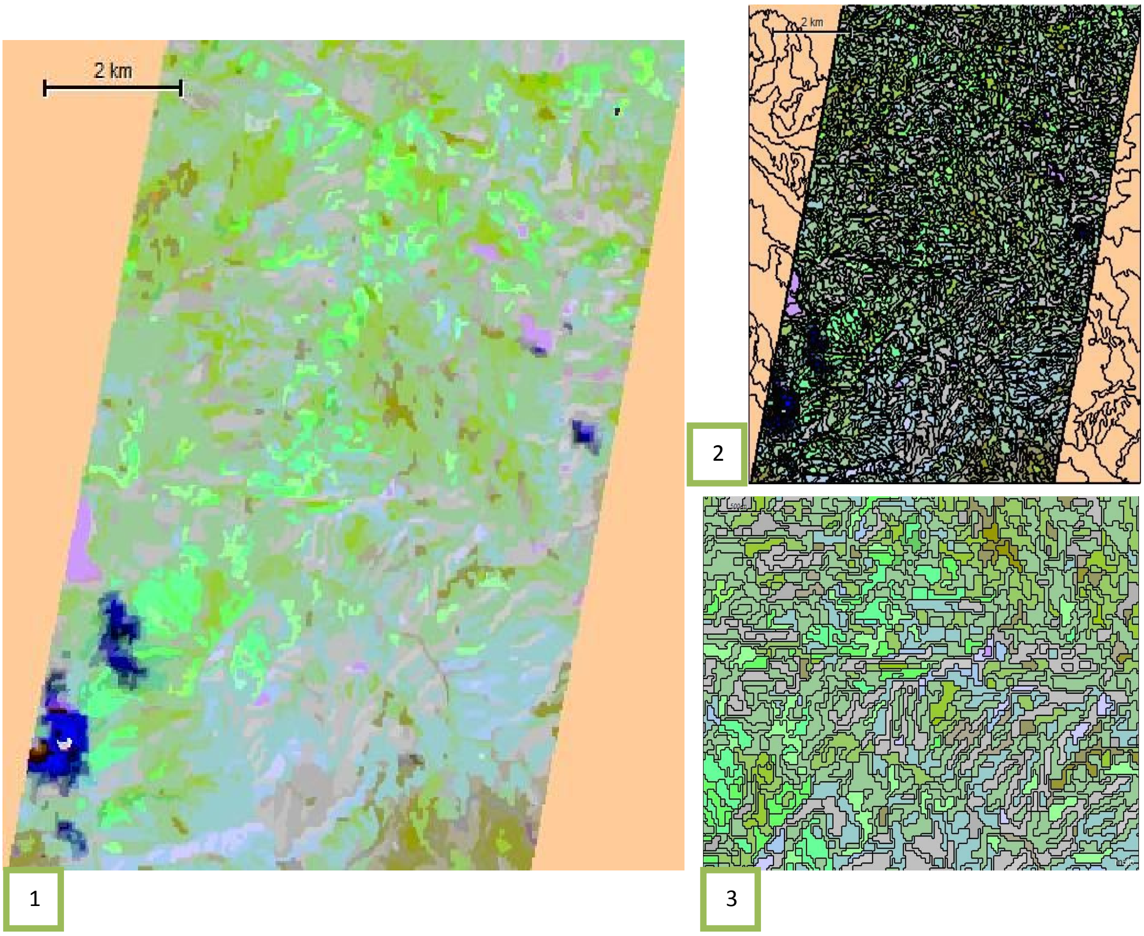

Figure 45: PCA transformed Hyperion image (see figure 1), segmentation (see figure 2) and zoomed in segmentation (see figure 3).

Figures 46.1 and 46.2, below, illustrate the classification result (class distribution based on spectral signatures), as taken using random samples from the TTA masks of figures 22 and 23 for groups A and B respectively.

For all classification results illustrated below, one should refer to the colour key of figure 21.

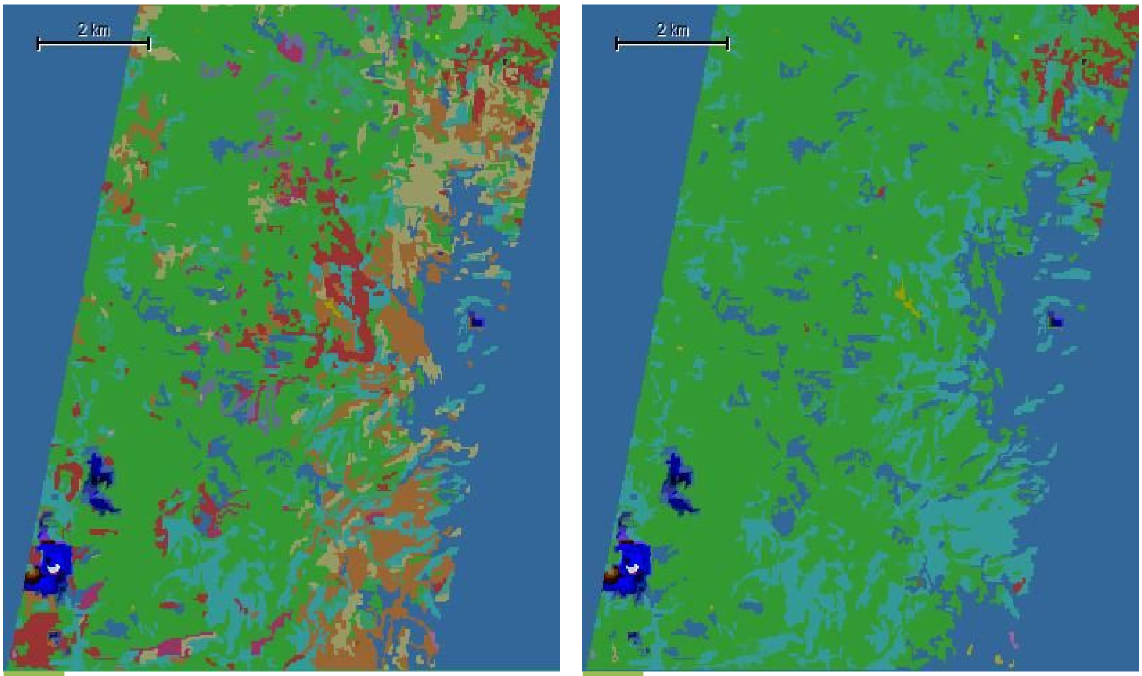

1

2

Figure 46: PCA transformed Hyperion imagery classification results for group A (see figure 1) and B (see figure 2) classes respectively.

3.2.4 Classification accuracies for PCA transformed hyperspectral imagery

All hyperspectral images transformed using the PCA methodology gave similar accuracies, with the atmospherically corrected CASI image of 2m spatial resolution giving a slightly better result. Overall, comparing the classification accuracies for all bands (tables 4 and 5 for CASI and Hyperion imagery respectively) and PCA transformed images there is loss of information and accuracy observed (with the exception of the atmospherically corrected CASI of 5m spatial resolution).

PCA	**CASI 5m**		**CASI-ATM 2m**		**CASI-ATM 5m**		**HYPERION**	
	Group A	Group B	Group A	Group B	Group A	Group B	Group A	Group B
Overall Accuracy	0.38	0.65	0.41	0.66	0.41	0.65	0.39	0.64
KIA	0.27	0.48	0.31	0.49	0.30	0.47	0.27	0.44

Table 7: Accuracies for classification results of PCA projects relative to the ground data generated TTA mask

3.3 OBIA on Minimum Noise Fraction (MNF) transformed Hyperspectral Imagery

3.3.1 MNF transformed CASI 2m spatial resolution imagery

The CASI 2m spatial resolution imagery was transformed using Minimum Noise Fraction (MNF), thus extracting six (6) bands with the least noise and most information, according to the MNF methodology, described in section 2.3.4.2, whilst reducing processing time, as with the PCA transform.

The CASI image was segmented with multi-resolution segmentation. The level used for classification was created with scale factor 50, colour factor 0.8, compactness 0.5 (all six MNF bands were used with equal weights (1) during segmentation and classification) (see figures 47.2 and 47.3).

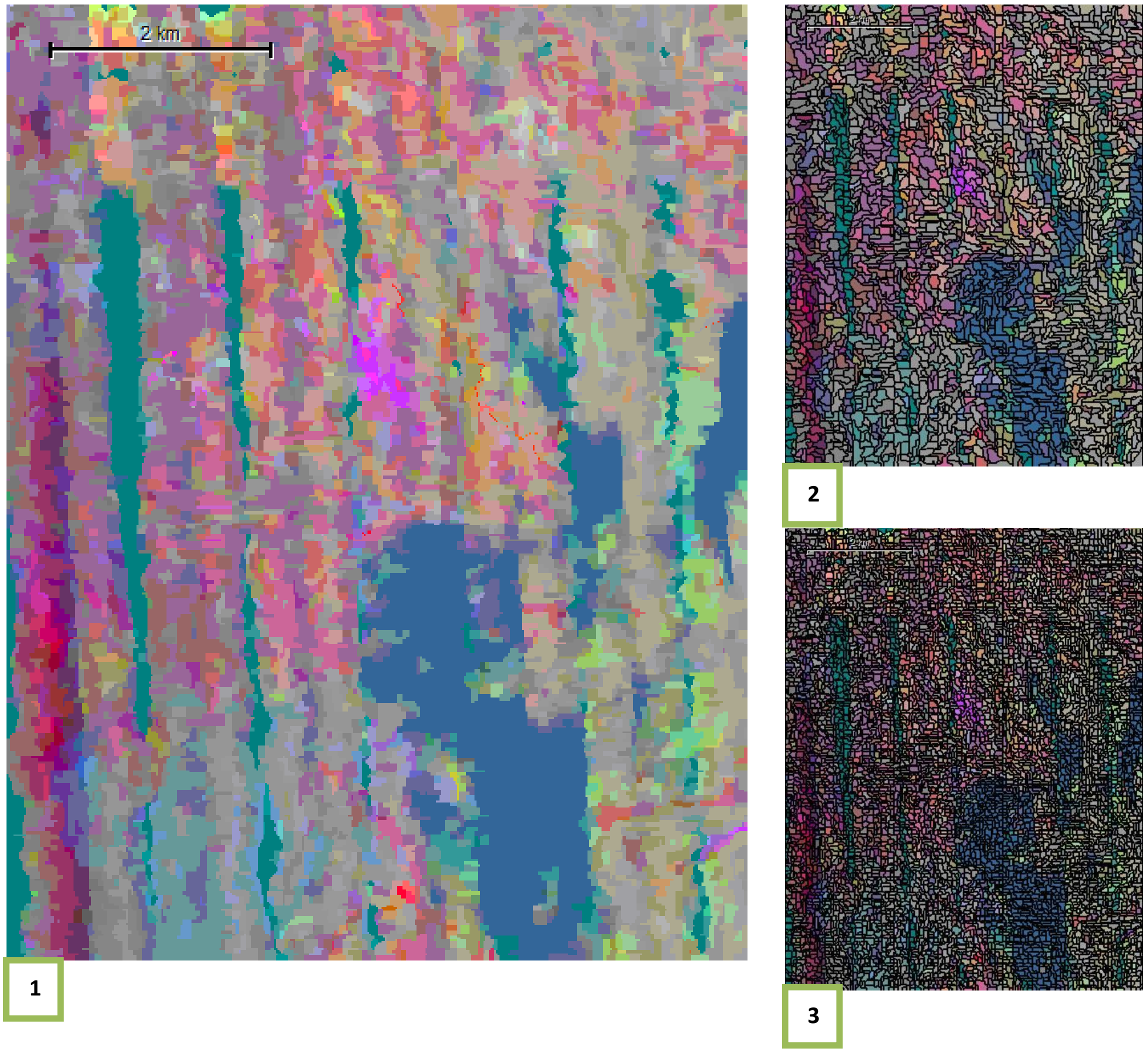

Figure 47: MNF CASI 2m image (see figure 1) and segmentation MNF transformed CASI 2m (for segmentation see figure 2) and 5m (for segmentation see figure 3) spatial resolution imagery.

Figures 48.1 and 48.2, below, illustrate the classification result (class distribution based on spectral signatures), resulting from using TTA mask-based (see figures 22 and 23) random samples for groups A and B respectively.

For all classification results illustrated below, one should refer to the colour key of figure 21.

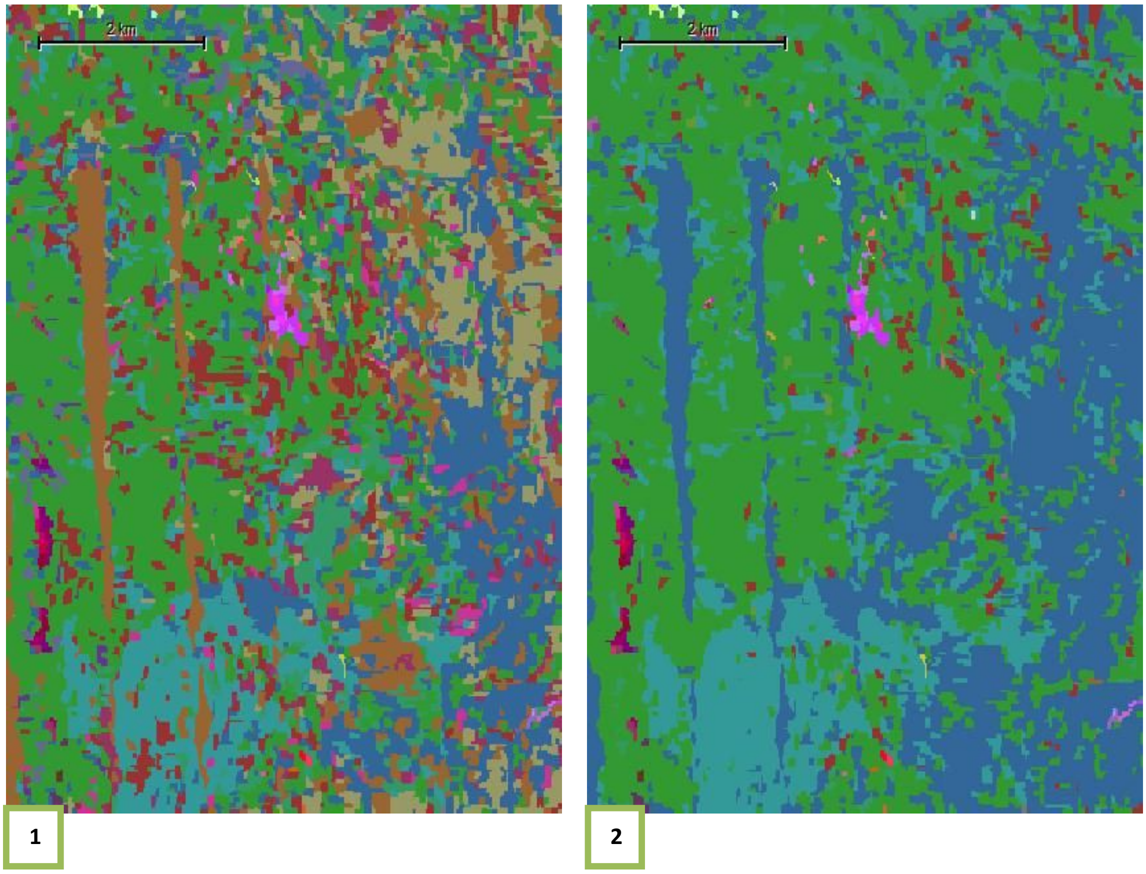

Figure 48: MNF CASI 2m spatial resolution classification result for group A (see figure 1) and B (see figure 2) classes respectively.

3.3.2 MNF transformed Hyperion imagery

Eleven (11) MNF bands were extracted from the Hyperion image and were all given equal weight (1) during segmentation and classification. The MNF transformed Hyperion image (see figure 49.1) was segmented with multi-resolution segmentation. The level used for classification was created with scale factor 10, colour factor 0.8, compactness 0.5 (see figure 49.2 and 49.3).

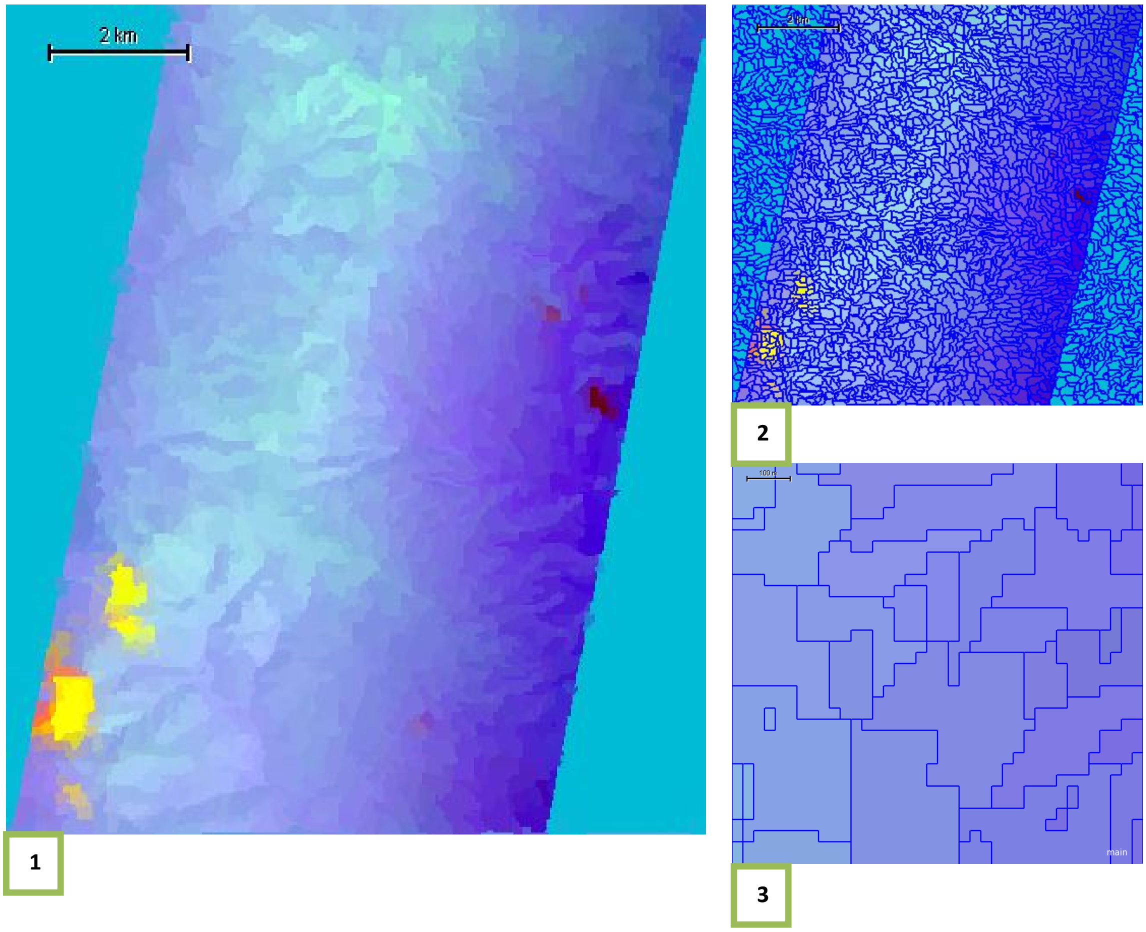

Figure 49: MNF transformed Hyperion image (see figure 1), segmentation (see figure 2) and zoomed in segmentation (see figure 3).

Figures 50.1 and 50.2, below, illustrate the classification result (class distribution based on spectral signatures), as taken using random samples from the TTA masks of figures 22 and 23 for groups A and B respectively.

For all classification results illustrated below, one should refer to the colour key of figure 21.

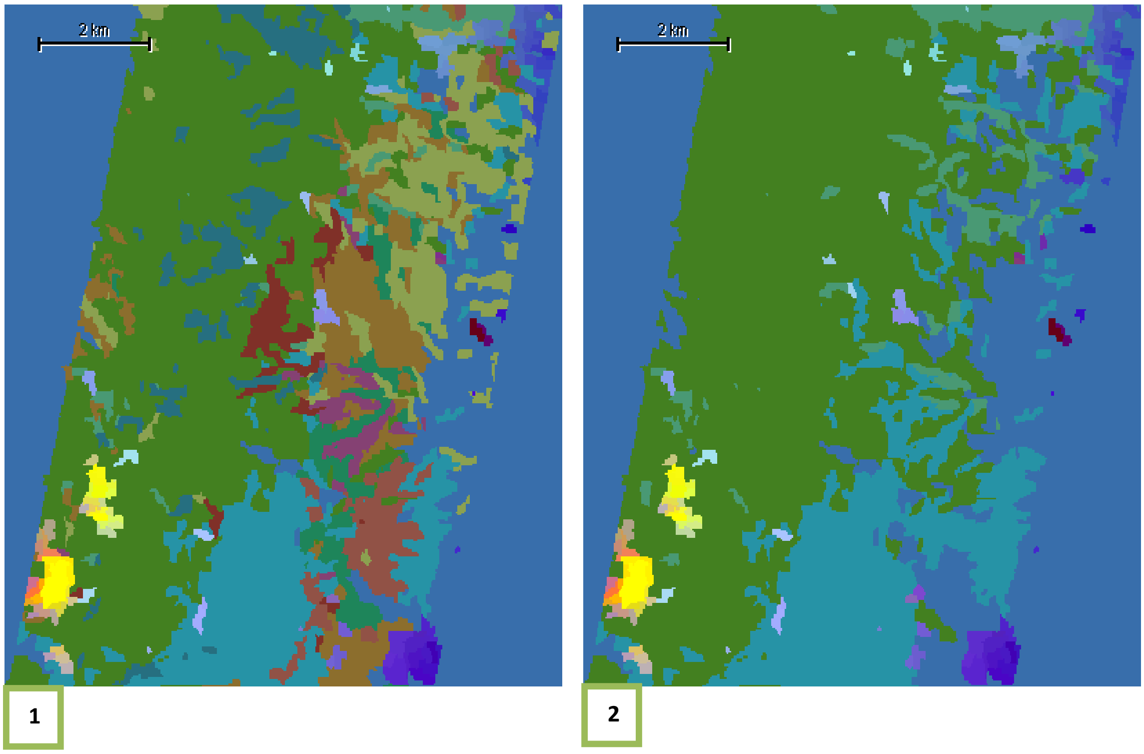

Figure 50: MNF transformed Hyperion imagery classification results for group A (see figure 1) and B (see figure 2) classes respectively.

3.3.3 Classification accuracies for MNF transformed hyperspectral imagery

As opposed to the PCA transform, the MNF transform increased the accuracy of classification, while reducing the data processing time significantly (approximately 95% reduction in processing time), as seen in table 7. According to Xiang *et al.*, (2009), the MNF transform is an effective method for noise removal, which is the main limitation in achieving better forest tree species classification results and our results support this conclusion. MNF transformed data gave improved accuracies in comparison to PCA, which failed to reduce noise.

MNF	**CASI 2m**		**HYPERION**	
	Group A	Group B	Group A	Group B
Overall Accuracy	0.44	0.75	0.44	0.69
KIA	0.34	0.63	0.35	0.53

Table 8: Accuracies for classification results of MNF projects relative to the ground data generated TTA mask

3.4 OBIA on Hyperspectral Imagery after Feature Selection

This band selection technique is based on selecting bands where the spectral signatures of the species of interest is distinctive in comparison to that of the rest of the species of interest. Reflectance of all species of interest for the most abundant tree species categories in Taxiarchis forest is plotted against that of all other species of interest and a spectral signature is created for each tree species. Each spectral reflectance value is correlated to three values above and below it, within the spectral range. Areas of the spectrum, where there is a (negative or positive) correlation between signatures and thus different species seem to be well separated from each other, are selected. The bands of interest and ultimately selected are those where correlation values are below 0.98 (98%) for at least two classes (see appendix V).

3.4.1 OBIA on CASI 2m hyperspectral imagery after band selection

In figure 51 we see an example of how the spectral signatures of different species vary. At around 870 nm for example there is a peak for the spectral signature of *Pinus brutia* in relation to the rest of the species considered. This area represents the infrared (IR) area of the spectrum, where it is well know that vegetation reflects well.

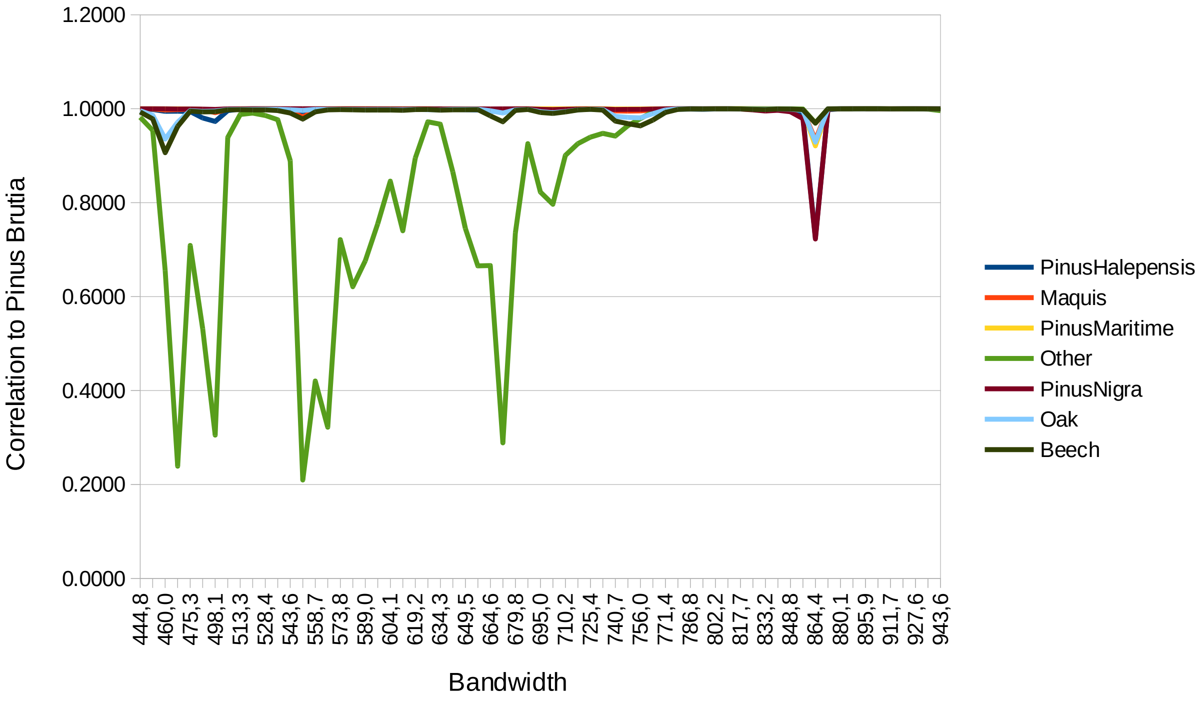

Figure 51: Correlation of spectral signatures of main tree species/classes to *Pinus brutia* at different spectral bandwidths.

After areas of the spectrum, where spectral signatures are distinct from each other, are selected for each species, the reflectance for each species (times 1000 for better separation) is plotted against bandwidth, clearly showing the areas of the spectrum where reflectance is high and tree species' spectral signatures are most distinctive (the bands selected can be found in Appendix III).

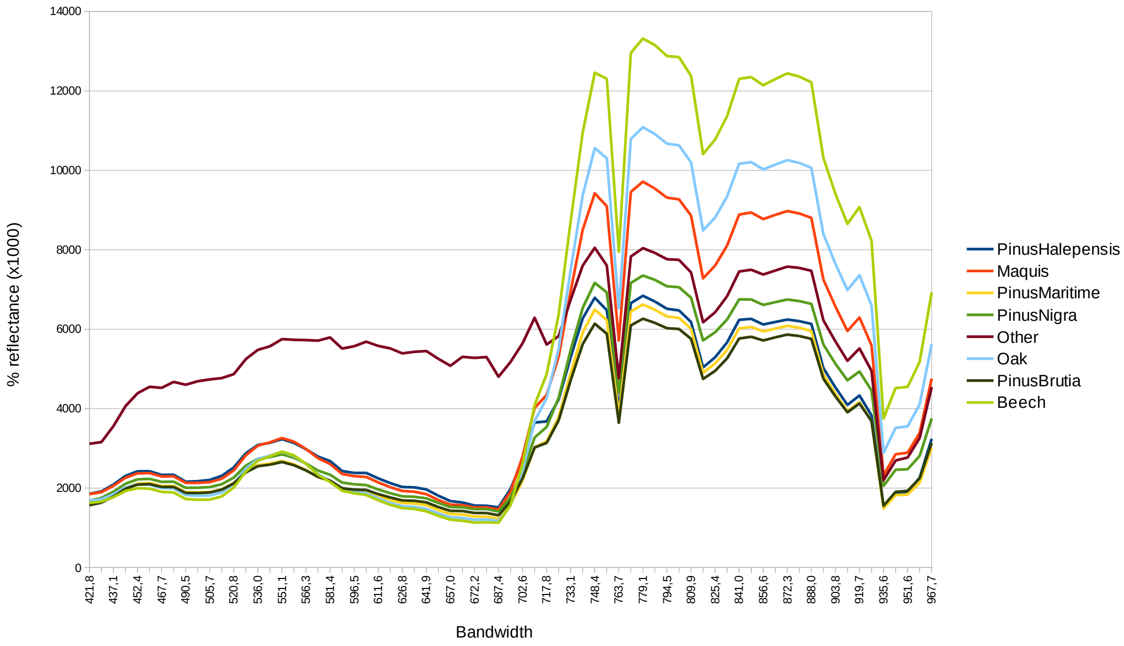

Figure 52: Correlation graph for different tree species (% reflectance is multiplied by 1000 for better visual separation between spectral signatures of classes).

The CASI image of 2m spatial resolution with selected bands (14 spectral bands taken into account with equal weights for the segmentation and classification procedures) based on tree species' spectral signatures was segmented with multi-resolution segmentation. The level used for classification was created with scale factor 80, colour factor 0.8, compactness 0.5.

Figures 53.1 and 53.2, below, illustrate the classification result (class distribution based on spectral signatures), as taken using random samples from the TTA masks of figures 22 and 23 for groups A and B respectively.

For all classification results illustrated below, one should refer to the colour key of figure 21.

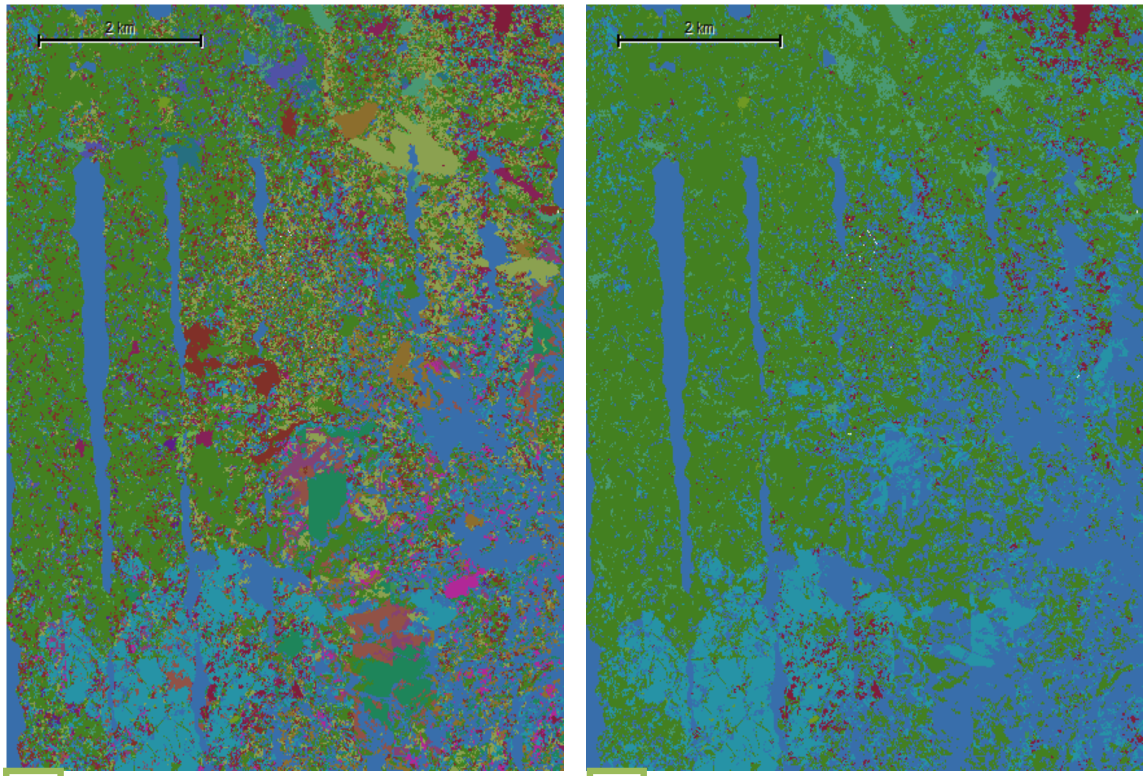

1

2

Figure 53: CASI 2m spatial resolution classification result based on correlation between spectral signatures for group A (see figure 1) and B (see figure 2) classes respectively.

3.4.2 OBIA on Hyperion imagery after band selection

Again, the example of correlation of the reflectance between oak and other tree species demonstrates the logic of this band selection method.

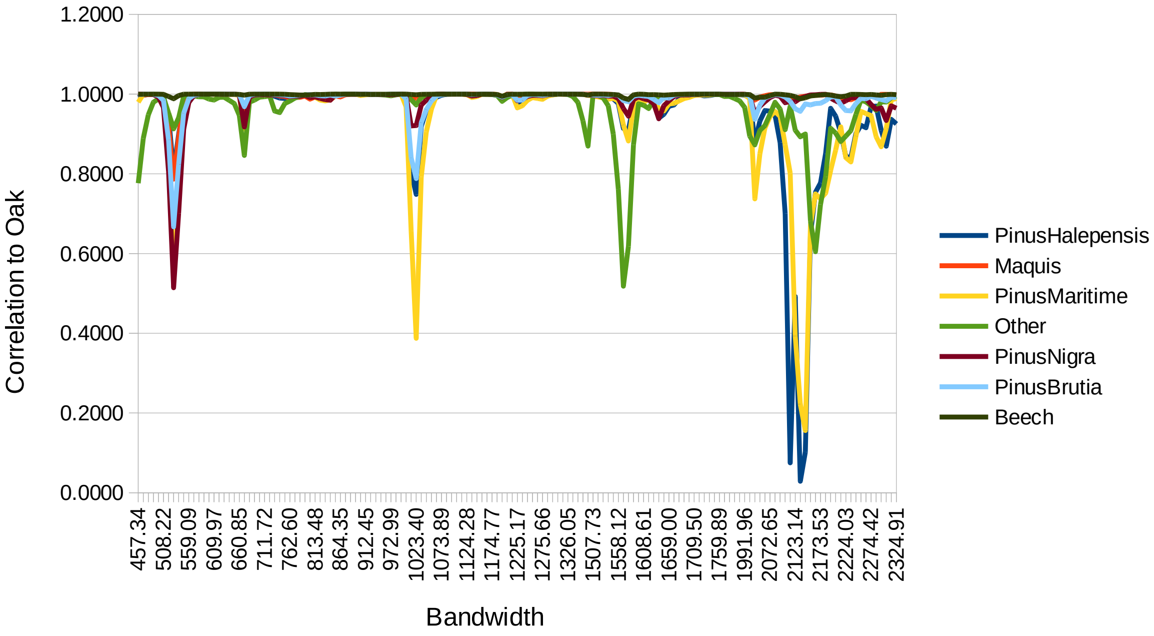

Figure 54: Correlation of spectral signatures of main tree species/classes to Oak at different spectral bandwidths.

For the Hyperion image we see that the reflectance of trees is better separated higher along the IR in comparison to the CASI imagery and thus according to the data at hand a different set of bandwidths are selected.

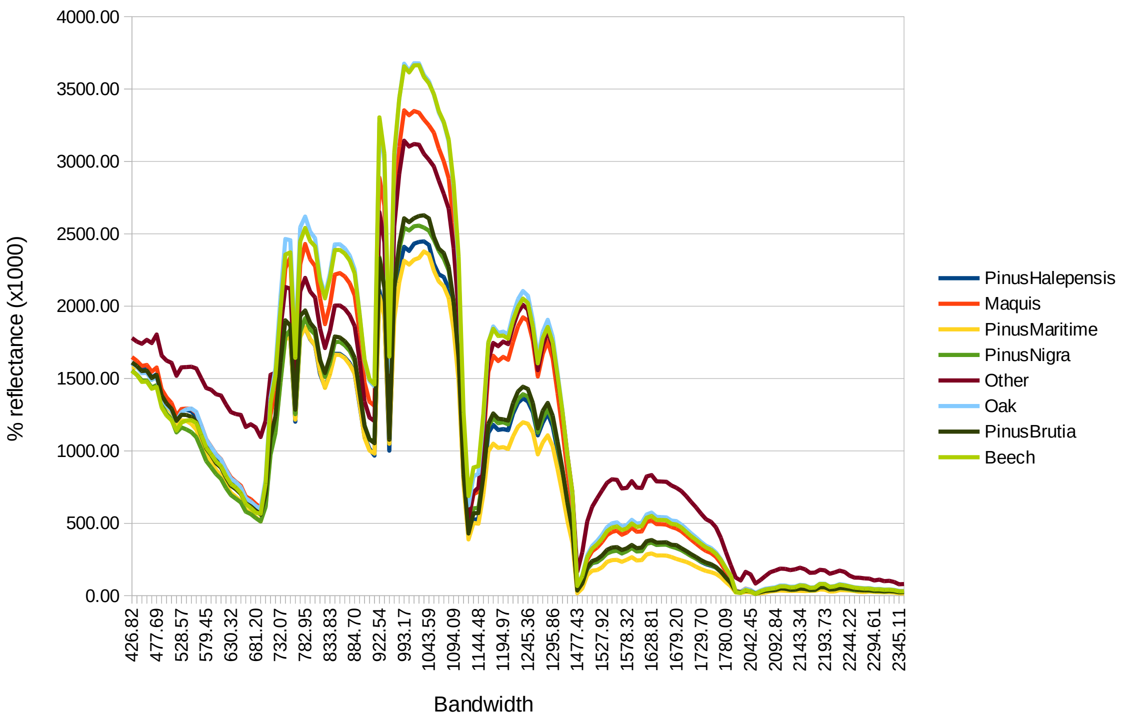

Figure 55: Correlation graph for different tree species (% reflectance is multiplied by 1000 for better visual separation between spectral signatures of classes).

The number of selected spectral bands is 25 and they were all taken into account with equal weights for during the segmentation and classification procedures. The Hyperion image was segmented with multi-resolution segmentation. The level used for classification was created with scale factor 10, colour factor 0.8, compactness 0.5.

Figures 56.1 and 56.2, below, illustrate the classification result (class distribution based on spectral signatures), as taken using random samples from the TTA masks of figures 22 and 23 for groups A and B respectively.

For all classification results illustrated below, one should refer to the colour key of figure 21.

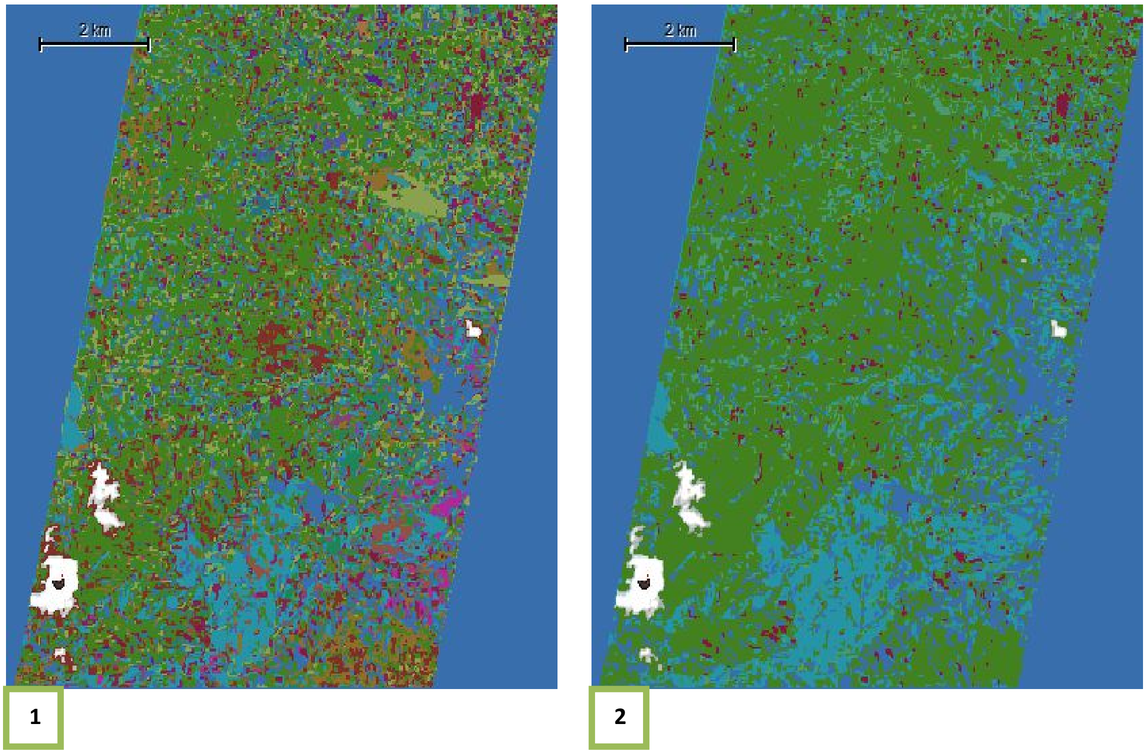

Figure 56: Hyperion classification result based on correlation between spectral signatures for group A (see figure 1) and B (see figure 2) classes respectively.

3.4.3 Classification accuracies for hyperspectral imagery with band selection based on correlation of species' spectral signatures

This band reduction method, through the selection of bands of hyperspectral imagery were the spectral signature of classes are most distinct proved useful in reducing the data and the processing time, but not in increasing accuracy, neither resulting in a major accuracy reduction. However, it gave better results in comparison to the PCA method, but worst in comparison to the MNF method for band reduction.

Signature correlation based selection	**CASI**		**Hyperion**	
	Group A	Group B	Group A	Group B
Overall Accuracy	0.45	0.70	0.39	0.64
KIA	0.35	0.55	0.28	0.45

Table 9: Accuracies for classification results of correlation between forest tree spectral signatures relative to the ground data generated TTA mask

3.5 OBIA with Fuzzy Analysis: Classification Improvement Using Physiographic Characteristics of Forest Trees

Based on the physiographic behaviour of tree species in Greek forest ecosystems, listed in table 10, the MNF transformed CASI (2 m spatial resolution), the MNF transformed Hyperion and the Landsat imageries were improved by entering fuzzy logic restrictions in tree species' (or classes') membership functions and evaluated in terms of their classification accuracies. These images gave the best accuracies during the previous results section, where classification was solely based on the spectral signatures of classes (group A and B). In addition, group B classes, consisting of unmixed classes, each representing one tree species, having given the best results, will be the ones concerning the following analyses and OBIA classifications of all following sections.

Table 10, below is based on a study by Rokos *et al*. (1992), on the distribution of Mediterranean crops and vegetation types, as a basis for image analysis expert system rules.

Tree species	**Criteria for the presence of a tree species, family or group**			
		Elevation (m)	Slope (%)	Aspect (N, S, E, W, NE, NW, SE and SW)
Pinus nigra	Rarely	400-800	10-35	W, SE, SW
	Often	800-2000	35-50	N, E
	Very often	-	>50	NE, NW
Pinus halepensis/ Pinus brutia	Rarely	800-1000	>50	N
	Often	600-800	0-10	E, W, NE, NW, SE
	Very often	0-600	10-50	S, SW
Pinus pinea	Rarely	800-1000		N, E, NE, NW
	Often	400-800	0-10, 35-50	S
	Very often	0-400	10-35	SE, SW
Beech	Rarely	600-800	10-35	NE, SE, SW

	Often	800-1200	35-50	N, S, W, NE
	Very often	1200-2000	>50	E
Castanea	Rarely	0-800	10-35	S, W, NW, SE
	Often	-	>50	N
	Very often	800-2000	35-50	E, NE
Oak	Rarely	1000-1200	>50	N, S, NE, NW, SE, SW
	Often	0-600	0-10, 35-50	W
	Very often	600-1000	10-35	E
Fir	Rarely	400-800	>50	S, SE, SW
	Often	-	35-50	E, W, NW
	Very often	800-1600	10-35	N, NE
Needleleaf species	Rarely	1200-2000	>50	S, W, NE, NW
	Often	800-1200	0-10, 35-50	-
	Very often	0-800	10-35	N
Broadleaf species	Rarely	1000-1600	>50	W, NW, SW
	Often	0-400	0-10, 35-50	E
	Very often	400-1000	10-35	S, SE

Table 10: Physiographic parameters related to elevation, slope and aspect requirements of tree species. 'Rarely' refers to a physiographic parameter attributed to 0-20% of trees belonging to a species, family or group, 'often' is attributed to 20-60%, while 'very often' to 60-90% (Rokos *et al*,. 1992).

After a series of trials applying the parameters listed in table 10, it was concluded that certain parameters were effective, whereas others were not improving our results. This may be attributed to the geographical variation of subspecies and behaviour of forest trees in particular environments, as well as radiometric and spatial resolution deficiencies in our imagery. More specifically, the third layer of the GDEM map, namely the aspect gave very poor results and we concluded that it would be best to be omitted from the set of physiographic restrictions used in fuzzy analysis. This may be due to the resolution of the GDEM (greater than tree crown diameter), as well as the difference in resolution between the CASI (2 and 5 m spatial resolution) and Hyperion (30 m spatial resolution) images in comparison to the GDEM (25 m spatial resolution).

Using ER Mapper software we subsequently extrapolated the range of tree distribution of the tree species of group B, using the vector data, onto the exiting GDEM available. The results are presented in table 11. These parameters, which are specifically related to the behaviour the Taxiarchis forest trees gave improved classification results and a greater degree of confidence in terms of tree behaviour for our particular area.

Tree species	**Elevation (m)**	**Slope (%)**	**Aspect (°)**
Maquis	285-888	0-114	1-360
Castanea	694-753	12-32	207-262
Beech	567-1129	1-90	1-360
Pinus brutia	423-746	1-103	1-360
Pinus sylvestris	575-1013	2-76	14-360
Pinus maritime	507-657	1-64	1-360
Pinus nigra	654-1064	0-90	1-360
Pinus pinea	557-600	13-48	178-297
Oak	468-1143	0-101	1-360

Table 11: Range of physiographic characteristics extrapolated using the ground data and the GDEM.

Several samples from groups, such as Castanea, *Pinus sylvestris*, *Pinus maritime* and *Pinus Pinea* with limited area distribution Taxiarchis forest, were taken manually, in addition to the already existing samples. However, *Pinus pinea* and *Pinus sylvestris* classes were excluded from the classification process in the case of the Landsat imagery; due to the fact the samples were not satisfactory in number and distribution, to give a representative spectral signature.

The parameters for tree distribution in relation to the terrain of Taxiarchis forest (elevation and slope), as presented in table 11, were entered for each individual class on a fuzzy logic basis in order to improve classification. A process of trial and error, based on the classification and the overall accuracy per class, the K index (or KIA[6]), as well as user[7] and producer[8] accuracies, assisted in deciding upon the fuzzy area of distribution for each tree species. As in previous classification processes, a nearest neighbour feature space was created with some additional parameters taken into account, namely brightness for the Landsat imagery and Standard Deviation for the mean value of particular bands of the MNF transformed Hyperion and CASI imagery.

The limits, left and right of the function are based on the range of the vector data as extrapolated from the GDEM in relation to the ground sampling (see table 10). Depending on producer and user accuracies, the range was restricted or loosened and several classification trials were carried out, as too reduce conflict between classes during classification at a minimum. This process gave rise to a best possible classification result, presented in the following sections.

Figure 57, below shows an example of the form of membership function entered for the elevation range of a class (in this case, beech) for fuzzy analysis based classification for the Landsat imagery.

---

[6] Reflects the difference between actual agreement and the agreement expected by chance. Kappa of 0.85 means there is 85% better agreement than by chance alone (Congalton, 1991).

[7] **User's accuracy** corresponds to error of commission (inclusion). Calculated as: Number correctly identified in a given map class / Number claimed to be in that map class (Congalton, 1991).

[8] **Producer's accuracy** corresponds to error of omission (exclusion). Calculated as: Number correctly identified in ref. plots of a given class / Number actually in that reference class (Congalton, 1991).

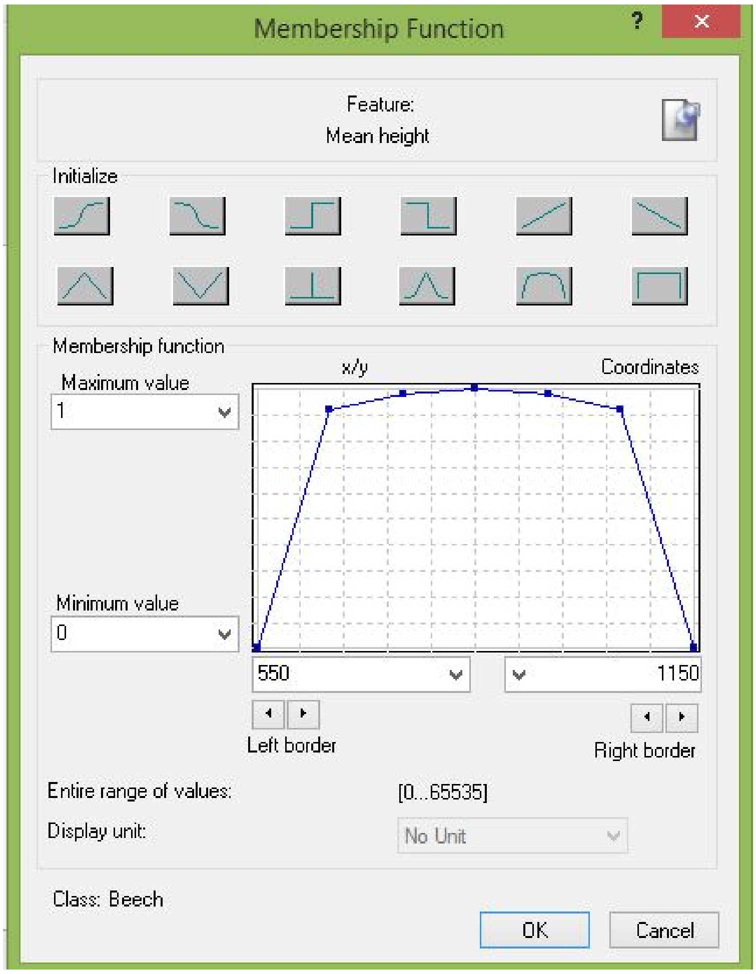

Feature:
Mean height

Maximum value: 1

Minimum value: 0

Left border: 550

Right border: 1150

Entire range of values: [0...65535]

Display unit: No Unit

Class: Beech

Figure 57: Membership function example for fuzzy analysis based classification for the elevation (m) range of beech.

As in figure 57, figure 58, depicts the range for the degree of slope for beech, as an example of the form of fuzzy analysis based classification.

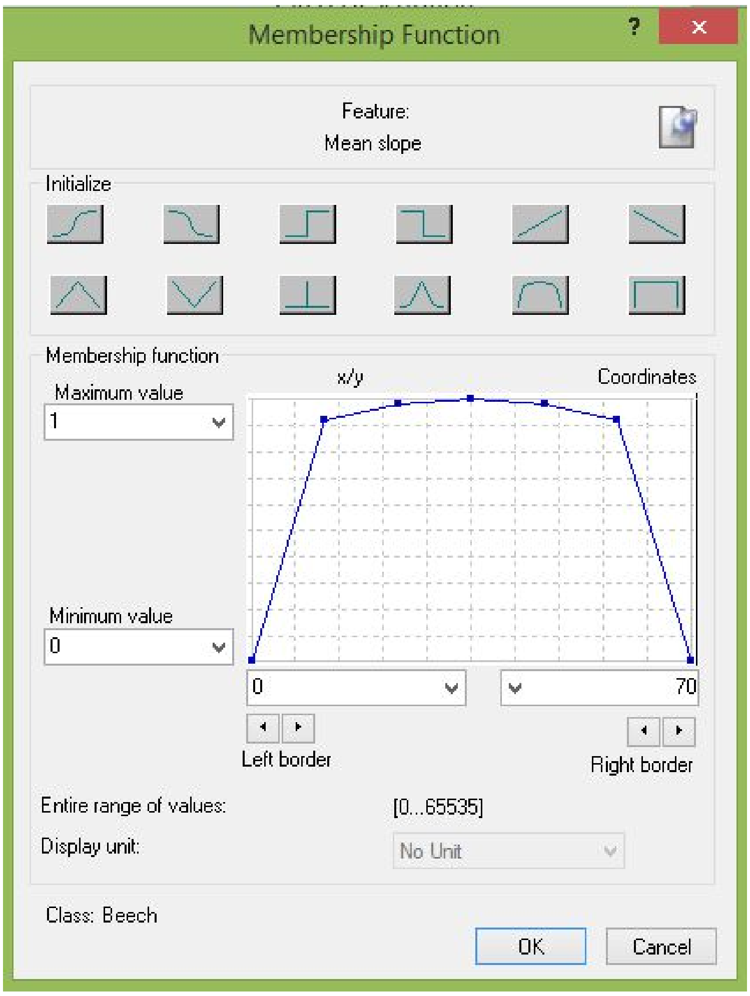

Feature:
Mean slope

Maximum value: 1

Minimum value: 0

Left border: 0

Right border: 70

Entire range of values: [0...65535]

Display unit: No Unit

Class: Beech

Figure 58: Membership function example for fuzzy analysis based classification for the degree of slope (%) range of beech.

For this part of the study we restricted our training in areas in those provided by group B categories. This is due to the high accuracy of classification they exhibited, as well as the straightforwardness in determining a spectral signature per species.

3.5.1 Landsat Imagery Object Based Image Analysis (OBIA) with Fuzzy Analysis Based on Physiographic Parameters

The Landsat image was segmented with multi-resolution segmentation. The level used for classification was created with scale factor 20, colour factor 0.8 and compactness 0.5, as before.

Figure 59, below, illustrate the classification result (class distribution based on spectral signatures, as well as restrictions based on the physiographic parameters of table 11, employing fuzzy logic).

For all classification results illustrated below, one should refer to the colour key of figure 21.

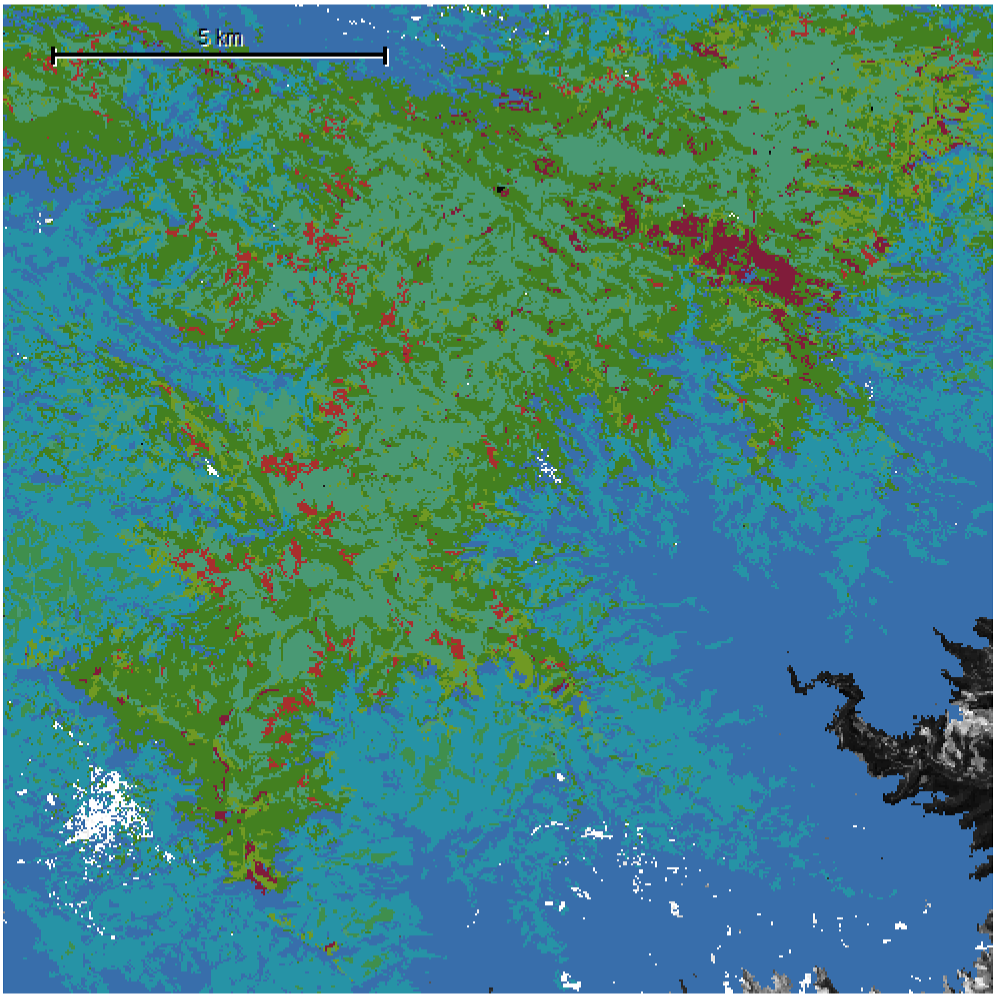

Figure 59: Classification result for Landsat image after fuzzy analysis-based classification.

The accuracy results which were achieved after a process of trial-and-error in deciding upon the fuzzy range attributed to each physiographic parameter is presented in table 12, below. It should be noted that the *Pinus sylvestris* and *Pinus pinea* classes do not affect the overall accuracy and KIA score, as their distribution is limited in the area and thus sample size was not satisfactory to give rise to meaningful results for the spatial resolution of the Landsat imagery.

Class	Maquis	Castanea	Beech	Pinus Brutia	Pinus Sylvest.	Pinus Maritime	Pinus Nigra	Pinus Pinea	Oak
Producer	0.82	0.17	0.14	0.29	0.00	0.30	0.27	0.00	0.94
User	0.65	0.20	0.79	0.86	0.00	0.09	0.71	-	0.78
KIA Per Class	0.73	0.17	0.13	0.25	0.00	0.28	0.27	0.00	0.85
Overall Accuracy	0.73								
KIA	0.56								

Table 12: Fuzzy analysis-based classification accuracy assessment for the Landsat image.

Upon comparison with the classification accuracy results listed in appendix V (see results for Group B classes); we observe a slight drop in the KIA accuracy, as well as for the classes *Pinus brutia* and Beech. However, other classes, such as Castanea (not present in the classification based on spectral signatures alone) were present in this classification (mainly due to the additional samples taken), while *Pinus maritime* showed great improvement, as a class. Thus, even though the overall result for accuracy is worst, more classes are present and due to the limited number of samples available the accuracy drops, as a result of insufficient training areas to create a spectral signature for certain species, which are known to be present from field studies.

Two additional indices have been employed for the classification evaluation, Classification Stability and Best Classification Result. The Classification Stability concerns a statistic type used for accuracy assessment and is depicted in figure 60, while the values for each class are listed in table 13. It is a measure for conflict between classes during the classification process. The difference between the best and the second best class assignment is calculated as a percentage. The statistical output displays basic statistical operations (number of image objects, mean, standard deviation, minimum value and maximum value) performed on the best-to-second values per class (eCognition Definiens Developer 7 Userguide, 2007).

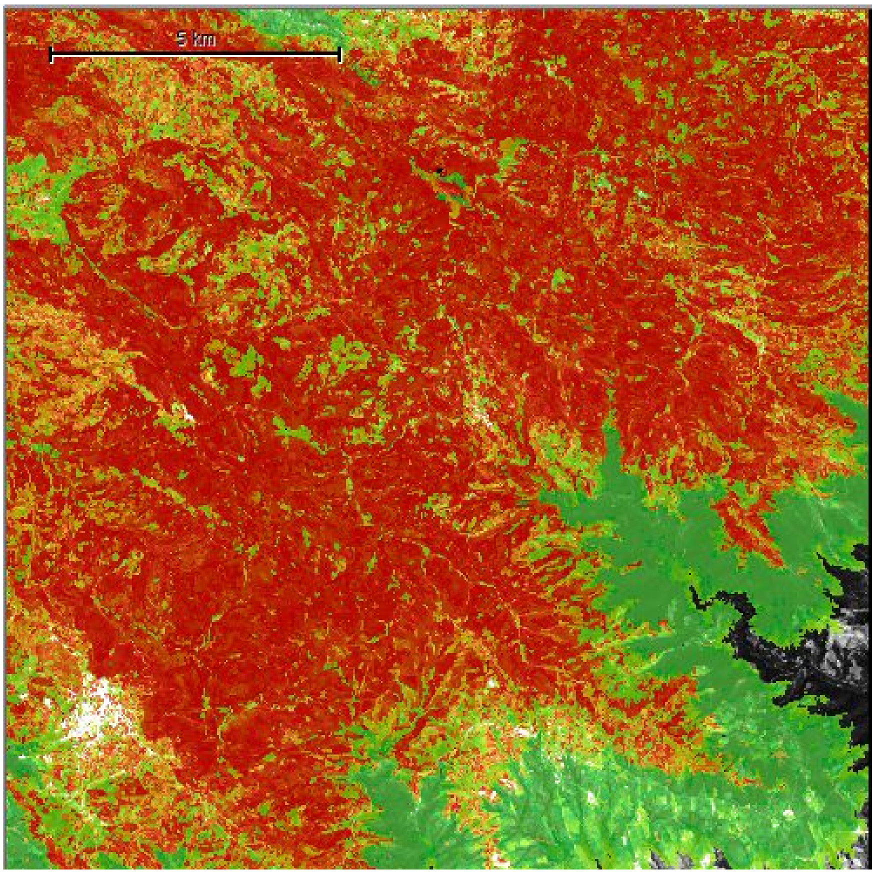

Figure 60: Classification Stability for the Landsat image after entering a fuzzy range for physiographic parameters. Red shows areas with high conflict between classes, followed by yellow and green for more stable classification results successively.

From the mapped Classification Stability, illustrated in figure 60, we conclude that the classification stability is low. Classes with a wide distribution, such as Maquis, *Pinus brutia* and Oak vary in stability, with Maquis representing a particularly unstable class (see SD in table 13).

Class	Objects	Mean	SD	Minimum	Maximum
Maquis	35104.00	0.27	0.28	0.00	0.94
Castanea	1405.00	0.03	0.03	0.00	0.21
Beech	19084.00	0.06	0.06	0.00	0.95
PinusBrutia	25426.00	0.06	0.06	0.00	0.35
PinusSylvestris	2823.00	0.02	0.02	0.00	0.14
PinusMaritime	1739.00	0.04	0.03	0.00	0.10
PinusNigra	1752.00	0.02	0.03	0.00	0.23
PinusPinea	0.00				
Oak	28424.00	0.05	0.07	0.00	0.76

Table 13: Classification Stability per class for the Landsat imagery after fuzzy analysis-based classification.

The Best Classification Result is another form of statistical analysis for evaluating classification accuracy (see figure 61) and displays a statistic type used for accuracy assessment. It addresses the issue of whether a particular segment has been assigned to a class well suited to the spectral signature of each tree category and the respective parameters. The statistical output for the best classification result is evaluated per class. Basic statistical operations are performed on the best classification result of the image objects assigned to a class (number of image objects, mean, standard deviation, minimum value and maximum value) (eCognition Definiens Developer 7 Userguide, 2007).

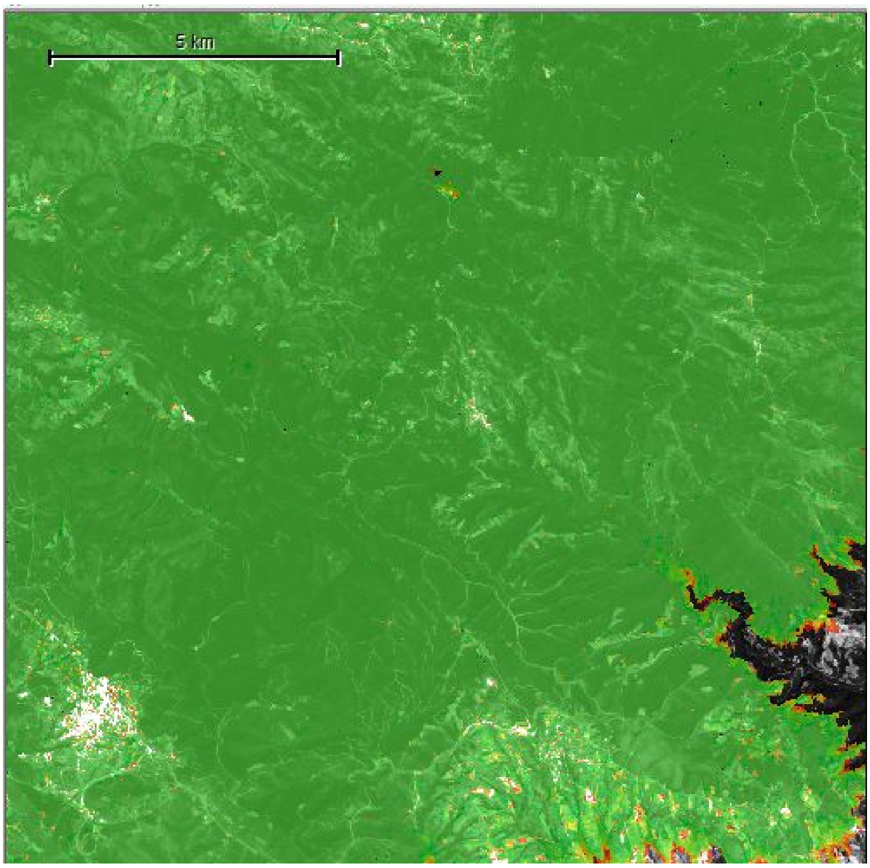

Figure 61: Best classification result for the Landsat image after entering a fuzzy range for physiographic parameters. Red shows areas with high conflict between classes, followed by yellow and green for more stable classification results successively.

Figure 61, representing a map for the Best Classification Result statistic shows that most segments have been attributed to a satisfactory degree to each class. Again Maquis, constitutes a class, which despite its wide distribution may be of high conflict with other classes and is followed by *Pinus maritime*, which is not surprising, considering the likelihood of conflict between Pinus species with a restricted distribution in the area. All other classes, which are present in this classification have scored relatively well.

Class	Objects	Mean	SD	Minimum	Maximum
Maquis	35104.00	0.73	0.26	0.10	1.00
Castanea	1405.00	0.93	0.07	0.47	0.99
Beech	19084.00	0.81	0.22	0.10	1.00
PinusBrutia	25426.00	0.81	0.19	0.10	1.00
PinusSylvestris	2823.00	0.93	0.07	0.26	1.00
PinusMaritime	1739.00	0.75	0.21	0.12	0.99
PinusNigra	1752.00	0.92	0.10	0.11	1.00
PinusPinea	0.00				
Oak	28424.00	0.92	0.13	0.10	1.00

Table 14: Best Classification result per class for the MNF transformed CASI image after fuzzy analysis-based classification.

3.5.2 MNF Transformed Hyperion Object Based Image Analysis (OBIA) with Fuzzy Analysis Based on Physiographic Parameters

The parameters for distribution in relation to the terrain of Taxiarchis forest (elevation and slope), as presented in table 11, were entered for each individual class in order to improve classification. As before, a process of trial and error, based on the classification the overall accuracy per class, the K index, as well as user and producer accuracies, assisted in deciding upon the fuzzy area of distribution for each tree species. As in previous classification processes, a nearest neighbour feature space was created with some additional parameters taken into account, namely brightness and Standard Deviation for Layers 4-11. SD for layers 1-3 was not taken into account due to high noise observed visually.

The MNF transformed Hyperion image was segmented with multi-resolution segmentation. The level used for classification was created with scale factor 10, colour factor 0.8, compactness 0.5.

Figure 62, below, illustrates the classification result (class distribution based on spectral signatures, as well as restrictions based on the physiographic parameters of table 11, employing fuzzy logic).

For all classification results illustrated below, one should refer to the colour key of figure 21.

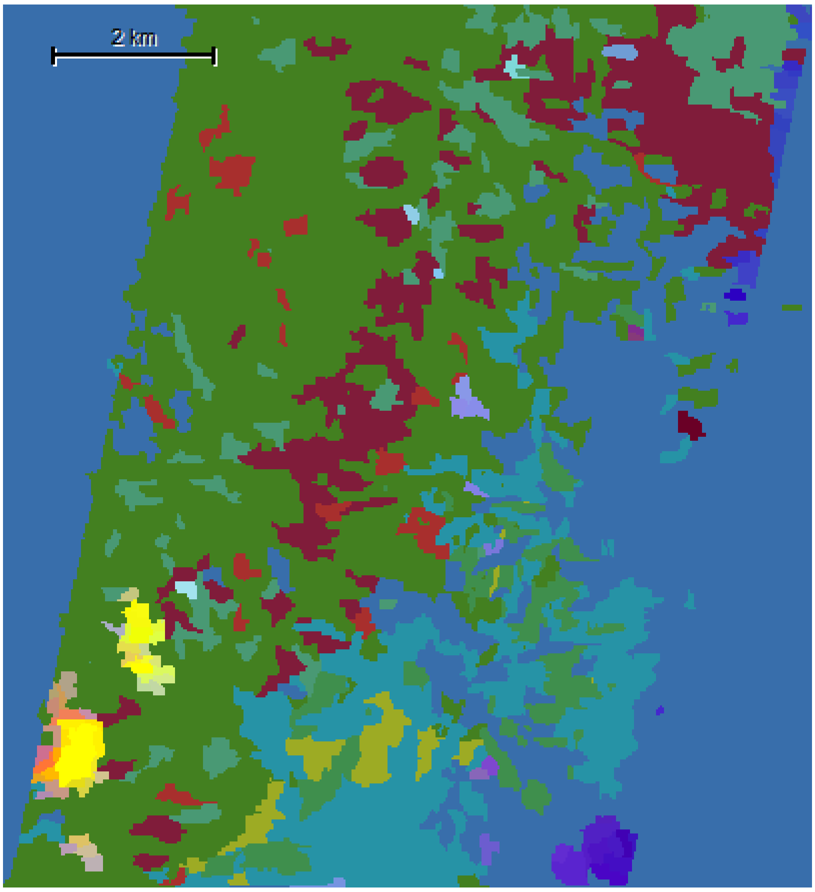

Figure 62: Classification result for MNF transformed Hyperion image after fuzzy analysis-based classification.

The accuracy results which were achieved after a process of trial-and-error in deciding upon the fuzzy range attributed to each physiographic parameter is presented in table 15, below. It should be noted that the *Pinus sylvestris* class does not affect the overall accuracy and KIA score, as its distribution is limited in the area and thus sample size was not satisfactory to give rise to meaningful results for the spatial resolution of the Landsat imagery.

Class	**Pinus Sylves.**	**Maquis**	**Castanea**	**Beech**	**Pinus Brutia**	**Pinus Maritime**	**Pinus Nigra**	**Pinus Pinea**	**Oak**
Producer	0.00	0.81	0.88	0.39	0.58	0.93	0.69	1.00	0.58
User	-	0.64	0.08	0.66	0.68	0.15	0.16	0.02	0.85
KIA Per Class	0.00	0.71	0.88	0.36	0.52	0.92	0.66	1.00	0.37
Overall Accuracy	0.63								
KIA	0.49								

Table 15: Fuzzy analysis-based classification accuracy assessment for the MNF transformed Hyperion image.

Upon comparison with the classification accuracy results listed in appendix V (see results for Group B classes, MNF results), we observe a significant, but not large drop in both the overall accuracy and the K index (KIA). However, the current classification, with the exception of the *Pinus sylvestris* class, includes many more classes and thus gives us a better tool for evaluating the biodiversity of the area.

The Classification Stability, as a measure for conflict between classes during the classification process, shows much reduced conflict in relation to the Landsat result (see figure 59), with the red areas (of high conflict) being less extensive and patched.

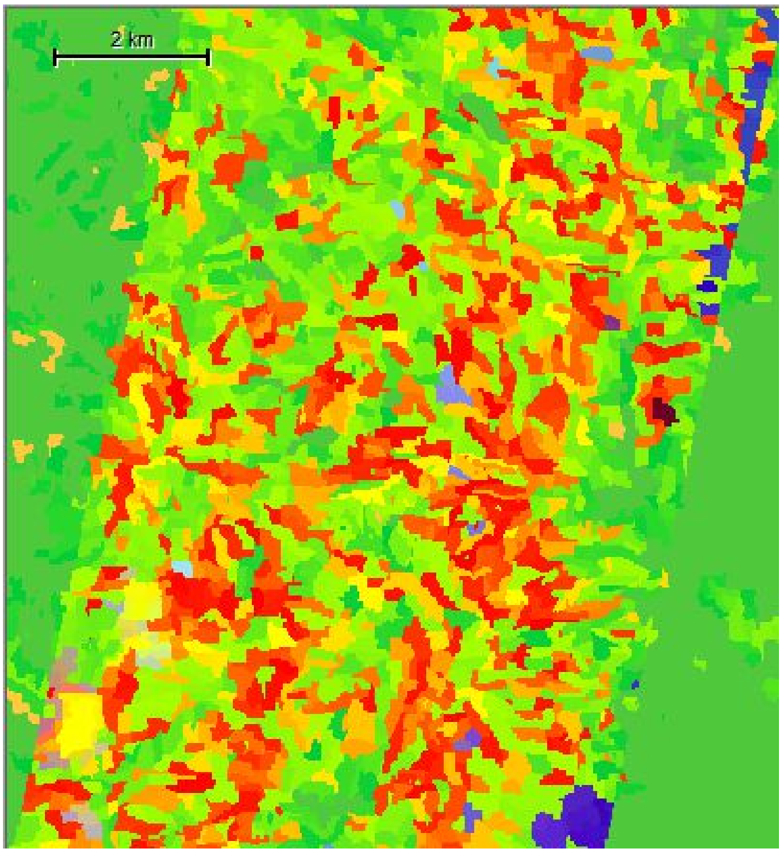

Figure 63: Classification stability for the MNF transformed Hyperion image after entering a fuzzy range for physiographic parameters. Red shows areas with high conflict between classes, followed by yellow and green for more stable classification results successively.

Indeed, looking at table 16, we observe that Classification Stability per class is quite high in all classes except in the cases of the *Pinus pinea* and Castanea classes, both classes with limited distribution and samples, thus with a relatively inaccurate spectral signature, which again proves to be a defining factor in classification accuracy.

Class	Objects	Mean	SD	Minimum	Maximum
Maquis	963.00	0.48	0.27	0.00	0.94
Castanea	30.00	0.07	0.09	0.00	0.46
Beech	132.00	0.14	0.15	0.00	0.75
PinusBrutia	245.00	0.14	0.13	0.00	0.76
PinusSylvestris	0.00				
PinusMaritime	77.00	0.10	0.11	0.00	0.48
PinusNigra	191.00	0.14	0.14	0.00	0.65
PinusPinea	24.00	0.06	0.04	0.00	0.20
Oak	938.00	0.16	0.12	0.00	0.78

Table 16: Classification Stability per class for the MNF transformed Hyperion image after fuzzy analysis-based classification.

The Best Classification Result, addressing the issue of whether a particular segment has been assigned to a class well suited to the spectral signature of each tree category and the respective parameters, is again improved in the Hyperion in comparison to the Landsat imagery. Figure 63 shows a very limited distribution of red patches (representing a questionable result) with most area being covered in green.

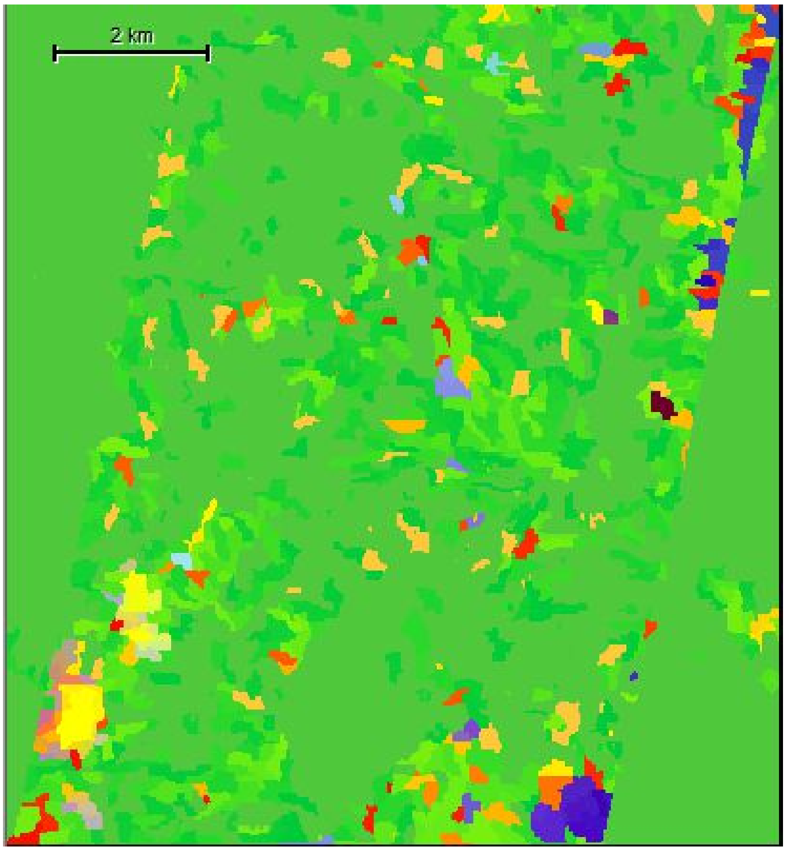

Figure 64: Best classification result for the MNF transformed Hyperion image after entering a fuzzy range for physiographic parameters. Red shows areas with high conflict between classes, followed by yellow and green for more stable classification results successively.

According to table 17, all classes scored very high for the Best Classification Result statistic, which shows that classification of most segments has a high probability of being accurate for the MNF transformed Hyperion image.

Class	Objects	Mean	SD	Minimum	Maximum
Maquis	963.00	0.69	0.23	0.11	0.99
Castanea	30.00	0.45	0.17	0.11	0.99
Beech	132.00	0.44	0.18	0.10	0.98
PinusBrutia	245.00	0.54	0.18	0.10	0.96
PinusMaritime	77.00	0.58	0.15	0.26	0.99
PinusNigra	191.00	0.47	0.18	0.11	0.99
PinusPinea	24.00	0.64	0.22	0.27	0.99
Oak	938.00	0.51	0.17	0.10	1.00

Table 17: Best Classification Result per class for the MNF transformed CASI image after fuzzy analysis-based classification.

3.5.3 MNF Transformed CASI 2m Spatial Resolution Object Based Image Analysis (OBIA) with Fuzzy Analysis Based on Physiographic Parameters

The parameters for distribution in relation to the terrain of Taxiarchis forest (elevation and slope), as presented in table 11, were entered for each individual class in order to improve classification. As before, a process of trial and error, based on the classification the overall accuracy per class, the K index, as well as user and producer accuracies, assisted in deciding upon the fuzzy area of distribution for each tree species. As in previous classification processes, a nearest neighbour feature space was created with some additional parameters taken into account, namely brightness and Standard Deviation for Layers 2-6. Layer 1 SD was not taken into account due to high noise observed visually.

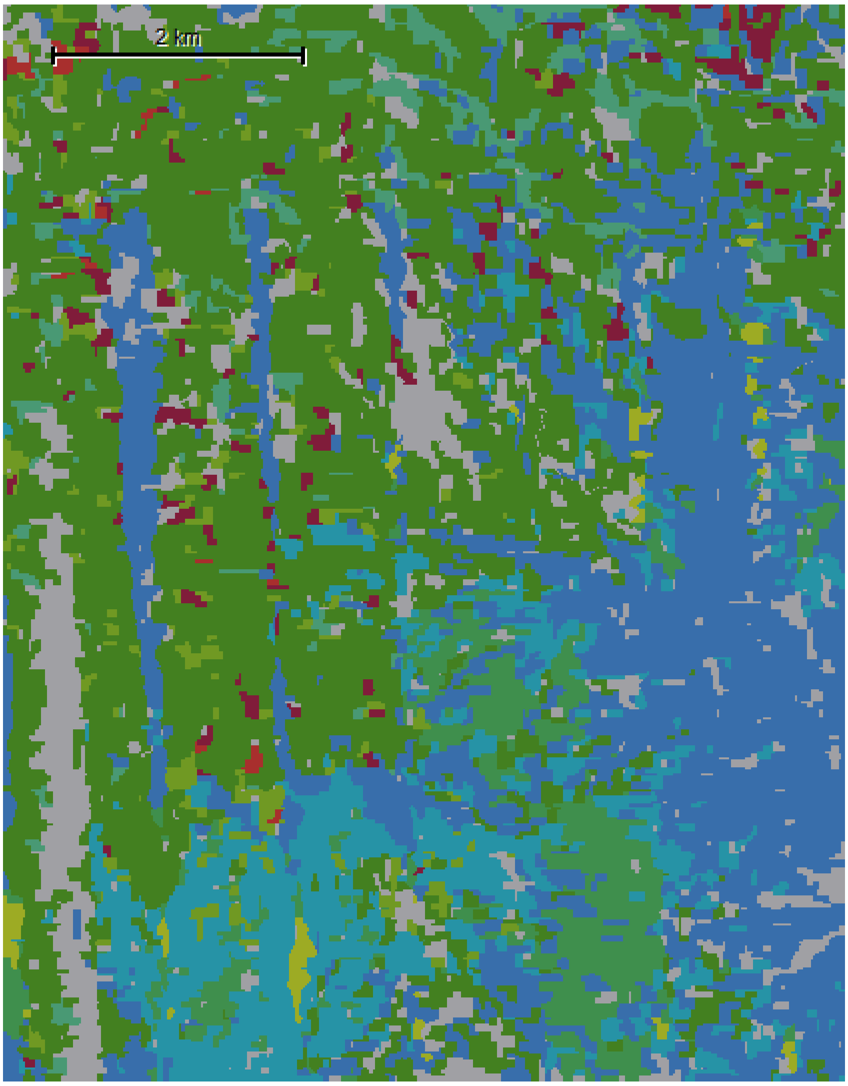

Table 18: Classification result for MNF transformed CASI image after fuzzy analysis-based classification.

The accuracy of the classification for the MNF transformed CASI after entering physiographic restrictions, according to a fuzzy-based logic, is considerably lower (by 1.2 for Overall Accuracy and 1.4 for KIA) in comparison to the result based on spectral signatures (see appendix V). Most classed represented have risen in accuracy (looking at KIA per class), including Maquis, Castanea (with a great increase in accuracy), *Pinus maritima* (with a great increase in accuracy), *Pinus nigra*, *Pinus pinea* (with great increase in accuracy). However, the remaining classes had dropped considerably.

Class	**Maquis**	**Castanea**	**Beech**	**Pinus Brutia**	**Pinus Sylvestris**	**Pinus Maritime**	**Pinus Nigra**	**Pinus Pinea**	**Oak**
Producer	0.72	0.25	0.44	0.71	0.41	0.52	0.38	0.90	0.74
User	0.74	0.10	0.60	0.79	0.04	0.09	0.42	0.06	0.86
KIA Per Class	0.62	0.25	0.41	0.65	0.40	0.49	0.37	0.90	0.57
Overall Accuracy			0.71						
KIA			0.58						

Table 19: Fuzzy analysis-based classification accuracy assessment for the MNF transformed CASI image.

The Classification Stability, concerning conflict between classes during the classification process, as depicted in figure 65 is better than the Landsat image, but worst in comparison to the MNF transformed Hyperion imagery, with extensive red patches.

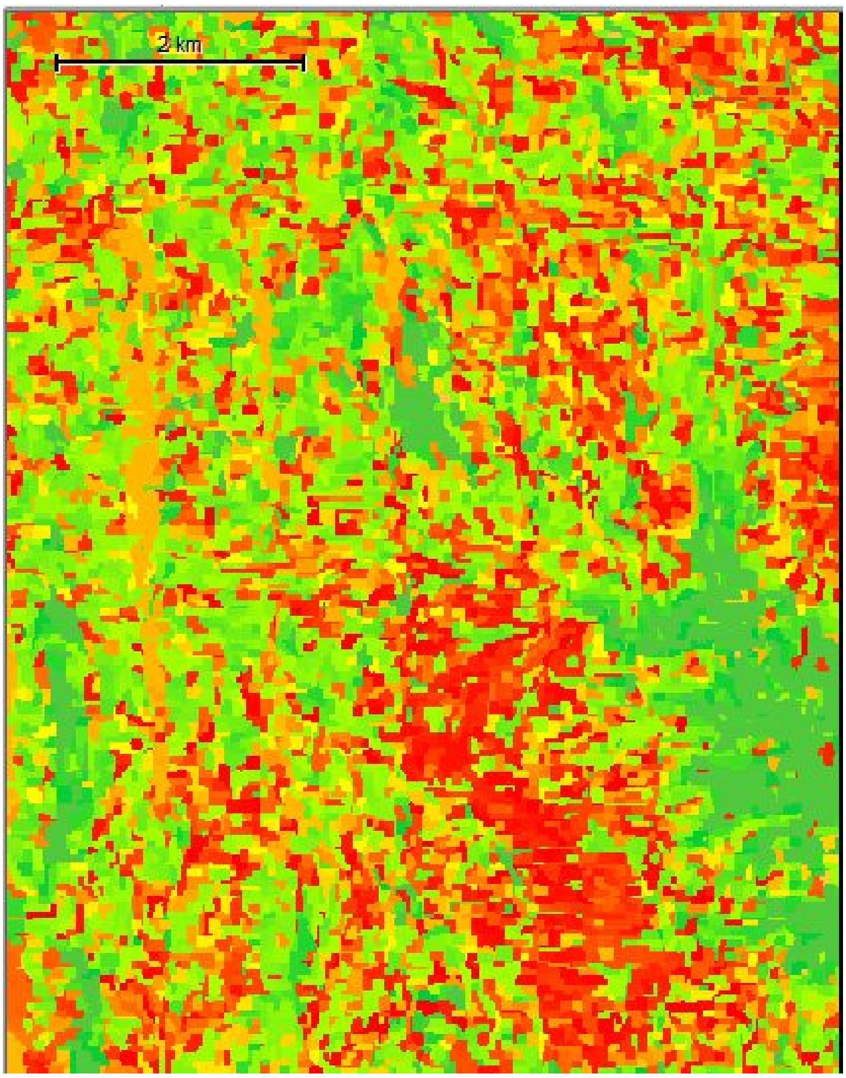

Figure 65: Classification Stability for the MNF transformed CASI image after entering a fuzzy range for physiographic parameters. Red shows areas with high conflict between classes, followed by yellow and green for more stable classification results successively.

As shown in table 19, the classes with particularly low stability include Castanea, *Pinus sylvestris*, *Pinus maritime*, *Pinus nigra* and *Pinus pinea*. This could be attributed to both their similarities in spectral signature, as well as their similarities in distribution (see table 11). Main dominant species, such as Oak, *Pinus brutia*, Beech and Maquis were found quite stable for the MNF transformed CASI imagery.

Class	Objects	Mean	SD	Minimum	Maximum
Maquis	2115.00	0.20	0.25	0.00	0.96
Castanea	25.00	0.12	0.09	0.00	0.29
Beech	280.00	0.14	0.14	0.00	0.73
PinusBrutia	861.00	0.08	0.08	0.00	0.60
PinusSylvestris	206.00	0.06	0.04	0.00	0.24
PinusMaritime	490.00	0.07	0.07	0.00	0.28
PinusNigra	156.00	0.05	0.05	0.00	0.30
PinusPinea	72.00	0.30	0.13	0.01	0.42
Oak	2949.00	0.13	0.10	0.00	0.98
Other	1105.00	0.43	0.33	0.00	1.00

Table 20: Classification Stability per class for the MNF transformed CASI image after fuzzy analysis-based classification.

The Best Classification Result, as illustrated in figure 65, with values tabulated in table 21, shows excellent results, meaning the confidence for attributing each segment to a particular class is exceptionally high (almost 100%).

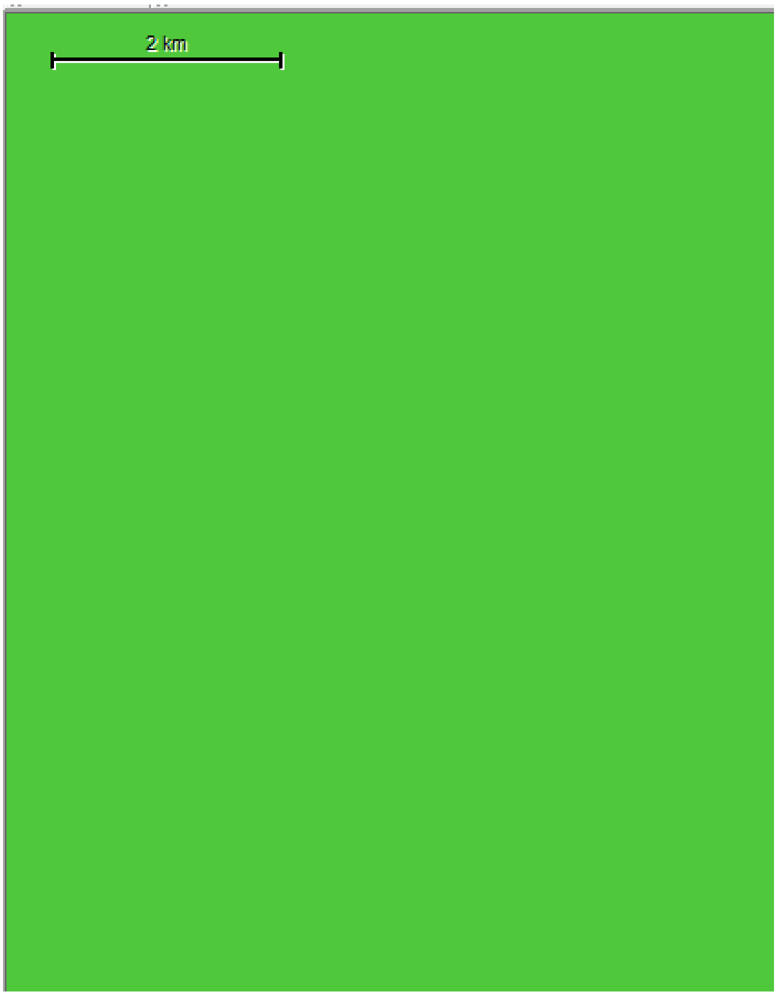

Figure 66: Best classification result for the MNF transformed CASI image after entering a fuzzy range for physiographic parameters. Red shows areas with high conflict between classes, followed by yellow and green for more stable classification results successively.

Class	Objects	Mean	SD	Minimum	Maximum
Maquis	2115.00	0.79	0.14	0.50	0.99
Castanea	25.00	0.70	0.09	0.54	0.99
Beech	280.00	0.74	0.12	0.50	0.99
PinusBrutia	861.00	0.84	0.12	0.50	1.00
PinusSylvestris	206.00	0.72	0.13	0.50	1.00
PinusMaritime	490.00	0.84	0.15	0.52	0.99
PinusNigra	156.00	0.80	0.12	0.51	0.99
PinusPinea	72.00	0.90	0.12	0.50	0.99
Oak	2949.00	0.82	0.12	0.50	1.00
Other	1105.00	0.71	0.16	0.50	1.00

Table 21: Best Classification result per class for the MNF transformed CASI image after fuzzy analysis-based classification.

3.6 Biodiversity Index

Mapping biodiversity in Taxiarchis University Forest, by calculating an index for the diversity of forest trees was the final aim of this study. Through this section, the potential of remote sensing in evaluating the quality, disturbance and possible management needs of a particular ecosystem is demonstrated. The MNF transformed CASI image with 2 m spatial resolution (Group B categories) was used in this section, due to the fact it provided the best classification accuracy results in comparison to the TTA mask.

For this part of the study we restricted our training in areas in those provided by group B categories. This is due to the high accuracy of classification they exhibited, as well as the straightforwardness in determining a spectral signature per species.

3.6.1 Simpson's Diversity Index

A level was created for the purpose of estimating the biodiversity of the area. The MNF transformed CASI image, which was selected for its excellent accuracy scores and classification stability, was segmented with multi-resolution segmentation. The level used for estimating Simpson's Diversity Index was created with scale factor 100, colour factor 0.9, compactness 1. For the segmentation only the Elevation feature of the GDEM was considered (so that this level is independent of spectral features).

The two levels, which were generated, are illustrated in figure 67, below. The biodiversity level, whose scale is double that of the tree distribution level, takes into consideration for the segmentation process only the elevation of the GDEM, so the segments are created irrespective of the forest ecosystem composition. The tree distribution level takes into consideration, as in previous projects, the 6 MNF transformed CASI (2 m spatial resolution) bands and so does the Nearest Neighbour classification process, together with brightness (bands 2-6), Standard Deviation (SD) (bands 2-6) and physiographic-parameter-based fuzzy analysis, as discussed in chapter 3.5.3. The classes are divided into two mother categories based on their Normalized Difference Vegetation Index (NDVI[9]).

---

[9] The NDVI is a simple graphical indicator that can be used to analyse remote sensing measurements and assess whether the target being observed contains live green vegetation or not. The formula used is as follows: NDVI = (NIR - Red) / (NIR + Red).

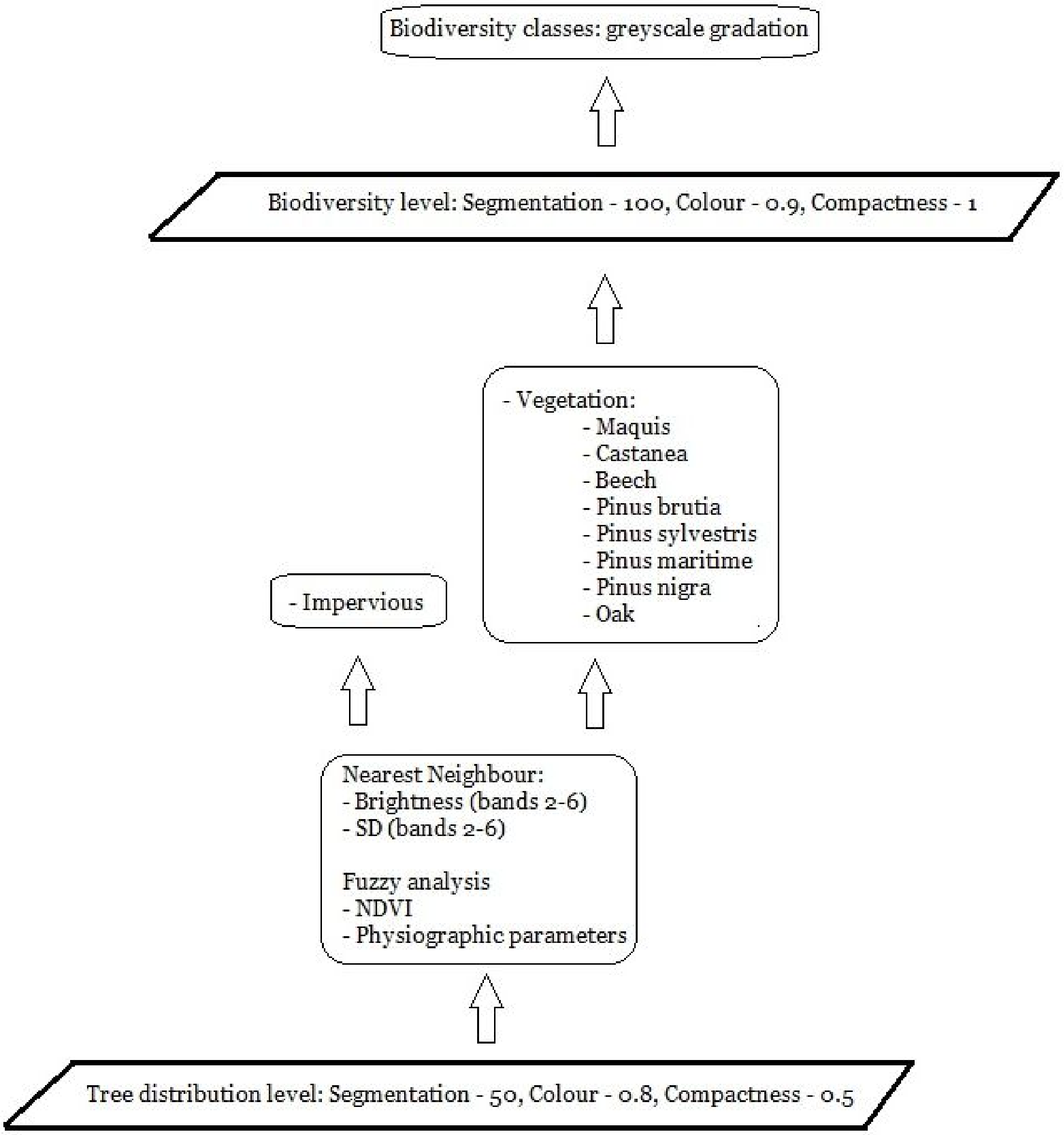

Figure 67: Illustration of the two levels used in the project for estimating Simpson's biodiversity index.

The formula index used for estimating the species richness per segment is the following:

$$D = \frac{1}{\sum_{i=1}^{S} P_i^2}$$

Where S, is the area coverage (ha) of each forest tree species (community richness) and P_i the i-th species' area cover within each segment. The value of the index depends both on the richness of the forest community, as well as the uniformity of the distribution of those species. Consequently, for a specific species richness, D increases with the uniformity of the forest community (Begon *et al.*, 1996).

Figure 68, illustrates the formula, as was entered in the eCognition Developer software, adapted appropriately. The Relative Area of each class was used, while the Relative Area of the Impervious class was subtracted, so that it is not accounted for, as it does not concern us for the calculation of this index (rocky areas may show high diversity in forest tree species, but are not likely to be uniformly distributed and thus those areas are not likely to score high in any case).

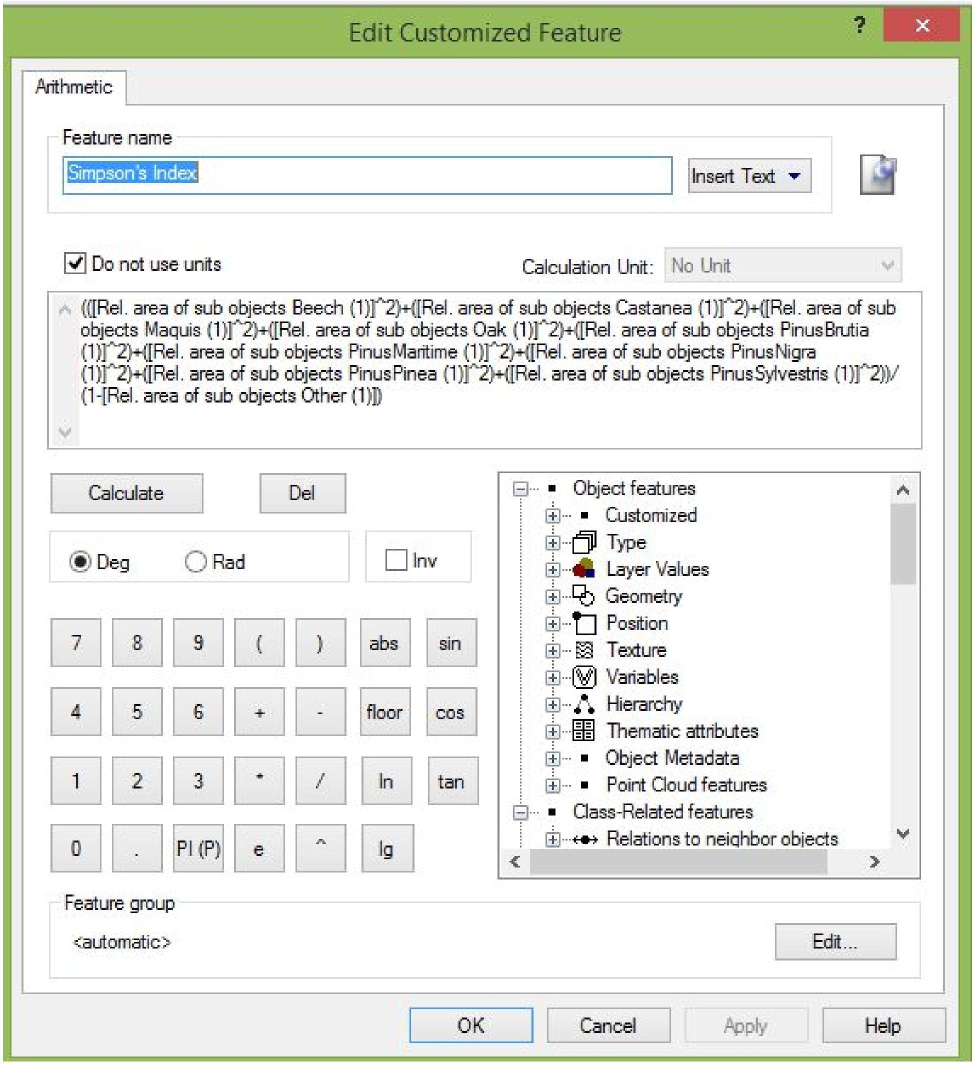

Feature name: Simpson's Index

☑ Do not use units

Calculation Unit: No Unit

```
(([Rel. area of sub objects Beech (1)]^2)+([Rel. area of sub objects Castanea (1)]^2)+([Rel. area of sub
objects Maquis (1)]^2)+([Rel. area of sub objects Oak (1)]^2)+([Rel. area of sub objects PinusBrutia
(1)]^2)+([Rel. area of sub objects PinusMaritime (1)]^2)+([Rel. area of sub objects PinusNigra
(1)]^2)+([Rel. area of sub objects PinusPinea (1)]^2)+([Rel. area of sub objects PinusSylvestris (1)]^2))/
(1-[Rel. area of sub objects Other (1)])
```

● Deg ○ Rad ☐ Inv

Feature group: <automatic>

Figure 68: Simpson's index estimation formula, as entered in the eCognition software.

In figure 69, we see the distribution of Simpson’s Diversity Index. The darker a patch is, the more biodiverse it is considered, with a vibrant and competitive community of forest trees. The darker a patch is, the less likely it is for a particular class or tree species to be dominant and thus the entire forest community is more likely to be richer on all levels of life (including living organisms such as mammals, reptiles, insects, microorganisms, fungi etc.). The implications for all forest organisms are quite significant and may lead to the identifications of patches within a forest ecosystem of particular interest for conservation and management efforts.

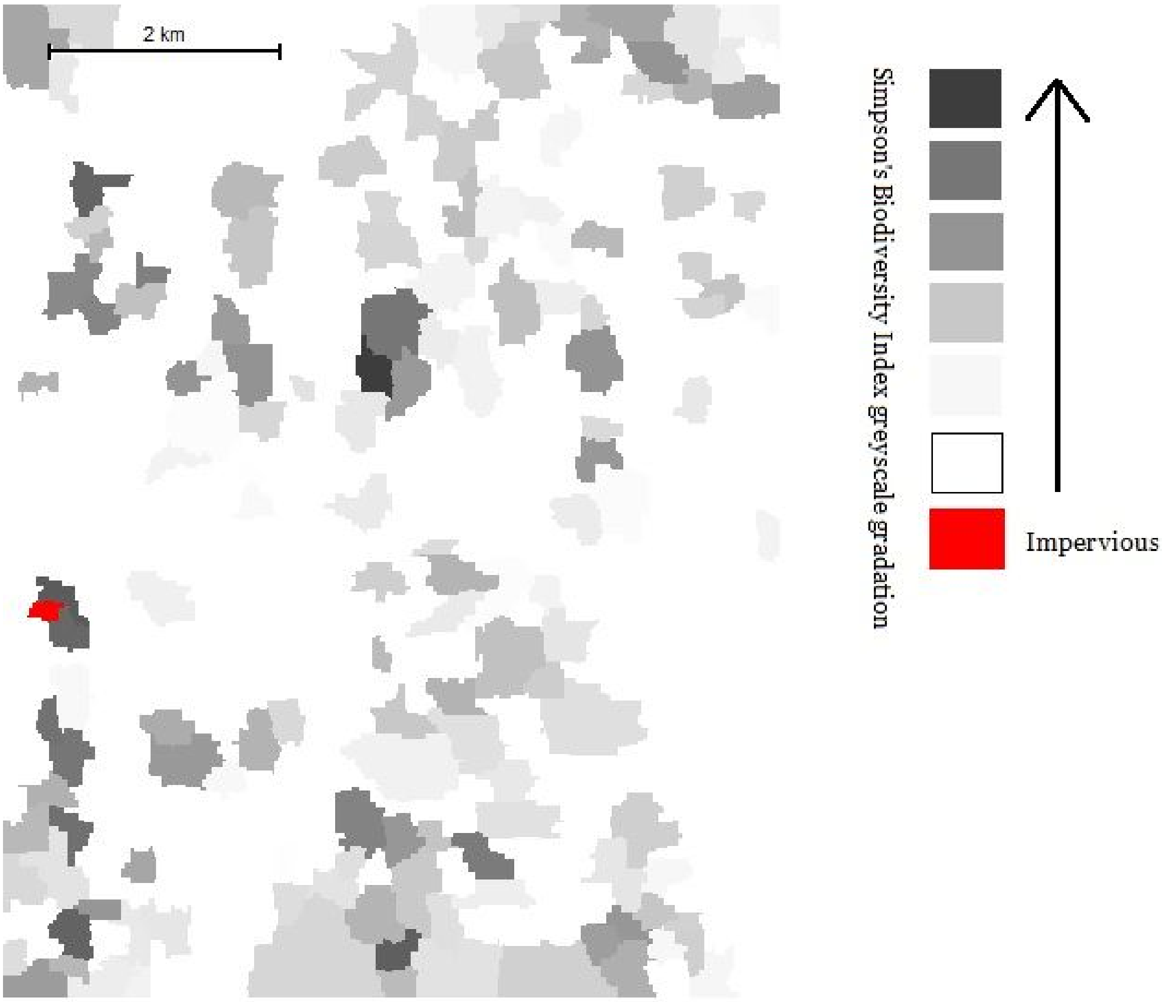

Figure 69: Simpson's diversity index. Darker areas have scored higher than more lightly coloured areas, while the red area represents a patch where the index could not be calculated due to the absence of vegetation.

Figure 70 shows Simpson's Diversity Index plotted against elevation (or height), based on the GDEM data. We see that forest tree diversity in the Taxiarchis forest is independent of elevation.

One should note that the accuracy of the biodiversity map (see figure 69) directly connected to the forest species classification accuracy.

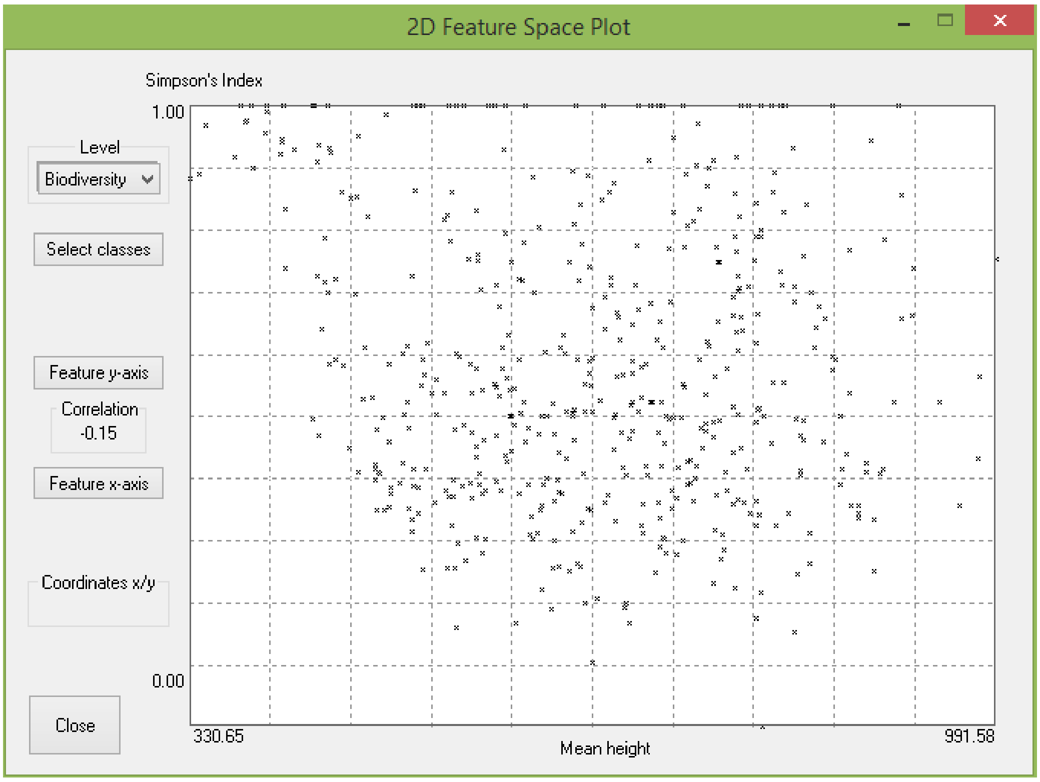

Level: Biodiversity

Correlation: -0.15

Figure 70: 2D Features space plot of elevation / height (m) against Simpson's Diversity Index.

4. Discussion

After analysing a variety of satellite and aerial imagery for Taxiarchis forest, by using the vector data, acquired from field sampling, it was possible to select the imagery providing the most accurate distribution for forest trees. Our imagery included multispectral data provided by satellites, such as Landsat and GeoEye, as well as hyperspectral data provided by Hyperion Satellite, as well as aerial CASI imagery.

The consecutive process concerned the satellite and aerially derived data, Hyperion and CASI respectively, which had their hyperspectral space reduced, using two feature extraction methods, PCA and MNF and one feature selection method based on the correlation between class spectral signatures along the spectrum. The PCA method did not give good results in comparison to other methods. Rocchini *et al.* (2007) found that generally such studies are prone to underestimation of species richness, using PCA to reduce the number of bands. The imagery providing the best classification results and accuracy, which were selected for further processing were the MNF transformed CASI imagery of 2m spatial resolution, the Landsat imagery, while the MNF transformed Hyperion imagery, which did not show especially high accuracy, was useful in comparing the results it gave with the other two. Fuzzy analysis, based on the distribution of forest tree species along on altitudinal gradient, provided by the GDEM data, helped in reducing classification conflict between categories, but not overall accuracy.

The process of creating a fuzzy spectrum for the distribution of each class in terms of elevation and slope was a process requiring time and careful observation. Despite the good quality of data available for the distribution of forest tree species along an altitudinal gradient (see tables 9 and especially 10), the results of this process were not satisfactory considering the time input required. This process could be improved by adding certain rules for the creation of a fuzzy set by systematically studying the classification accuracy responses to the different values entered and evaluated through trial-and-error.

The MNF transform allowed for an extremely useful reduction in the amount of data being processed and consequently in processing time. It also proved to be a feature extraction method, which can successfully reduce noise, without loss of useful information for the classification of forest tree species using OBIA. Especially in the case of the CASI image, an image with 72 bands, constituting a very heavy file, the MNF transform increased the usability of the imagery, giving very good results. It should be noted that the CASI imagery had various radiometric flaws and yet gave very good results. This could be attributed to the spatial resolution of the imagery.

In OBIA the spatial resolution of a particular image should be less than the diameter of the target objects, which in our case were primarily forest tree crowns and secondarily forest patches. With a spatial resolution of 2m, the CASI imagery was proven more reliable for providing a stable and confident identification of tree species, while other images, such as the Landsat gave high accuracy, but low stability and confidence in the results after the fuzzy analysis. We thus conclude that spatial resolution should be at least 2m for an effective identification of tree species and patches, when using OBIA. Indeed, ideally, the size of the pixel should be matched so that it is one quarter to one third of the size of the smallest patches of habitat, species assemblage or individual tree being mapped. Some studies exploring the use of medium-resolution (few tens of metres) and high-resolution (a few metres) satellite images for assessing plant species richness (Rocchini *et al.*, 2007) or for ecological prediction (Stickler & Southworth, 2008) found that Landsat performed better than IKONOS or QuickBird VHR satellites, across a range of measures of species richness (EEA & MNHN, 2014). The majority of studies on biodiversity focus on canopy tree species of a forested area, even though in recent years with the use of radar sensors or Lidar penetration on lower vegetative levels is feasible, as these are usually static and bulky organisms. However, various studies conclude that the distinction between tree species is particularly difficult and requires both good resolution of imaging and a suitable selection of a spectral signature area, which depends on the biochemical composition of an organism.

A major problem that was faced at various points during the process of this study involved the vector data derived from field observations. This data corresponded to a great degree to mixed categories of forest tree species. Those categories representing forest communities, often found in a particular composition in the field, lacked in that they do not carry a definite spectral signature and result in high conflict between species during classification. In a future study, it may be useful for ground data to be collected in terms of individual tree species, as opposed to tree species combinations or communities, when the study is used for remote sensing purposes. Also the already weak spectral features of tree canopies might be further attenuated by canopy voids, as well as the superposition of emitted and reflected energy components (Ribeiro da Luz & Cowley, 2010) and thus a definite spectral signature is of high importance for the systemisation of forest monitoring efforts. Spectral unmixing methods would also be an appropriate technique for the type of data included in this study and constitutes a prospect for future research, even though OBIA was found to be a well suited approach for the identification of tree objects.

Another prospect, with great promise for the continuation and improvement of the results of the present study, would be the identification of tree species' spectral signatures in the laboratory, which could later be used for the analysis of remote sensing data. This proposed methodology could also provide powerful insights on the differences and similarities between the chemical composition, reflectance and even health of the tree species. Separating species based on their spectral signatures and identifying them using the vector ground data would be the opposite approach of the one used in this study, but would be worth testing, as it could provide in-depth insights on the reflectance and absorbance differences between tree species.

The Simpson's Diversity Index estimates provided results in the form of a map, which shows patches within the Taxiarchis forest of particularly high biodiversity. Forest trees may constitute habitats for a variety of living organisms, as well as forests altogether. Harvey *et al.* (2006) related tree cover to birds, butterflies and dung beetles while Dover *et al.* (2010) examined how the structure even within a single habitat can affect butterfly abundance and Hinsley and Bellamy (2000) show how bird assemblages, even within one habitat, a hedge, are related to management. Identification and prioritisation of places meriting protection has become more systematic and scientific. Several organizations (e.g., Conservation International, the World Wildlife Fund) have targeted places for global protection based upon the biodiversity they contain—so-called "hotspots" of species richness (Myers *et al.*, 2000).

Biodiversity usually takes into consideration the rate of occurrence or the abundance of a species or of another ecological entity, along with the multitude of species within the sample. Biodiversity indices, such as the Shannon & Weaver and the Simpson Diversity Index combine species richness with a measure of the degree of heterogeneity in their distribution. When a natural landscape is fragmented, for example, the total biodiversity of a community may remain on the same levels or may increase, even though the integrity of the community may have been compromised due to the intrusion of alien-species, dislocating for example species which previously existed there. As an area gradually loses its character, global biodiversity is reduced (Noss, 1990). Thus the full interpretation of the biodiversity results give some preliminary conclusions related to the distribution of biodiversity in Taxiarchis forest, but should also be followed for management purposes by a field study.

Considering the importance attributed to biodiversity, in terms of EU policy and legislation, as a criterion for ecosystem conservation, the implications of using remote sensing to identify patches of high biodiversity is of particular interest, because this could concern extremely large areas of forest or even other types of ecosystems. In patches or areas where high biodiversity is observed, conservation efforts could be intensified and more focused, ultimately providing protection for an entire ecosystem. In addition, buffer zones could be planned around areas considered ecologically valuable and of high biodiversity by using these remote sensing tools. For example, the EU INSPIRE Directive, which aims to allow for the combination of spatial data and services from different sources across Europe in a consistent way, proposes that the EUNIS habitat classification be used as a common reference for habitats (EEA & MNHN, 2014).

Remote sensing observations can complement and add to field observations as they deliver a synoptic view and offer the opportunity to provide consistent information in time and space (Nagendra, 2001; Nagendra & Rocchini, 2008; Vanden Borre *et al.*, 2011). It is a field that could assist greatly in conservation and monitoring efforts. However, existing remote sensing data are of limited coverage is still limited and this is an issue that should be addressed on a policy lever provided that remote sensing can play such a valuable role, as demonstrated by the present study.

Habitat records can be linked to changes over time at the landscape level and to vegetation assemblages. Protocols are available and can be used to link extant habitat data across Europe (Bunce *et al.*, 2013). A prospect opened by studies such as this involve the development of a methodology protocol building on existing information concerning the spectral behaviour of forest trees, as well as other ecosystem types. In our study such a protocol was partially developed, as discussed previously and concerns a process of determining the best accuracy for the existing remote sensing data, reducing bands through band extraction and selection methods, with the MNF method, as well as the Spectral-Signature-Correlation method showing the most promise and applying fuzzy analysis for the identification of tree species.

In most cases, the accuracy of classification, which is achieved for the identification of tree species using remote sensing data, varies between 50% and 90% and thus our results are considered to have achieved a good level of accuracy. However, our results would have been significantly improved if the CASI imagery lacked the serious radiometric and geometric defects that it carried. Thus this study may be used as a starting point for adding to the sophistication and amelioration of the methods described here.

5. Conclusion

After analysing a variety of satellite and aerial imagery for Taxiarchis forest, by using the vector data, acquired from field sampling, it was possible to select the imagery providing the most accurate distribution for forest trees for further analysis. Our imagery included multispectral data provided by satellites, such as Landsat and GeoEye, as well as hyperspectral data provided by Hyperion Satellite, as well as aerial CASI hyperspectral imagery.

The images providing the best classification results and accuracy, which were selected for further processing were the MNF transformed CASI imagery of 2m spatial resolution, the Landsat imagery, while the MNF transformed Hyperion imagery, which did not show especially high accuracy, was useful in comparing the results it gave with the other two. Fuzzy analysis, based on the distribution of forest tree species along on altitudinal gradient, provided by the GDEM data, helped in reducing classification conflict between categories, but not overall accuracy. The process of creating a fuzzy spectrum for the distribution of each class in terms of elevation and slope was a process requiring time and careful observation. The MNF transform allowed for an extremely useful reduction in the amount of data being processed and consequently in processing time. It also proved to be a band extraction method, which can successfully reduce noise, without loss of useful information for the classification of forest tree species using OBIA. Especially in the case of the CASI image, with 72 bands, constituting a very heavy file, the MNF transform increased the usability of the imagery, giving very good results. With a spatial resolution of 2m, the CASI imagery was proven more reliable for providing a stable identification of tree species, while other images, such as the Landsat gave high accuracy, but low stability in the results after the fuzzy analysis. We thus conclude that spatial resolution should be at least 2m for an effective identification of tree species and patches, when using OBIA. In a future study, it may be useful for ground data to be collected in terms of individual tree species, as opposed to tree species combinations or communities, when the study is used for remote sensing purposes. In addition, a newly launched satellite, The ESA-developed Sentinel satellite – Sentinel-2A, providing data for land monitoring services and designed to be the base for a wide spectrum of applications reaching from agriculture to forestry, environmental monitoring to urban planning, could also provide imagery complementing the range of imagery used in this study.

Simpson’s Diversity Index provided results in the form of a map, which shows patches within the Taxiarchis forest of particularly high biodiversity. Forest trees may constitute habitats for a variety of living organisms, as well as forests altogether.

Considering the importance attributed to biodiversity, in terms of EU policy and legislation, as a criterion for ecosystem conservation, the implications of using remote sensing to identify patches of high biodiversity is useful, because this could concern extremely large areas of forest or even other types of ecosystems. In patches or areas where high biodiversity is observed, conservation efforts could be intensified and more focused, ultimately providing protection for an entire ecosystem. In addition, buffer zones could be planned around areas considered ecologically valuable and of high biodiversity by using these remote sensing tools.

Acknowledgements

I would like to thank everyone who works and studies in the Remote Sensing Laboratory and the Interdisciplinary Postgraduate Program “Environment and Development” (year 2014-2015), School of Rural and Surveying Engineering, NTUA, for their valuable help, constant input, profound support and opportunity they gave me to be part of a community with dedication to education, science and development. I am especially grateful to Dr. Pol Kolokoussis for his tireless support, kindness and guidance in every aspect of this thesis and Prof. Demetre Argialas for his valuable support and careful comments. I would also like to thank Ilias Papagiannopoulos, Dr. Vassilis Andronis and Dr. Kostas Vamvoukakis for the enjoyable conversations, thoughts and ideas we shared and have contributed to the process of this study. I would like to thank Emeritus Prof. Dimitris Rokos for his support and profound influence in my approach to science and philosophy. Last, but not least, I would like to thank Antonina Papathanasoglou, Mrs. Milli Vasili-Vasiliou, Ass. Prof. Efi Dimopoulou & Ass. Prof. Vassilia Karathanasi for being an inspiration for the role they play as women scientists in a Greek University.

References

Agathagelou, M. (2008). Διπλωματική Εργασία: Σύγκριση παραδοσιακών και αντικειμενοστραφών τεχνικών τηλεπισκόπησης, κάλυψης – χρήσης γης από τηλεπισκοπικά δεδομένα QUICKBIRD στην επαρχία Πάφου. Επιβλέπων: Δ. Αργιαλάς. Σχολή Αγρονόμων και Τοπογράφων Μηχανικών. Τομέας Τοπογραφίας – Εργαστήριο Τηλεπισκόπησης.

Angelini, P., Bianco, P. M., Cardillo, A., Francescato, C., & Oriolo, G. (2009). Gli habitat in Carta della Natura. Schede descrittive degli habitat per la cartografia alla scala 1:50.000, Manuali e Linee Guida 49/2009. Rome, ISPRA *in* EEA & MNHN (2014).

Argialas, D.P. (2000). Φωτοερμηνεία – Τηλεπισκόπηση. Εθνικό Μετσόβιο Πολυτεχνείο, Τμήμα Αγρονόμων Τοπογράφων Μηχ., Τομέας Τοπογραφίας, Εργαστήριο Τηλεπισκόπησης. Αθήνα.

Aristotle University of Thessaloniki (2013). Διαχειριστικό σχέδιο Πανεπιστημιακού Δάσους Ταξιάρχη – Βαστάμων 2012-2021. Διοίκηση Δάσους Ταξιάρχη-Βαστάμων.

Aristotle University of Thessaloniki (2014). http://www.auth.gr/en/units/8164

ASTER GDEM (2011). ASTER Global Digital Elevation Model. http://www.jspacesystems.or.jp/ersdac/GDEM/E/4.html

Baatz, M. & Schaepe, A. (1999). Object-oriented and multiscale image analysis in semantic networks. 2nd International Symposium: Operationalization of Remote Sensing, 16-20 August, ITC, the Netherlands.

Begon M., C.R. Townsend & J.L. Harper (1996). Ecology: From Individuals to Ecosystems. Wiley. Blaschke, T. (2010). Object based image analysis for remote sensing. ISPRS Journal of Photogrammetry and Remote Sensing 65: 2–16.

Blaschke, T. (2010). Object based image analysis for remote sensing. ISPRS Journal of Photogrammetry and Remote Sensing 65: 2–16.

Bohn, U., Neuhäusl, R., Gollub, G., Hettwer, C., Neuhäuslová, Z., & Weber, H. E. (2000–2003). Karte der natürlichen Vegetation Europas — Maßstab 1: 2.500.000. Teil 1: Erläuterungstext mit CD-Rom; Teil 2: Legende; Teil 3: Karten. U. Bohn & R. Neuhäusl, Eds., Münster, Bundesamt für Naturschutz, Landwirtschaftsverlag *in* EEA & MNHN (2014).

Braun-Blanquet, J. (1928). Pflanzensoziologie. Grundzüge der Vegetationskunde, 1st ed., pp. 1–330. Berlin, Springer Verlag.Braun-Blanquet *in* EEA & MNHN (2014).

Bunce, R. G. H., Metzger, M. J., Jongman, R. H. G., Brandt, J., Blust, G., De Elena-Rossello, R., Groom, G. B., Halada, L., Hofer, G., Howard, D.C., Kovar, P., Mucher, C.A., Padoa-Schioppa, E., Paelinx, D., Palo, A., Perez-Soba, M., Ramos, I.L., Roche, P., Skones, H. & Wrbka, T. (2008). A standardized procedure for surveillance and monitoring European habitats and provision of spatial data. Landscape Ecology 23: 11–25.

Bunce, R. G. H., Bogers, M. M. B., Evans, D., Halada, L., Jongman, R. H. G., Mücher, C. A., Bauch, B., de Blust, G., Parr, T. W. & Olsvig- Whittaker, L. (2013). The significance of habitats as indicators of biodiversity and their links to species. Ecological Indicators 33: 19–25.

Burnett, C. & T. Blaschke (2003). A multi-scale segmentation/object relationship modeling methodology for landscape analysis. Ecological Modeling 168: 233-249.

Calow, P.P. (1999). Blackwell's Concise Encyclopedia of Environmental Management. Blackwell Science Ltd., UK.

Carreiras, J.M.B, J.M.C. Pereira & J.S. Pereira (2006). Estimation of tree canopy cover in evergreen oak woodlands using remote sensing. Forest Ecology and Management 223: 45–53.

Chang, C.-I. (2003). Hyperspectral Imaging: Techniques for Spectral Detection and Classification. Kluwer Academic/Plenum Publishers, New York.

Chuvieco, E. & Congalton, R.G. (1988). Application of Remote Sensing and Geographic Information Systems to Forest Fire Hazard Mapping. Remote Sensing of the Environment 29: 147-159.

Cochrane, M.A. (2000). Using vegetation reflectance variability for species level classification of hyperspectral data. International Journal of Remote Sensing 21: 2075-2087.

Council of Europe (2014).
http://www.coe.int/t/dg4/cultureheritage/nature/econetworks/default_en.asp

Coombes, A.J. (2992). Trees. Dorling Kindersley Handbooks, London.

Congalton, R.G. (1991). A review of assessing the accuracy of classification of remotely sensed data. Remote Sensing of Environment 37:35-46.

Danson, F.M. & Plummer, S.E. (1995). Red-edge response to leaf area index. International Journal of Remote Sensing 16: 183-188.

Davies, C. E., Moss, D., & Hill, M. O. (2004). EUNIS habitat classification revised 2004. European Environment Agency — European Topic Centre on Nature Protection and Biodiversity.

De Fries, R.S., M.C. Hansen, J.R.G. Townshend, A.C. Janetos & T.R. Loveland (2000). A new global 1-km dataset of percentage tree cover derived from remote sensing. Global Change Biology 6: 247-254.

De Fries, R.S., M.C. Hansen, J.R.G. Townshend & R. Sohlberg (1998). Global land cover classifications at 8 km spatial resolution: The use of training data derived from Landsat imagery in decision tree classifiers. International Journal of Remote Sensing, 19: 3141-3168.

Dennis, R.L.H. & T.G. Shreeve (1996). Butterflies on British and Irish offshore islands. Gem Publisching Company.

Devillers, P., Devillers-Terschuren J. & Ledant J-P. (1991). Corine biotopes manual. Vol. 2. Habitats of the European Community, Office for Official Publications of the European Communities, Luxembourg.

Devilliers, P., & Devilliers-Terschuren, J. (1996). A classification of Palaearctic habitats, Nature and environment 78: 194.

Dimopoulos, P., I. Tsiripidis, E. Bergmeier, G. Fotiadis, K. Theodoropoulos, T. Raus, M. Panitsa, A.S. Kallimanis, K.V. Sýkora7, L. Mucina (2012). Towards the Hellenic National Vegetation Database: VegHellas. Plant Sociology 49 (No. 2): 81-87.

Dover, J. W., A. Rescia, S. Fungarino, J. Fairburn, P. Carey, P. Lunt, R. L. H. Dennis, C. J. Dover (2010). Can hay harvesting detrimentally affect adult butterfly abundance? Journal of Insect Conservation 14:413–418.

EBONE – European Biodiversity Observation Network (2015). http://www.wageningenur.nl/en/Expertise-Services/Research-Institutes/alterra/Projects/EBONE-2.htm

eCognition. Technical Commission VII Symposium 2010. In: Wagner W., Székely, B. (eds.): ISPRS TC VII Symposium – 100 Years ISPRS, Vienna, Austria, July 5–7, 2010, IAPRS, Vol. XXXVIII, Part 7B.
http://www.isprs.org/proceedings/Xxxviii/part7/b/pdf/690_XXXVIII-part7B.pdf

eCognition Definiens Developer 7 Userguide (2007).
http://ecognition.cc/download/userguide.pdf

European Commission (2007). Interpretation Manual of the European Union Habitats. European Commission.
http://ec.europa.eu/environment/nature/legislation/habitatsdirective/docs/2007_07_im.pdf

European Commission (2013). Interpretation Manual of European Union Habitats — EUR28. Brussels, European Commission, DG Environment, Brussels, http://ec.europa.eu/environment/nature/legislation/habitatsdirective/docs/Int_Manual_EU28.pdf.

European Commission (1992). Council Directive 92/43/EEC of 21 May 1992 on the conservation of natural habitats and of wild fauna and flora. Official Journal of European Committee L 206: 7–50.

European Environmental Agency (2014). http://www.eea.europa.eu/
European Vegetation Archive (EVA) (2015). http://euroveg.org/eva-database

Evans, D. (2006). The habitats of the European Union habitats directive, Biology & Environment: Proceedings of the Royal Irish Academy, 106(3), 167–173.Fisher *et al.* (2009) Franklin, J., 1995, Predictive vegetation mapping: geographic modelling of biospatial patterns in relation to environmental gradients, *Progress in Physical Geography*, *19*(4), 474–499.

EU INSPIRE Directive (Directive 2007/2/EC).
http://inspire.ec.europa.eu/

Filotis Database for Greek Nature (2015).
http://filotis.itia.ntua.gr/species/?species_category=4

Franklin, S. E., D.R. Connery, & J.A. Williams (1994). Classification of Alpine vegetation using Landsat Thematic Mapper, SPOT HRV and DEM data. Canadian Journal of Remote Sensing 20: 49–60.

Fuller, R.M., G.B. Groom, S. Mugisha, P. Ipulet, D. Pomeroy, A. Katende, R. Bailey & R. Ogutu-Ohwayo (1998). The integration of field survey and remote sensing for biodiversity assessment: a case study in the tropical forests and wetlands of Sango Bay, Uganda. Biological Conservation 86: 379-391.

Gao, Y., J.F. Mas, I. Niemeyer, P.R. Marpu & J.R. Palacio (2007). Object-based image analysis for mapping land-cover in a forest area.
http://www.itc.nl/issdq2007/proceedings/Postersession/gao,%20mas,%20marpu%20et%20al..pdf

Geijzendorffer, I. R., & P. K. Roche (2013). Can monitoring schemes provide indicators for ecosystem services? Ecological Indicators 33: 148-157

General Habitat Categories (GHCs).
http://www.wageningenur.nl/en/Expertise-Services/Research-Institutes/alterra/Projects/EBONE-2/Products/General-Habitat-Categories.htm

GEO BON (2011).
http://geobon.org/

Gonzalez, R. & Woods, R. (1993). Digital image processing. Reading, Massachusetts, Addison-Wesley Publishing Company, pp.148-56.

Gould, W. (2000). Remote sensing of vegetation, plant species richness and regional biodiversity. Ecological Applications, 10 (No.6): 1861–1870

Green A. A., Berman M., Switzer P. & Craig, M.D. (1988). A transformation for ordering multispectral data in terms of image quality with implications for noise removal. IEEE Transactions in Geoscience and Remote Sensing 26(1): 65–74.

Groves, C. & The Nature Conservancy (2003). Drafting a Conservation Blueprint: A practicioner's guide to planning for biodiversity. Island Press, Washington, DC.

Harvey, C.A., A. Medina, D.M. Sanchez, S. Vilchez, B. Hernandez, J.C. Saenz, J.M. Maes, F. Casanoves & F.L. Sinclair (2006). Patterns of animal diversity in different forms of tree cover in agricultural landscapes. Ecological Applications, 16(5): 1986–1999.

Haslett, J.R., P.M. Berry, G. Bela, R.H.G. Jongman, G. Pataki, M.J. Samways & M. Zobel (2010). Changing conservation strategies in Europe: a framework integrating ecosystem services and dynamics. Biodiversity Conservation 19:2963–2977.

Hearn, S. M., Healey, J. R., McDonald, M. A., Turner, A. J., Wong, J. L. G., & Stewart, G. B., 2011, The repeatability of vegetation classification and mapping, *Journal of environmental management*, 92(4), 1 174–1 184.

Hestir, E.L., S. Khanna, M.E. Andrew, M.J. Santos, J.H. Viers, J.A. Greenberg, S.S. Rajapakse & S.L. Ustin (2008). Identification of invasive vegetation using hyperspectral remote sensing in the California Delta ecosystem. Remote Sensing of Environment 112: 4034–4047.

Hinsley, S.A. & P.E. Bellamy (2000). The influence of hedge structure, management and landscape context on the value of hedgerows to birds: A review. Journal of Environmental Management 60: 33–49.

Hofmann, P. (2001). Detecting Urban Features from IKONOS Data using an Object-Oriented Approach. Proceedings of the First Annual Conference of the Remote Sensing & Photogrammetry Society. RSPS, Munich, Germany, 12-14 September 2001, 79-91.

Hufkens, K., G. Thoonen, J. Vanden Borre, P. Scheunders, R. Ceulemans (2010). Habitat reporting of a heathland site: Classification probabilities as additional information, a case study. Ecological Informatics 5: 248–255.

Innes, J.L. & B. Koch (1998). Forest biodiversity and its assessment by remote sensing. Global Ecology and Biogeography Letters 7: 397–419

James B. L., Woodyatt A. S., Berman M. (1990). Enhancement of high spectral resolution remote-sensing data by a noise-adjusted principal components transform. IEEE Transactions in Geoscience and Remote Sensing 28(3): 295–304.

Jones, K.B. & B.R. Riddle (1996). Regional scale monitoring of biodiversity. Biodiversity in managed landscapes: theory and practice. R.C. Szaro & D.W. Johnston. Oxford University Press, New York.

Karathanassi, V., P. Kolokoussis & S. Ioannidou (2007). A comparison study on fusion methods using evaluation indicators. International Journal of Remote Sensing 28 (10): 2309 - 2341

Kent, M. (2012) Vegetation description and data analysis: a practical approach. Wiley-Blackwell, Chichester.

Kolokoussis, P. (2008). “Development of an Integrated System of Hyperspectral and Thermal Remote Sensing Sensors for the Detection of Coastal and Submarine Springs”. Doctorate thesis. Remote Sensing Laboratory, School of Rural and Surveying Engineering, NTUA.

Layke, C., A. Mapendembe, C. Brown, M. Walpole & J. Winn (2012). Indicators from the global and sub-global Millennium Ecosystem Assessments: An analysis and next steps. Ecological Indicators 17: 77–87.

Lengyel, S., E. Déri, Z. Varga, R. Horváth, B. Tóthmérész, P.-Y. Henry, A. Kobler, L. Kutnar, V. Babij, A. Selinkar, C. Christia, E. Papastergiadou, B. Grube & K. Henle (2008). Habitat monitoring in Europe: a description of current practices. Biodiversity and Conservation 17: 327–339.

Machala, M. & L. Zejdová (2014). Forest Mapping Through Object-based Image Analysis of Multispectral and LiDAR Aerial Data. European Journal of Remote Sensing 47: 117-131.

McRoberts, R. E., D.G. Wendt, M.D. Nelson, & M.H. Hansen (2002). Using a land cover classification based on satellite imagery to improve the precision of forest inventory area estimates. Remote Sensing of Environment 81(1): 36–44.

Mallinis, G., G. Galidaki & I. Gitas (2014). A comparative analysis of EO-1 Hyperion, Quickbird and Landsat TM imagery for fuel type mapping of a typical Mediterranean landscape. Remote Sens. 6: 1684–1704.

Mallinis, G., N. Koutsias, M. Tsakiri-Strati & M. Karteris (2008). Object-based classification using Quickbird imagery for delineating forest vegetation polygons in a Mediterranean test site. ISPRS J. Photogramm. Remote Sens. 63: 237–250.

Mickelson, J.G., D.L. Civco & J.A. Silander (1998). Delineating Forest Canopy Species in the Northeastern United States Using Multi-Temporal TM Imagery. Photogrammetric Engineering & Remote Sensing 64 (9): 891-904.

Mitri, G.H. & Gitas, I.Z. (2004). A semi-automated object-oriented model for burned area mapping in the Mediterranean region using Landsat-TM imagery. International Journal of Wildland Fire 13: 367–376.

Myers, N., R.A. Mittermeier, C.G. Mittermeier, G.A.B. da Fonseca & J. Kent (2000). Biodiversity hotspots for conservation priorities. Nature 403: 853-858.

Mücher, C. A., S.M. Hennekens, R.G.H. Bunce, J.H.J. Schaminée, & M.E. Schaepman (2009). Modelling the spatial distribution of Natura 2000 habitats across Europe. Landscape and Urban Planning 92 (2): 148–159.

Mücher C.A., L. Kooistra, M. Vermeulen, J. Vanden Borre, B. Haest & R. Haveman (2013). Quantifying structure of Natura 2000 heathland habitats using spectral mixture analysis and segmentation techniques on hyperspectral imagery. Ecological Indicators 33: 71–81.

Nagendra, H. (2001). Using remote sensing to assess biodiversity – Review Article. International Journal of Remote Sensing 22 (No. 12): 2377–2400.

Nagendra, H. & D. Rocchini (2008). High resolution satellite imagery for tropical biodiversity studies: the devil is in the detail. Biodiversity Conservation 17: 3431-3442.

NASA (2013). Compact Airborne Spectrographic Imager (CASI). http://geo.arc.nasa.gov/sge/jskiles/top-down/OTTER/OTTER_docs/CASI.html
National Park Sutjeska (2015).
http://sutjeska.design21th.com/stranica.php?id=12&naziv=flora&jez=en

Noirfalise, A. (1987). Map of the natural vegetation of the member countries of the European Community and the Council of Europe, Luxembourg, Office for Official Publications of the European Community *in* EEA & MNHN, 2014.

Noss, R.F. (1990). Indicators for Monitoring Biodiversity: A Hierarchical Approach. Conservation Biology Volume 4 (No. 4): 335-364.
NVC (National Vegetation Classification) http://jncc.defra.gov.uk/page-4259

Odum, E.P. (1963). Ecology. Holt, Rinehart and Winston.

Petit, S. & M.B. Usher (1998). Biodiversity in agricultural landscapes: the ground beetle communities of woody uncultivated habitats. Biodiversity and Conservation 7: 1549-1561.

Plant sociology – South Europe. http://www.scienzadellavegetazione.it/sisv/rivista/articoloCerca.do?idRivista=68&compatto

Plaza, A., P. Martinez, J. Plaza & R. Perez (2005). Dimensionality Reduction and Classification of Hyperspectral Image Data Using Sequences of Extended Morphological Transformations. IEEE Transactions on Geoscience and Remote Sensing 43 (3): 466-479.

Portigal, F., R. Holasek, G. Mooradian, P. Owensby, M. Dicksion, M. Fene, M. Elliot, E. Hall & D. Driggett (1997). Vegetation classification using red-edge first derivative and green peak statistical moment indices with the Advanced Airborne Hyperspectral Imaging System (AAHIS). Third International Airborne Remote Sensing Conference and Exhibition, Copenhagen, Denmark, 7–10 July 1997: 789–797.

Price, J.C. (1994). How unique are spectral signatures? Remote Sensing of Environment 49: 181–186.

Raven, H. & E.O. Wilson (1992). A Fifty-Year Plan for Biodiversity Surveys. Science 258: 1099-1100.

Ribeiro Da Luz, B., & J.K. Crowley (2010). Identification of plant species by using high spatial and spectral resolution thermal infrared (8.0 –13.5 μm) imagery. Remote Sensing of Environment, 114(2): 404–413.

Roberts D.A., M. Gardner, R. Church, S. Ustin, G. Scheer, & R.O. Green (1998). Mapping Chaparral in the Santa Monica Mountains Using Multiple Endmember Spectral Mixture Models. Remote Sens. Environ. 65: 267–279.

Rocchini, D., C. Ricotta & A. Chiarucci (2007). Using satellite imagery to assess plant species richness: The role of multispectral systems. Applied Vegetation Science 10: 325-331.

Rodarmel, C. & J. Shan (2002). Principal Component Analysis for Hyperspectral Image Classification. Surveying and Land Information Systems 62 (No. 2) 2002: 115-123.

Rokos, D.S. Theocharopoulos & G.Halaris (1992). Geographic Context of Typical Mediterranean Crops and Vegetation Types as a Basis for Image Analysis Expert System Rules. European programme, contract No 4569-91-12 ED ISP GR, EEC-NTUA. Funded by the European Economic Community (EEC), Joint Research Centre (JRC), Institute for Remote Sensing Applications, Ispra, Italy.

Rosso, P.H., S.L. Ustin & A. Hastings (2005). Mapping marshland vegetation of San Francisco Bay, California, using hyperspectral data. International Journal of Remote Sensing 26(23): 5169-5191.

Satellite Imaging Corporation (2014). GeoEye-1 Satellite Sensor.
http://www.satimagingcorp.com/satellite-sensors/geoeye-1/

Savitzky–Golay filter.
http://en.wikipedia.org/wiki/Savitzky%E2%80%93Golay_filter
http://www.mdpi.com/2072-4292/4/6/1781

Schaminée, J. H. J., S.M. Hennekens & J.S. Rodwell (2009). Vegetation-plot data and databases in Europe: an overview. Preslia 81: 173–185.

Schmithüsen, J. (1948). 'Fliesengefüge der Landschaft' und 'Ökotop': Vorschläge zur begrifflichen Ordnung und Nomenklatur in der Landschaftsforschung. Berichte zur Deutschen Landeskunde 5: 74–83 *in* EEA & MNHN, 2014.

Schmidtlein, S., P. Zimmermann, R. Schüpferling & C. Weiß (2007). Mapping the floristic continuum: Ordination space position estimated from imaging spectroscopy. Journal of Vegetation Science 18: 131-140.

Schowengerdt, R.A. (1997). Remote Sensing: Models and methods for image processing, 2nd edn. Academic Press.

Shackelford A. K. & Davis C. H. (2003). A combined fuzzy pixel-based and object-based approach for classification of high-resolution multispectral data over urban areas. IEEE Transactions on Geoscience and Remote Sensing 41: 2354-2364.

Stickler, C. M., & J. Southworth, J. (2008). Application of multi-scale spatial and spectral analysis for predicting primate occurrence and habitat associations in Kibale National Park, Uganda. Remote Sensing of Environment 112(no.5): 170–2 186.

Ståhl, G., A. Allard, P. Esseen, A. Glimskär, A. Ringvall, J. Svensson, S. Sundquist, P. Christensen, Å. Gallegos Torell, M. Högström, K. Lagerqvist, L. Marklund, B. Nilsson & O. Inghe (2011). National Inventory of Landscapes in Sweden (NILS)—scope, design, and experiences from establishing a multiscale biodiversity monitoring system. Environmental Monitoring Assessment 173:579–595

Townshend, J., C. Justice, W. Li & J. McManus (1991). Global Land Cover Classification by Remote Sensing: Present Capabilities and Future Possibilities. Remote Sens. Environ. 35: 243-255.

Tucker, C. J., & M.W. Garrett (1977). Leaf optical system modeled as a stochastic process. Applied Optics 16: 1151–1157.

Turner, W., S. Spector, N. Gardiner, M. Fladeland, E. Sterling & M. Steininger (2003). Remote sensing for biodiversity science and conservation. Trends in Ecology and Evolution 18 (No.6): 306-314.

Tüxen, R. (1979). Sigmeten und Geosigmeten, ihre Ordnung und ihre Bedeutung für Wissenschaft, Naturschutz und Planung, Biogeographica 16: 79–92 *in* EEA & MNHN, 2014.

UN Forest and Agriculture Organisation (FAO) (2014).
http://www.fao.org/forestry/fra/remotesensingsurvey/en/

US Geological Survey (USGS) (2011). Sensors – Hyperion.
http://eo1.usgs.gov/sensors/hyperion

US Geological Survey (USGS) (2014). Landsat Missions – Landsat 8.
landsat.usgs.gov/landsat8.php

USGS – U.S. Geological Survey (2011). Sensors – Hyperion.
http://eo1.usgs.gov/sensors/hyperion

Vanden Borre, J., D. Paelinckx, C.A. Mücher, L. Kooistra, B. Haest, G. De Blust & A.M. Schmidt (2011). Integrating remote sensing in Natura 2000 habitat monitoring: Prospects on the way forward. Journal for Nature Conservation 19(no.2): 116–125.

Weber, H. E., J. Moravec & J.-P. Theurillat (2000). International Code of Phytosociological Nomenclature. 3rd edition. Journal of Vegetation Science: 739–768.

Wiens J., R. Sutter, M. Anderson, J. Blanchard, A. Barnett, N. Aguilar-Amuchastegui, C. Avery & S. Laine (2009). Selecting and conserving lands for biodiversity: The role of remote sensing. Remote Sensing of Environment 113: 1370–1381.

Wikipedia (2015).
https://en.wikipedia.org/wiki/Scots_pine
https://en.wikipedia.org/wiki/Acer_platanoides
https://en.wikipedia.org/wiki/Castanea_sativa
http://commons.wikimedia.org/wiki/File:Pinus_radiata_Montjuic.JPG

Wilson, E.O. (1988). Resolutions for the 80s. Harvard Magazine 82(3): 617-618.

Wilson, E.O. (2003) The Encyclopedia of Life. TRENDS in Ecology and Evolution 18 (No.2): 77-80.

Woodcock, C.E. & Strahler, A.H. (1987). The Factor of Scale in Remote Sensing. Remote Sensing of Environment 21: 311-332.

Xiang, L., Bing, Z., LianRu, G. & DongMei, C. (2009). A maximum noise fraction transform with improved noise estimation for hyperspectral images. Sci China Ser F-Inf Sci 52(9): 1578–1587.

Zhang, Y., Maxwell, T., Tong, H. & Dey, V. (2010). Development of a supervised software tool for automated determination of optimal segmentation parameters for eCognition. Wagner W., Székely, B. (eds.): ISPRS TC VII Symposium – 100 Years ISPRS, Vienna, Austria, July 5–7, 2010, IAPRS, Vol. XXXVIII, Part 7B.

Appendix I: Landsat 8 receptors and bands for data collection

Bands	**Name**	**Spectral range (µm)**	**Spatial resolution (m)**
Operational Land Imager (OLI)			
Band 1	Coastal Aerosol	0.43 – 0.45	30
Band 2	Blue	0.45 – 0.51	30
Band 3	Green	0.53 – 0.59	30
Band 4	Red	0.64 – 0.67	30
Band 5	Near-Infrared (NIR)	0.85 – 0.88	30
Band 6	Shortwave Infrared (SWIR) 1	1.57 – 1.65	30
Band 7	Shortwave Infrared (SWIR) 2	2.11 – 2.29	30
Band 8	Panchromatic (PAN)	0.50 – 0.68	15
Band 9	Cirrus	1.36 – 1.38	30
Thermal Infrared Sensor (TIRS)			
Band 11	Thermal Infrared (TIR) 1	10.6 – 11.19	100
Band 12	Thermal Infrared (TIR) 2	11.5 – 12.51	100

Table 22: Spectral bands for Landsat 8 and their spatial resolution.

Appendix II: Hyperion Layer Mixing

Band no	HYPERION Spectral Coverage						
	ALI Band Comparison		Hyperion Band	Average Wavelength (nm)	Full Width at Half the Maximum FWHM (nm)	Spatial Resolution (m)	Not Calibrated (x)
	MS	Pan (nm) 480 - 690 (X)					
1			B8	426.8200	11.3871	30	X
2	MS-1		B9	436.9900	11.3871	30	X
3	MS-1		B10	447.1700	11.3871	30	X
4	MS-1'		B11	457.3400	11.3871	30	X
5	MS-1'		B12	467.5200	11.3871	30	X
6	MS-1'		B13	477.6900	11.3871	30	X
7	MS-1'	X	B14	487.8700	11.3784	30	X
8	MS-1'	X	B15	498.0400	11.3538	30	
9	MS-1'	X	B16	508.2200	11.3133	30	
10		X	B17	518.3900	11.2580	30	
11	MS-2	X	B18	528.5700	11.1907	30	
12	MS-2	X	B19	538.7400	11.1119	30	
13	MS-2	X	B20	548.9200	11.0245	30	
14	MS-2	X	B21	559.0900	10.9321	30	
15	MS-2	X	B22	569.2700	10.8368	30	
16	MS-2	X	B23	579.4500	10.7407	30	
17	MS-2	X	B24	589.6200	10.6482	30	
18	MS-2	X	B25	599.8000	10.5607	30	
19		X	B26	609.9700	10.4823	30	
20		X	B27	620.1500	10.4147	30	
21	MS-3	X	B28	630.3200	10.3595	30	

22	MS-3	X	B29	640.5000	10.3188	30	
23	MS-3	X	B30	650.6700	10.2942	30	
24	MS-3	X	B31	660.8500	10.2856	30	
25	MS-3	X	B32	671.0200	10.2980	30	
26	MS-3	X	B33	681.2000	10.3349	30	
27			B34	691.3700	10.3909	30	
28			B35	701.5500	10.4592	30	
29			B36	711.7200	10.5322	30	
30			B37	721.9000	10.6004	30	
31			B38	732.0700	10.6562	30	
32			B39	742.2500	10.6933	30	
33			B40	752.4300	10.7058	30	
34			B41	762.6000	10.7276	30	
35	MS-4		B42	772.7800	10.7907	30	
36	MS-4		B43	782.9500	10.8833	30	
37	MS-4		B44	793.1300	10.9938	30	
38	MS-4		B45	803.3000	11.1044	30	
39			B46	813.4800	11.1980	30	
40			B47	823.6500	11.2600	30	
41			B48	833.8300	11.2824	30	
42	MS-4'		B49	844.0000	11.2822	30	
43	MS-4'		B50	854.1800	11.2816	30	
44	MS-4'		B51	864.3500	11.2809	30	
45	MS-4'		B52	874.5300	11.2797	30	
46	MS-4'		B53	884.7000	11.2782	30	
47			B54	894.8800	11.2771	30	
48			B55	905.0500	11.2765	30	
49			B77	912.4500	11.0457	30	

50			B56	915.2300	11.2756	30	**X**
51			B78	922.5400	11.0457	30	
52			B57	925.4100	11.2754	30	**X**
53			B79	932.6400	11.0457	30	
54			B83	972.9900	11.0457	30	**X**
55			B84	983.0800	11.0457	30	
56			B85	993.1700	11.0457	30	**X**
57			B86	1003.3000	11.0457	30	
58			B87	1013.3000	11.0457	30	**X**
59			B88	1023.4000	11.0451	30	
60			B89	1033.4900	11.0423	30	**X**
61			B90	1043.5900	11.0372	30	
62			B91	1053.6900	11.0302	30	
63			B92	1063.7900	11.0218	30	
64			B93	1073.8900	11.0122	30	
65			B94	1083.9900	11.0013	30	
66			B95	1094.0900	10.9871	30	
67			B96	1104.1900	10.9732	30	**X**
68			B97	1114.1900	10.9572	30	
69			B98	1124.2800	10.9418	30	**X**
70			B99	1134.3800	10.9248	30	
71			B100	1144.4800	10.9065	30	**X**
72			B101	1154.5800	10.8884	30	
73			B102	1164.6800	10.8696	30	**X**
74			B103	1174.7700	10.8513	30	
75			B104	1184.8700	10.8335	30	**X**
76			B105	1194.9700	10.8154	30	
77	MS-5'		B106	1205.0700	10.7979	30	**X**

78	MS-5'		B107	1215.1700	10.7822	30	
79	MS-5'		B108	1225.1700	10.7663	30	**X**
80	MS-5'		B109	1235.2700	10.7520	30	
81	MS-5'		B110	1245.3600	10.7385	30	**X**
82	MS-5'		B111	1255.4600	10.7270	30	
83	MS-5'		B112	1265.5600	10.7174	30	**X**
84	MS-5'		B113	1275.6600	10.7091	30	
85	MS-5'		B114	1285.7600	10.7022	30	**X**
86	MS-5'		B115	1295.8600	10.6970	30	
87			B116	1305.9600	10.6946	30	**X**
88			B117	1316.0500	10.6937	30	
89			B118	1326.0500	10.6949	30	**X**
90			B119	1336.1500	10.6996	30	
91			B133	1477.4300	11.0074	30	**X**
92			B134	1487.5300	11.0414	30	
93			B135	1497.6300	11.0759	30	
94			B136	1507.7300	11.1108	30	
95			B137	1517.8300	11.1461	30	
96			B138	1527.9200	11.1811	30	
97			B139	1537.9200	11.2156	30	
98			B140	1548.0200	11.2496	30	
99	MS-5		B141	1558.1200	11.2826	30	
100	MS-5		B142	1568.2200	11.3146	30	
101	MS-5		B143	1578.3200	11.3460	30	
102	MS-5		B144	1588.4200	11.3753	30	
103	MS-5		B145	1598.5100	11.4037	30	
104	MS-5		B146	1608.6100	11.4302	30	
105	MS-5		B147	1618.7100	11.4538	30	

106	MS-5		B148	1628.8100	11.4760	30	
107	MS-5		B149	1638.8100	11.4958	30	
108	MS-5		B150	1648.9000	11.5133	30	
109	MS-5		B151	1659.0000	11.5286	30	
110	MS-5		B152	1669.1000	11.5404	30	
111	MS-5		B153	1679.2000	11.5505	30	
112	MS-5		B154	1689.3000	11.5580	30	
113	MS-5		B155	1699.4000	11.5621	30	
114	MS-5		B156	1709.5000	11.5634	30	
115	MS-5		B157	1719.6000	11.5617	30	
116	MS-5		B158	1729.7000	11.5563	30	
117	MS-5		B159	1739.7000	11.5477	30	
118	MS-5		B160	1749.7900	11.5346	30	
119			B161	1759.8900	11.5193	30	
120			B162	1769.9900	11.5002	30	
121			B163	1780.0900	11.4789	30	
122			B164	1790.1900	11.4548	30	
123			B183	1981.8600	10.9230	30	
124			B184	1991.9600	10.9139	30	
125			B188	2032.3500	10.9013	30	
126			B189	2042.4500	10.8951	30	
127			B190	2052.4500	10.8854	30	
128			B191	2062.5500	10.8740	30	
129			B192	2072.6500	10.8591	30	
130	MS-7		B193	2082.7500	10.8429	30	
131	MS-7		B194	2092.8400	10.8242	30	
132	MS-7		B195	2102.9400	10.8039	30	
133	MS-7		B196	2113.0400	10.7820	30	

134	MS-7		B197	2123.1400	10.7592	30	
135	MS-7		B198	2133.2400	10.7342	30	
136	MS-7		B199	2143.3400	10.7092	30	
137	MS-7		B200	2153.3400	10.6834	30	
138	MS-7		B201	2163.4300	10.6572	30	
139	MS-7		B202	2173.5300	10.6312	30	
140	MS-7		B203	2183.6300	10.6052	30	
141	MS-7		B204	2193.7300	10.5803	30	
142	MS-7		B205	2203.8300	10.5560	30	
143	MS-7		B206	2213.9300	10.5328	30	
144	MS-7		B207	2224.0300	10.5101	30	
145	MS-7		B208	2234.1200	10.4904	30	
146	MS-7		B209	2244.2200	10.4722	30	
147	MS-7		B210	2254.2200	10.4552	30	
148	MS-7		B211	2264.3200	10.4408	30	
149	MS-7		B212	2274.4200	10.4285	30	
150	MS-7		B213	2284.5200	10.4197	30	
151	MS-7		B214	2294.6100	10.4129	30	
152	MS-7		B215	2304.7100	10.4088	30	
153	MS-7		B216	2314.8100	10.4077	30	
154	MS-7		B217	2324.9100	10.4077	30	
155	MS-7		B218	2335.0100	10.4077	30	
156	MS-7		B219	2345.1100	10.4077	30	
157			B220	2355.2100	10.4077	30	

Table 23: Hyperion bands (USGS, 2011).

Colour key:

Spectral area of blue
Spectral area of green
Spectral area of red

Appendix III: Spectral bands of the CASI imagery

1. CASI imagery without atmospheric correction

Band 01	**421.8nm+/-**	**3.8nm**
Band 02	429.5nm+/-	3.8nm
Band 03	437.1nm+/-	3.8nm
Band 04	444.8nm+/-	3.8nm
Band 05	452.4nm+/-	3.8nm
Band 06	460.0nm+/-	3.8nm
Band 07	467.7nm+/-	3.8nm
Band 08	475.3nm+/-	3.8nm
Band 09	482.9nm+/-	3.8nm
Band 10	490.5nm+/-	3.8nm
Band 11	498.1nm+/-	3.8nm
Band 12	505.7nm+/-	3.8nm
Band 13	513.3nm+/-	3.8nm
Band 14	520.8nm+/-	3.8nm
Band 15	528.4nm+/-	3.8nm
Band 16	536.0nm+/-	3.8nm
Band 17	543.6nm+/-	3.8nm
Band 18	551.1nm+/-	3.8nm
Band 19	558.7nm+/-	3.8nm
Band 20	566.3nm+/-	3.8nm
Band 21	573.8nm+/-	3.8nm
Band 22	581.4nm+/-	3.8nm
Band 23	589.0nm+/-	3.8nm
Band 24	596.5nm+/-	3.8nm
Band 25	604.1nm+/-	3.8nm
Band 26	611.6nm+/-	3.8nm
Band 27	619.2nm+/-	3.8nm
Band 28	626.8nm+/-	3.8nm
Band 29	634.3nm+/-	3.8nm
Band 30	641.9nm+/-	3.8nm
Band 31	649.5nm+/-	3.8nm
Band 32	657.0nm+/-	3.8nm
Band 33	664.6nm+/-	3.8nm
Band 34	672.2nm+/-	3.8nm
Band 35	679.8nm+/-	3.8nm

Band 36	687.4nm+/-	3.8nm
Band 37	695.0nm+/-	3.8nm
Band 38	702.6nm+/-	3.8nm
Band 39	710.2nm+/-	3.8nm
Band 40	717.8nm+/-	3.8nm
Band 41	725.4nm+/-	3.8nm
Band 42	733.1nm+/-	3.8nm
Band 43	740.7nm+/-	3.8nm
Band 44	748.4nm+/-	3.8nm
Band 45	756.0nm+/-	3.8nm
Band 46	763.7nm+/-	3.8nm
Band 47	771.4nm+/-	3.8nm
Band 48	779.1nm+/-	3.8nm
Band 49	786.8nm+/-	3.9nm
Band 50	794.5nm+/-	3.9nm
Band 51	802.2nm+/-	3.9nm
Band 52	809.9nm+/-	3.9nm
Band 53	817.7nm+/-	3.9nm
Band 54	825.4nm+/-	3.9nm
Band 55	833.2nm+/-	3.9nm
Band 56	841.0nm+/-	3.9nm
Band 57	848.8nm+/-	3.9nm
Band 58	856.6nm+/-	3.9nm
Band 59	864.4nm+/-	3.9nm
Band 60	872.3nm+/-	3.9nm
Band 61	880.1nm+/-	3.9nm
Band 62	888.0nm+/-	3.9nm
Band 63	895.9nm+/-	4.0nm
Band 64	903.8nm+/-	4.0nm
Band 65	911.7nm+/-	4.0nm
Band 66	919.7nm+/-	4.0nm
Band 67	927.6nm+/-	4.0nm
Band 68	935.6nm+/-	4.0nm
Band 69	943.6nm+/-	4.0nm
Band 70	951.6nm+/-	4.0nm
Band 71	959.7nm+/-	4.0nm
Band 72	967.7nm+/-	4.0nm

Table 24: Bands and bandwidths of CASI imagery without atmospheric corrections.

2. CASI imagery with atmospheric correction (CASI-ATM)

Band 01	**421.8nm+/-**	**3.8nm**
Band 02	429.5nm+/-	3.8nm
Band 03	437.1nm+/-	3.8nm
Band 04	444.8nm+/-	3.8nm
Band 05	452.4nm+/-	3.8nm
Band 06	460.0nm+/-	3.8nm
Band 07	467.7nm+/-	3.8nm
Band 08	475.3nm+/-	3.8nm
Band 09	490.5nm+/-	3.8nm
Band 10	498.1nm+/-	3.8nm
Band 11	505.7nm+/-	3.8nm
Band 12	513.3nm+/-	3.8nm
Band 13	520.8nm+/-	3.8nm
Band 14	528.4nm+/-	3.8nm
Band 15	536.0nm+/-	3.8nm
Band 16	543.6nm+/-	3.8nm
Band 17	551.1nm+/-	3.8nm
Band 18	558.7nm+/-	3.8nm
Band 19	566.3nm+/-	3.8nm
Band 20	573.8nm+/-	3.8nm
Band 21	581.4nm+/-	3.8nm
Band 22	589.0nm+/-	3.8nm
Band 23	596.5nm+/-	3.8nm
Band 24	604.1nm+/-	3.8nm
Band 25	611.6nm+/-	3.8nm
Band 26	619.2nm+/-	3.8nm
Band 27	626.8nm+/-	3.8nm
Band 28	634.3nm+/-	3.8nm
Band 29	641.9nm+/-	3.8nm
Band 30	649.5nm+/-	3.8nm
Band 31	657.0nm+/-	3.8nm
Band 32	664.6nm+/-	3.8nm
Band 33	672.2nm+/-	3.8nm
Band 34	679.8nm+/-	3.8nm
Band 35	687.4nm+/-	3.8nm
Band 36	695.0nm+/-	3.8nm
Band 37	702.6nm+/-	3.8nm
Band 38	710.2nm+/-	3.8nm
Band 39	717.8nm+/-	3.8nm

Band 40	725.4nm+/-	3.8nm
Band 41	733.1nm+/-	3.8nm
Band 42	740.7nm+/-	3.8nm
Band 43	748.4nm+/-	3.8nm
Band 44	756.0nm+/-	3.8nm
Band 45	763.7nm+/-	3.8nm
Band 46	771.4nm+/-	3.8nm
Band 47	779.1nm+/-	3.8nm
Band 48	786.8nm+/-	3.9nm
Band 49	794.5nm+/-	3.9nm
Band 50	802.2nm+/-	3.9nm
Band 51	809.9nm+/-	3.9nm
Band 52	817.7nm+/-	3.9nm
Band 53	825.4nm+/-	3.9nm
Band 54	833.2nm+/-	3.9nm
Band 55	841.0nm+/-	3.9nm
Band 56	848.8nm+/-	3.9nm
Band 57	856.6nm+/-	3.9nm
Band 58	864.4nm+/-	3.9nm
Band 59	872.3nm+/-	3.9nm
Band 60	880.1nm+/-	3.9nm
Band 61	888.0nm+/-	3.9nm
Band 62	895.9nm+/-	4.0nm
Band 63	903.8nm+/-	4.0nm
Band 64	911.7nm+/-	4.0nm
Band 65	919.7nm+/-	4.0nm
Band 66	927.6nm+/-	4.0nm
Band 67	935.6nm+/-	4.0nm
Band 68	943.6nm+/-	4.0nm
Band 69	951.6nm+/-	4.0nm
Band 70	959.7nm+/-	4.0nm
Band 71	967.7nm+/-	4.0nm
Band 72	shadow mask	

Table 25: CASI bands and bandwidths with atmospheric corrections.

Appendix IV: Tree species' spectral signature correlation tables

1. CASI 2m Spatial Resolution Imagery

Band	Pinus Halepensis	Maquis	Pinus Maritime	Pinus Nigra	Oak	Pinus Brutia	Beech
452.4			x	x		x	x
460.0	x	x	x	x	x	x	x
467.7	x	x	x	x	x	x	x
490.5	x		x		x		x
498.1	x		x		x	x	x
551.1		x	x	x		x	x
672.2	x		x	x		x	x
702.6	x						x
740.7	x				x	x	x
748.4	x		x		x	x	x
756.0	x		x	x	x	x	x
763.7	x		x		x	x	x
856.6				x		x	
864.4	x	x	x	x	x	x	x

Table 26: Spectral bands where correlation between spectral signatures of tree species is significant (below 98% for three or more correlations between classes). X denotes the classes for which each bandwidth is considered of importance relative to the information conveyed, based on this method.

2. Hyperion Imagery

Band	Pinus Halepensis	Maquis	Pinus Maritime	Pinus Nigra	Oak	Pinus Brutia	Beech
508.22			x	x	x		x
518.39	x	x	x	x	x	x	x
528.57	x	x	x	x	x	x	x
538.74	x	x	x	x	x	x	x
548.92	x	x	x	x	x	x	x
559.09				x	x		
671.02	x	x	x	x	x	x	x
752.43	x	x		x	x		
762.60	x	x		x	x	x	x
803.30		x				x	
823.65			x				x
833.83			x				x
1003.30		x	x				x
1013.30	x	x	x	x	x	x	x
1023.40	x	x	x	x	x	x	x
1033.49	x	x	x	x	x	x	x
1043.59	x	x	x	x	x	x	x
1053.69	x	x	x		x	x	x
1225.17	x		x	x	x	x	x
1235.27	x		x		x		
1558.12	x				x		x
1568.22	x	x	x	x	x	x	x
1578.32	x	x	x	x	x	x	x
1588.42	x		x		x		x
1608.61			x		x		x

Table 27: Spectral bands where correlation between spectral signatures of tree species is significant (below 98% for three or more correlations between classes). X denotes the classes for which each bandwidth is considered of importance relative to the information conveyed, based on this method.

Appendix V: Producer, User, KIA per Class and Overall Accuracy

1. Group A Classification Accuracies

All bands									
	CASI 2m			**Casi 5m**			**Casi 2m ATM**		
Classes	Prod.	User	KIA	Prod.	User	KIA	Prod.	User	KIA
Maquis	0.47	0.56	0.38	0.44	0.46	0.33	0.39	0.44	0.28
Maquis/ P.Brutia	0	-	0	0	-	0	0	-	0
Maquis/ Oak	0.41	0.24	0.36	0.26	0.14	0.19	0.32	0.17	0.25
Castanea	0	-	0	0	-	0	0	-	0
Fir	-	-	-	-	-	-	-	-	-
Beech	0.23	0.34	0.21	0.13	0.34	0.11	0.20	0.30	0.18
Beech/ P.Nigra	0.05	0.18	0.05	0.03	0.10	0.03	0.05	0.25	0.05
Beech/ Oak	0.16	0.22	0.15	0.01	0.05	0	0.11	0.22	0.10
P.Brutia	0.68	0.57	0.62	0.59	0.48	0.52	0.57	0.51	0.50
P. Brutia/ Maquis	0.22	0.28	0.20	0.30	0.18	0.26	0.29	0.20	0.26
P. Brutia/ Oak	0.14	0.20	0.11	0.06	0.12	0.04	0.10	0.18	0.07
PinusSpp	0.59	0.27	0.59	0.12	0.07	0.12	0.40	0.08	0.40
P. Halepensis	0	-	0	0	-	0	0	-	0
P. Maritime	0.01	0.43	0.01	0	-	0	0.02	0.08	0.02
P. Maritime/ Maquis	0.28	0.24	0.27	0.07	0.06	0.06	0.15	0.15	0.15
P.Nigra	0.29	0.38	0.28	0.17	0.14	0.16	0.17	0.12	0.16
P.Nigra/ Beech	0.05	0.12	0.05	0.03	0.04	0.03	0.02	0.03	0.01
P.Nigra/ Beech/Oak	0.28	0.08	0.28	0.14	0.02	0.13	0.26	0.08	0.26

P.Nigra/ Oak	0.18	0.22	0.14	0.09	0.23	0.07	0.09	0.20	0.07
P. Nigra/ Oak/Beech	0	-	0	0	0	0	0	0	0
P.Radiata	0	-	0	0	-	0	0	-	0
Oak	0.68	0.59	0.53	0.66	0.55	0.48	0.60	0.52	0.39
Oak/ Maquis	0.16	0.27	0.13	0.09	0.20	0.06	0.13	0.21	0.09
Oak/Beech	0.15	0.33	0.14	0.14	0.27	0.13	0.14	0.18	0.12
Oak/ P.Brutia	0.31	0.10	0.29	0.02	0.03	0.01	0.17	0.15	0.17
Oak/ P.Nigra	0.31	0.22	0.26	0.20	0.14	0.14	0.27	0.19	0.22
Oak/P. Nigra/Beech	0	-	0	0	-	0	0	-	0
BareLand	-	-	-	-	-	-	-	-	-
Agricultural Area	-	-	-	-	-	-	-	-	-
Overall Accuracy	0.45			0.39			0.38		
KIA	0.35			0.27			0.26		

Table 28: Accuracy per class. User refers to errors caused by omission of pixels where the class of interest is present in the TTA mask based on ground sampling, while producer refers to errors caused by the inclusion of pixels to a specific class, classified as a different category in the TTA mask.

All bands									
	Landsat			**GeoEye**			**Hyperion**		
Classes	Prod.	User	KIA	Prod.	User	KIA	Prod.	User	KIA
Maquis	0.59	0.69	0.52	0.49	0.39	0.35	0.36	0.46	0.26
Maquis/P.Brutia	0	-	0	0	-	0	0	-	0
Maquis/Oak	0.42	0.33	0.38	0.41	0.22	0.35	0.38	0.15	0.31
Castanea	0	-	0	0	-	0	0	-	0
Fir	0	-	0	-	0	0	0	0	0
Beech	0.24	0.34	0.21	0.29	0.40	0.27	0.20	0.34	0.18
Beech/P.Nigra	0.13	0.09	0.12	0.07	0.23	0.07	0.03	0.48	0.03
Beech/Oak	0.21	0.19	0.19	0.21	0.22	0.19	0.14	0.21	0.12
P.Brutia	0.72	0.58	0.68	0.63	0.57	0.58	0.55	0.49	0.48
P.Brutia/Maquis	0.29	0.27	0.27	0.24	0.22	0.22	0.34	0.33	0.32
P.Brutia/Oak	0.28	0.28	0.25	0.23	0.20	0.19	0.19	0.20	0.16
PinusSpp	0.16	0.11	0.15	0.44	0.32	0.44	0.32	0.24	0.32
P.Halepensis	0	-	0	0	-	0	0	-	0
P.Maritime	0.04	0.14	0.04	0.09	0.15	0.08	0.07	0.08	0.06
P.Maritime/Maquis	0.24	0.26	0.24	0.29	0.19	0.28	0.36	0.22	0.35
P.Nigra	0.34	0.23	0.33	0.29	0.26	0.28	0.24	0.29	0.23
P.Nigra/Beech	0.15	0.23	0.14	0.13	0.19	0.12	0.19	0.19	0.18
P.Nigra/Beech/Oak	0.16	0.22	0.16	0.35	0.13	0.35	0.14	0.14	0.14
P.Nigra/Oak	0.30	0.35	0.25	0.15	0.32	0.12	0.10	0.22	0.07
P.Nigra/Oak/Beech	0	-	0	0	-	0	0	-	0
P.Radiata	0	-	0	0	-	0	0	-	0
Oak	0.67	0.62	0.51	0.47	0.59	0.31	0.64	0.54	0.46
Oak/Maquis	0.18	0.26	0.14	0.20	0.24	0.15	0.16	0.20	0.11
Oak/Beech	0.18	0.20	0.16	0.13	0.22	0.11	0.12	0.25	0.11
Oak/P.Brutia	0.18	0.15	0.17	0.22	0.13	0.21	0.16	0.13	0.15
Oak/P.Nigra	0.29	0.23	0.25	0.33	0.19	0.28	0.30	0.24	0.26
Oak/P.Nigra/Beech	0	-	0	0	-	0	0	-	0
BareLand	-	-	-	-	-	-	-	-	-
AgriculturalArea	-	-	-	-	-	-	-	-	-
Overall Accuracy	0.49			0.39			0.39		
KIA	0.39			0.30			0.28		

Table 29: Accuracy per class for satellite data projects including all bands. User refers to errors caused by omission of pixels where the class of interest is present in the TTA mask based on ground sampling, while producer refers to errors caused by the inclusion of pixels to a specific class, classified as a different category in the TTA mask.

PCA						
	Casi 5m			**Casi 2m ATM**		
Classes	Prod.	User	KIA	Prod.	User	KIA
Maquis	0.40	0.46	0.30	0.39	0.44	0.28
Maquis/P.Brutia	0	-	0	0	-	0
Maquis/Oak	0.43	0.24	0.38	0.32	0.17	0.25
Castanea	0	-	0	0	-	0
Fir	-	-	-	-	-	0
Beech	0.25	0.32	0.23	0.20	0.30	0.18
Beech/P.Nigra	0.08	0.22	0.08	0.05	0.25	0.05
Beech/Oak	0.18	0.23	0.17	0.11	0.22	0.10
P.Brutia	0.50	0.52	0.44	0.57	0.51	0.50
P.Brutia/Maquis	0.34	0.34	0.32	0.29	0.20	0.26
P.Brutia/Oak	0.29	0.28	0.25	0.10	0.18	0.07
PinusSpp	0.48	0.22	0.48	0.40	0.08	0.40
P.Halepensis	0	-	0	0	-	0
P.Maritime	0.05	0.13	0.05	0.02	0.08	0.02
P.Maritime/Maquis	0.25	0.20	0.24	0.15	0.15	0.15
P.Nigra	0.31	0.20	0.29	0.17	0.12	0.16
P.Nigra/Beech	0.08	0.18	0.08	0.02	0.03	0.01
P.Nigra/Beech/Oak	0.57	0.13	0.57	0.26	0.08	0.26
P.Nigra/Oak	0.14	0.25	0.12	0.09	0.20	0.07
P.Nigra/Oak/Beech	0	-	0	0	-	0
P.Radiata	0	-	0	0	-	0
Oak	0.62	0.55	0.44	0.60	0.52	0.39
Oak/Maquis	0.16	0.29	0.12	0.13	0.21	0.09
Oak/Beech	0.21	0.22	0.19	0.14	0.18	0.12
Oak/P.Brutia	0.37	0.19	0.36	0.17	0.15	0.17
Oak/P.Nigra	0.34	0.25	0.30	0.27	0.19	0.22
Oak/P.Nigra/Beech	0	-	0	0	-	0
BareLand	-	-	-	-	-	-
AgriculturalArea	-	-	-	-	-	-
Overall Accuracy	0.41			0.38		
KIA	0.31			0.26		

Table 30: Accuracy per class for PCA projects. User refers to errors caused by omission of pixels where the class of interest is present in the TTA mask based on ground sampling, while producer refers to errors caused by the inclusion of pixels to a specific class, classified as a different category in the TTA mask.

PCA						
	Casi 5m ATM			**Hyperion**		
Classes	Prod.	User	KIA	Prod.	User	KIA
Maquis	0.39	0.47	0.28	0.70	0.59	0.62
Maquis/P.Brutia	0	-	0	0	-	0
Maquis/Oak	0.43	0.24	0.37	0.28	0.14	0.21
Castanea	0	-	0	0	-	0
Fir	0	0	0	0	0	0
Beech	0.25	0.32	0.23	0.12	0.15	0.09
Beech/P.Nigra	0.08	0.26	0.08	0.09	0.09	0.08
Beech/Oak	0.19	0.23	0.17	0	0	0
P.Brutia	0.51	0.50	0.44	0.23	0.39	0.17
P.Brutia/Maquis	0.34	0.35	0.32	0.31	0.24	0.29
P.Brutia/Oak	0.27	0.26	0.24	0.12	0.16	0.09
PinusSpp	0.46	0.25	0.46	0	-	0
P.Halepensis	0	-	0	0	-	0
P.Maritime	0.05	0.13	0.05	0	-	0
P.Maritime/Maquis	0.25	0.19	0.24	0.26	0.28	0.26
P.Nigra	0.29	0.19	0.28	0.19	0.18	0.18
P.Nigra/Beech	0.09	0.15	0.09	0.07	0.11	0.06
P.Nigra/Beech/Oak	0.62	0.12	0.62	0	-	0
P.Nigra/Oak	0.14	0.28	0.12	0.01	0.03	-0.01
P.Nigra/Oak/Beech	0	-	0	0	-	0
P.Radiata	0	-	0	0	-	0
Oak	0.62	0.54	0.44	0.68	0.50	0.49
Oak/Maquis	0.15	0.27	0.12	0.12	0.18	0.08
Oak/Beech	0.21	0.22	0.19	0.04	0.05	0.02
Oak/P.Brutia	0.39	0.18	0.38	0	-	0
Oak/P.Nigra	0.34	0.24	0.29	0.17	0.11	0.12
Oak/P.Nigra/Beech	0	-	0	0	-	0
BareLand	-	-	-	-	-	-
AgriculturalArea	-	-	-	-	-	-
Overall Accuracy	0.41			0.39		
KIA	0.30			0.27		

Table 31: Accuracy per class for PCA projects. User refers to errors caused by omission of pixels where the class of interest is present in the TTA mask based on ground sampling, while producer refers to errors caused by the inclusion of pixels to a specific class, classified as a different category in the TTA mask.

MNF						
	Casi 2m			**Hyperion**		
Classes	Prod.	User	KIA	Prod.	User	KIA
Maquis	0.43	0.51	0.33	0.59	0.67	0.52
Maquis/P.Brutia	0	-	0	0	-	0
Maquis/Oak	0.42	0.20	0.36	0.37	0.14	0.29
Castanea	0	-	0	0	-	0
Fir	-	-	-	-	-	-
Beech	0.26	0.51	0.25	0.10	0.39	0.09
Beech/P.Nigra	0.05	0.21	0.05	0	-	0
Beech/Oak	0.25	0.19	0.23	0.40	0.23	0.38
P.Brutia	0.65	0.56	0.60	0.76	0.51	0.71
P.Brutia/Maquis	0.34	0.41	0.33	0.40	0.24	0.37
P.Brutia/Oak	0.31	0.37	0.28	0.22	0.19	0.18
PinusSpp	0.22	0.15	0.22	0	-	0
P.Halepensis	0	-	0	0	-	0
P.Maritime	0.02	0.04	0.02	0	-	0
P.Maritime/Maquis	0.22	0.14	0.21	0	-	0
P.Nigra	0.13	0.14	0.12	0	-	0
P.Nigra/Beech	0.06	0.07	0.05	0	-	0
P.Nigra/Beech/Oak	0	-	0	0	-	0
P.Nigra/Oak	0.12	0.20	0.09	0	-	0
P.Nigra/Oak/Beech	0	-	0	0	-	0
P.Radiata	0	-	0	0	-	0
Oak	0.67	0.62	0.52	0.66	0.60	0.51
Oak/Maquis	0.18	0.27	0.14	0.16	0.17	0.10
Oak/Beech	0.13	0.21	0.12	0	-	0
Oak/P.Brutia	0.28	0.16	0.27	0.34	0.09	0.32
Oak/P.Nigra	0.24	0.21	0.20	0.28	0.43	0.26
Oak/P.Nigra/Beech	0	-	0	0	-	0
BareLand	-	-	-	-	-	-
AgriculturalArea	-	-	-	-	-	-
Overall Accuracy	0.44			0.44		
KIA	0.34			0.35		

Table 32: Accuracy per class for MNF projects. User refers to errors caused by omission of pixels where the class of interest is present in the TTA mask based on ground sampling, while producer refers to errors caused by the inclusion of pixels to a specific class, classified as a different category in the TTA mask.

Band selection based on spectral signatures						
	Casi 2m			**Hyperion**		
Classes	Prod.	User	KIA	Prod.	User	KIA
Maquis	0.42	0.51	0.32	0.54	0.47	0.43
Maquis/P.Brutia	0	-	0	0	-	0
Maquis/Oak	0.43	0.26	0.38	0.36	0.23	0.32
Castanea	0	-	0	0	-	0
Fir	-	-	-	0	-	0
Beech	0.28	0.38	0.26	0.22	0.26	0.19
Beech/P.Nigra	0.07	0.28	0.07	0.11	0.19	0.11
Beech/Oak	0.20	0.27	0.19	0.19	0.21	0.17
P.Brutia	0.60	0.56	0.54	0.50	0.47	0.44
P.Brutia/Maquis	0.33	0.38	0.31	0.26	0.27	0.24
P.Brutia/Oak	0.29	0.31	0.26	0.19	0.18	0.16
PinusSpp	0.60	0.30	0.60	0.15	0.10	0.14
P.Halepensis	0	-	0	0	-	0
P.Maritime	0.05	0.15	0.05	0.07	0.17	0.07
P.Maritime/Maquis	0.32	0.18	0.31	0.39	0.25	0.39
P.Nigra	0.31	0.22	0.30	0.21	0.19	0.20
P.Nigra/Beech	0.08	0.16	0.08	0.11	0.21	0.11
P.Nigra/Beech/Oak	0.67	0.20	0.67	0.11	0.12	0.11
P.Nigra/Oak	0.19	0.31	0.16	0.11	0.23	0.08
P.Nigra/Oak/Beech	0	-	0	0	-	0
P.Radiata	0	-	0	0	-	0
Oak	0.68	0.60	0.53	0.55	0.54	0.34
Oak/Maquis	0.19	0.31	0.16	0.18	0.21	0.14
Oak/Beech	0.26	0.28	0.24	0.14	0.26	0.13
Oak/P.Brutia	0.30	0.14	0.29	0.17	0.13	0.16
Oak/P.Nigra	0.35	0.24	0.30	0.27	0.20	0.23
Oak/P.Nigra/Beech	0	-	0	0	-	0
BareLand	-	-	-	-	-	-
AgriculturalArea	-	-	-	-	-	-
Overall Accuracy	0.45			0.39		
KIA	0.35			0.28		

Table 33: Accuracy per class for the band selection method based on spectral signatures of forest tree species. User refers to errors caused by omission of pixels where the class of interest is present in the TTA mask based on ground sampling, while producer refers to errors caused by the inclusion of pixels to a specific class, classified as a different category in the TTA mask.

2. Group B Classification Accuracies

All bands									
	Casi 2m			**Casi 5m**			**Casi 2m ATM**		
Classes	Prod.	User	KIA	Prod.	User	KIA	Prod.	User	KIA
Maquis	0.61	0.77	0.50	0.60	0.65	0.46	0.58	0.64	0.44
Castanea	0	-	0	0	-	0	0	-	0
Beech	0.29	0.37	0.26	0.19	0.53	0.17	0.24	0.40	0.21
P.Brutia	0.77	0.71	0.71	0.65	0.65	0.58	0.63	0.64	0.55
PinusSpp	0.59	0.23	0.59	0.12	0.09	0.12	0.40	0.11	0.40
P.Maritime	0.01	0.58	0.01	0	-	0	0.02	0.08	0.02
P.Nigra	0.31	0.41	0.30	0.17	0.11	0.15	0.17	0.14	0.15
P.Pinea	0	-	0	0	-	0	0	-	0
Oak	0.87	0.76	0.72	0.83	0.75	0.65	0.79	0.71	0.57
Overall Accuracy	0.73			0.68			0.65		
KIA	0.59			0.51			0.48		

Table 34: Accuracy per class for Casi projects containing all bands. User refers to errors caused by omission of pixels where the class of interest is present in the TTA mask based on ground sampling, while producer refers to errors caused by the inclusion of pixels to a specific class, classified as a different category in the TTA mask.

All bands									
	Landsat			**GeoEye**			**Hyperion**		
Classes	Prod.	User	KIA	Prod.	User	KIA	Prod.	User	KIA
Maquis	0.70	0.82	0.62	0.69	0.53	0.51	0.65	0.60	0.52
Castanea	0	-	0	0	-	0	0	-	0
Beech	0.38	0.47	0.34	0.51	0.63	0.48	0.23	0.41	0.20
P.Brutia	0.82	0.73	0.79	0.79	0.73	0.74	0.67	0.64	0.61
PinusSpp	0.16	0.15	0.16	0.44	0.27	0.44	0.13	0.15	0.13
P.Maritime	0.07	0.28	0.06	0.09	0.16	0.08	0.07	0.14	0.07
P.Nigra	0.44	0.49	0.43	0.33	0.41	0.31	0.26	0.43	0.25
P.Pinea	0	-	0	0	-	0	0	-	0
Oak	0.87	0.81	0.73	0.65	0.79	0.44	0.75	0.73	0.50
Overall Accuracy	0.77			0.66			0.66		
KIA	0.65			0.52			0.48		

Table 35: Accuracy per class for satellite data projects containing all bands. User refers to errors caused by omission of pixels where the class of interest is present in the TTA mask based on ground sampling, while producer refers to errors caused by the inclusion of pixels to a specific class, classified as a different category in the TTA mask.

PCA						
	Casi 5m			**Casi 2m ATM**		
Classes	Prod.	User	KIA	Prod.	User	KIA
Maquis	0.57	0.65	0.43	0.59	0.65	0.45
Castanea	0	-	0	0	-	0
Beech	0.29	0.36	0.26	0.29	0.35	0.26
P.Brutia	0.58	0.64	0.50	0.59	0.65	0.52
PinusSpp	0.48	0.27	0.48	0.58	0.28	0.58
P.Maritime	0.09	0.18	0.08	0.05	0.12	0.04
P.Nigra	0.34	0.25	0.33	0.38	0.27	0.36
P.Pinea	0	-	0	0	-	0
Oak	0.80	0.71	0.58	0.80	0.73	0.60
Overall Accuracy	0.65			0.66		
KIA	0.48			0.49		

Table 36: Accuracy per class for the PCA projects. User refers to errors caused by omission of pixels where the class of interest is present in the TTA mask based on ground sampling, while producer refers to errors caused by the inclusion of pixels to a specific class, classified as a different category in the TTA mask.

PCA						
	Casi 5m ATM			**Hyperion**		
Classes	Prod.	User	KIA	Prod.	User	KIA
Maquis	0.56	0.66	0.41	0.75	0.67	0.65
Castanea	0	-	0	0	-	0
Beech	0.29	0.36	0.26	0.22	0.43	0.19
P.Brutia	0.58	0.61	0.50	0.44	0.49	0.35
PinusSpp	0.46	0.29	0.46	0	-	0
P.Maritime	0.05	0.12	0.05	0	-	0
P.Nigra	0.34	0.25	0.32	0.22	0.65	0.22
P.Pinea	0	-	0	0	-	0
Oak	0.80	0.70	0.58	0.73	0.67	0.43
Overall Accuracy	0.65			0.64		
KIA	0.47			0.44		

Table 37: Accuracy per class for the PCA projects. User refers to errors caused by omission of pixels where the class of interest is present in the TTA mask based on ground sampling, while producer refers to errors caused by the inclusion of pixels to a specific class, classified as a different category in the TTA mask.

MNF						
	Casi 2m			**Hyperion**		
Classes	Prod.	User	KIA	Prod.	User	KIA
Maquis	0.75	0.74	0.65	0.76	0.63	0.66
Castanea	0	-	0	0	-	0
Beech	0.45	0.62	0.43	0.08	0.37	0.06
P.Brutia	0.77	0.75	0.72	0.86	0.60	0.82
PinusSpp	0.22	0.28	0.22	0	-	0
P.Maritime	0.02	0.03	0.02	0	-	0
P.Nigra	0.16	0.14	0.15	0	-	0
P.Pinea	0	-	0	0	-	0
Oak	0.82	0.81	0.67	0.72	0.80	0.50
Overall Accuracy	0.75			0.69		
KIA	0.63			0.53		

Table 38: Accuracy per class for the MNF projects. User refers to errors caused by omission of pixels where the class of interest is present in the TTA mask based on ground sampling, while producer refers to errors caused by the inclusion of pixels to a specific class, classified as a different category in the TTA mask.

Band selection based on spectral signatures						
	Casi 2m			**Hyperion**		
Classes	Prod.	User	KIA	Prod.	User	KIA
Maquis	0.60	0.71	0.47	0.62	0.60	0.49
Castanea	0	-	0	0	-	0
Beech	0.38	0.47	0.35	0.25	0.33	0.21
P.Brutia	0.68	0.69	0.61	0.64	0.64	0.57
PinusSpp	0.64	0.35	0.64	0.15	0.13	0.14
P.Maritime	0.05	0.15	0.05	0.07	0.19	0.07
P.Nigra	0.35	0.24	0.33	0.25	0.28	0.23
P.Pinea	0	-	0	0	0	0
Oak	0.83	0.75	0.66	0.73	0.71	0.46
Overall Accuracy	0.70			0.64		
KIA	0.55			0.45		

Table 39: Accuracy per class for the band selection method based on spectral signatures of forest tree species. User refers to errors caused by omission of pixels where the class of interest is present in the TTA mask based on ground sampling, while producer refers to errors caused by the inclusion of pixels to a specific class, classified as a different category in the TTA mask.

Appendix VI: List of Tree Species Present in Taxiarchis University Forest

a) Main forest tree species of economic value:

1. *Quercus frainetto*
2. *Quercus petraea spp. medwediewii (Quercus dalechampii)*
3. *Quercus pubescens*
4. *Fagus moesiacae*

b) Secondary forest tree species of limited economic value:

1. *Acer campestre*
2. *Acer platanoides*
3. *Arbutus andrachnae*
4. *Arbutus unedo*
5. *Carpinus orientalis*
6. *Castanea sativa, Castanea vesca*
7. *Cornus mas*
8. *Corylus avellana*
9. *Erica arborea*
10. *Erica verticillata*
11. *Fraxinus ornus*
12. *Ilex aquifolium*
13. *Juglans regia*
14. *Juniperus communis*
15. *Juniperus oxycedrus*
16. *Laurus nobilis*
17. *Ostrya carpinifolia*

18. *Phillyrea media*

19. *Pirus amygdaliformis*

20. *Platanus orientalis*

21. *Populus tremula*

22. *Prunus avium*

23. *Prunus spinosa*

24. *Quercus ilex*

25. *Pistacia terebinthus*

26. *Quercus coccifera*

27. *Sorbus torminalis*

28. *Sorbus domestica*

29. *Spartium junceum*

30. *Tilia tomentosa*

31. *Taxus baccata*

32. *Ulmus Montana*

Introduced species, which were planted after major forest fires, are the following:

a) Main forest tree species occupying large areas:

1. *Pinus nigra*

2. *Pinus maritima*

3. *Pinus brutia*

4. *Pinus halepensis*

b) Secondary tree species, occupying limited areas:

5. *Abies borisii regis*

6. *Cedrus atlantica*

7. *Cupressus sempervirens v. orizontalis*

8. *Pinus pinea*

9. *Pinus radiata*

10. *Pseudotsuga menziesii*

11. *Prunus avium*

12. *Robinea pseudacacia*

13. *Quercus borealis*

(Aristotle University of Thessaloniki, 2013)

Appendix VII: Tree Species, Common Names and Greek Names

Name used in this study	Species name	Common name	Common Greek name
Beech	*Fagus moesiacae*	Balkan beech	Οξιά η μοϊσιακή
Castanea	*Castanea sativa*	Sweet chestnut	Καστανιά
Fir	*Abies borisii regis*	King Boris Fir, Bulgarian Fir	Ελάτη
Maquis	*Acer platanoides*	Norway maple	Σφένδαμος πλατανοειδής
PinusBrutia	*Pinus brutia*	Turkish pine, Calabrian pine	Τραχεία Πεύκη
PinusHalepensis	Pinus halepensis	Aleppo pine, Jerusalem pine	Χαλέπιος Πεύκη
PinusMaritime	*Pinus pinaster*	Maritime pine	Παραθαλάσσια Πεύκη
PinusNigra	*Pinus nigra*	Austrian pine	Μαύρη Πεύκη
PinusPinea	*Pinus pinea*	Stone pine	Κουκουναριά
PinusRadiata	*Pinus radiata*	Monteray pine	Ραντιάτα
PinusSylvestris	*Pinus sylvestris*	Scots pine	Δασική Πεύκη
Pseudotsuga	*Pseudotsuga menziesii*	Douglas fir	Ψευδοτσούγκα
Oak	*Querqus cerris* (*Querqus coccifera* L.)	Turkey oak	Πουρνάρι - Πρίνος

Table 40: Scientific and common names of tree species common in Taxiarchis University Forest.